

# High-redshift physics from the acoustic scale

Zachary J. Weiner<sup>1,\*</sup>

<sup>1</sup>*Perimeter Institute for Theoretical Physics, Waterloo, Ontario N2L 2Y5, Canada*

(Dated: March 20, 2026)

We present a simplified and general description of the high-redshift information in acoustic scale measurements from the cosmic microwave background and large-scale structure. The transverse distance interval between photon–baryon decoupling and a late epoch in the matter era provides an analytically tractable summary statistic thereof and a general diagnostic of the current tension between the Dark Energy Spectroscopic Instrument and the CMB. We show that this “matter-era distance excess” is unlikely to be explained by modified dynamics at low redshift. We then analytically derive the matter-era distance interval’s sensitivity to new physics at high redshift, including nonstandard recombination, nonminimal dark matter dynamics, and spatial curvature; in particular, we explain how this observable represents a direct geometric measurement of (and underlies the current incompatibility with) neutrino masses. Finally, we demonstrate that phenomenological models of dynamical dark energy mediate the matter-era distance excess in a manner reliant on their unphysical, extrapolated behavior at high redshift. Invoking alternative explanations of the excess removes the CMB’s contribution to the evidence for these models; the residual preference of around  $1.7\sigma$  mostly derives from DESI’s two lowest-redshift measurements of the Alcock–Paczynski distortion, without which it drops to  $0.5\sigma$ .

## CONTENTS

I. Introduction	2
II. The matter-era distance interval	3
A. Theoretical description	3
B. Measurement from the acoustic scale	6
C. The BAO–CMB tension as a matter-era distance excess	9
III. High-redshift solutions	14
A. Predecoupling physics	14
B. Postdecoupling physics	21
C. Implications for neutrino masses	26
D. High-redshift alternatives to dynamical dark energy	28
IV. Summary and conclusions	32
A. The matter-era distance interval	32
B. Acoustic scale tensions	33
C. Implications for dark energy	35
D. Outlook	36
Acknowledgments	36
A. Computational details	37
1. Analytic results	37
2. Numerical implementation	41
References	42

---

\* [zweiner@perimeterinstitute.ca](mailto:zweiner@perimeterinstitute.ca)

## I. INTRODUCTION

Cosmological distances derived from the acoustic scale are the leading source of contemporary information on the expansion history from high to low redshift. The angular extent of the sound horizon on the sky as inferred from the photon distribution represents the second-best measured number in cosmology [1–3] (next to the cosmic microwave background temperature [4, 5]), while analogous measurements in the distribution of galaxies and other tracers of large-scale structure have achieved subpercent precision [6]. Both are reasonably independent of the underlying cosmology and are modeled from first principles. Taking seriously any microphysical implications of these measurements demands a rigorous understanding of not just their potential systematics but also all cosmological physics relevant to their predictions—including possible alternative explanations of the data—and what complementary observational information such inference relies on.

In this work, we present a comprehensive and analytic description of the high-redshift information in the acoustic scale, i.e., distances from baryon acoustic oscillations (BAO) and the cosmic microwave background (CMB). While we primarily focus on physics outside of the redshift coverage of BAO measurements (which is presently  $z \lesssim 2 - 3$ ), our treatment does not ignore possible dynamics beyond the  $\Lambda$  cold dark matter ( $\Lambda$ CDM) model in this redshift range. Rather, we devise an effective summary of the information in acoustic scale data on intermediate- and high-redshift physics in the form of a single measurement that is nearly independent of low-redshift dynamics and whose predictions can be understood analytically. This description substantially sharpens the typical, vague appeal to degeneracy breaking in explaining how BAO data contribute to the inference of cosmological parameters (both in their reduced uncertainties and potentially shifted central values), which often can be incomplete or simply incorrect.

Our approach builds on insight from Ref. [7] on how the acoustic scale contributes to measurements of neutrino masses in an otherwise  $\Lambda$ CDM cosmology, motivated by the incompatibility of the Dark Energy Spectroscopic Instrument’s BAO data (combined with CMB data) with nonzero neutrino masses [6, 8]. We extend this analysis beyond  $\Lambda$ CDM and neutrino masses, explaining how the neutrino mass tension serves as a proxy for the general tension between DESI and the CMB. We quantify the relevant information as the distance photons travel during matter domination (relative to the sound horizon), which reduces to a direct measurement of the matter density in the simplest cases. This observable was in fact proposed long ago as a tool to “search for dynamical shenanigans” at high redshift in Ref. [9], and its value in constraining curvature was recognized in Ref. [10]; in this work, we demonstrate its paramount role in constraining the cosmological model in general. In Sec. II, we define the matter-era distance interval (MEDI), derive its full parameter dependence in  $\Lambda$ CDM, and obtain its measurement from the acoustic scale. Section II C 1 explains how the MEDI represents the key contribution of the CMB’s geometric information to the constraining power of acoustic scale data. We then show in Sec. II C that the tension between the acoustic scale and the CMB is most generally summarized by the MEDI as a matter-era distance excess.

In Sec. III, we demonstrate the matter-era distance interval’s efficacy in summarizing the sensitivity of CMB and BAO data to various modifications to the cosmological model at intermediate and high redshift, including not just massive neutrinos [11] (and hyperlight scalar fields, which are phenomenologically similar [12–16]) but also dark matter that decays [17–23] or whose mass evolves (as realized in scalar-mediated dark force models [24–27]). Beyond modifications to the postdecoupling expansion history, the MEDI summarizes most of the information on spatial curvature and any other scenario featuring a geometric degeneracy in the CMB—namely, early recombination via a time-varying electron mass [7, 16, 28] and the (closely related [16]) hypothesis that the present-day CMB temperature is mismeasured [29]. We also explain why high-density recombination models (like dark radiation [30–32] or early dark energy [33–37]) have a parametrically less relevant effect on acoustic scale predictions and therefore are not candidates to mediate the BAO–CMB tension.

In addition, we identify the physical mechanism by which a larger-than-measured optical depth to reionization [7, 38, 39] alleviates the matter-era distance tension. We summarize the status of these various proposals by presenting their impact on the neutrino mass tension in Sec. III C.

Though designed to be maximally independent of dark energy, the matter-era distance interval is presently affected by its density at the subpercent level. In Sec. III D, we show that the CMB’s contribution to putative preferences for dynamical dark energy [6] derives fully from mediating the matter-era distance excess. Moreover, our analytic description demonstrates that its resolution relies specifically on extrapolating linearized dark-energy equations of state to high redshift, where the behavior is nominally the most unphysical (i.e., as interpreted for fluidlike dark energy alone). We show that any alternative resolution to the matter-era distance tension removes the evidence for dark energy dynamics added by the CMB; these high-redshift alternatives also have greater potential to resolve the geometric side of the neutrino mass tension. Finally, we show that the residual, “direct” evidence for dark energy dynamics from DESI derives mostly from the Alcock–Paczynski distortion measured in its two lowest-redshift bins. We summarize our analysis in Sec. IV and conclude by discussing the outlook for resolving the matter-era distance and neutrino mass tensions and for disentangling genuine evidence of dark energy dynamics from high-redshift alternatives.

## II. THE MATTER-ERA DISTANCE INTERVAL

Were late-time observations consistent with an Einstein–de Sitter Universe, i.e., zero dark energy and curvature, the CMB, even treated as unlensed, would uniquely measure the matter abundance at early *and* late times—that in CDM and baryons at recombination (via the shape of the anisotropy spectra) and in all nonrelativistic matter present at late times (via the distance to last scattering). Disagreement between these measurements either would suggest the baryon and CDM abundances were miscalibrated or would simply measure the change in matter abundance after recombination—in particular, an increase from massive neutrinos, but also changes due to a range of nonminimal dark matter phenomena. Our premise is to combine measurements to realize this idealized scenario as robustly as possible.

We start in Sec. II A by precisely defining the observable—heuristically, the distance photons travel in the matter era—and explaining its dependence on the energy content of the standard cosmological model; we comment on what generalizations thereof this matter-era distance interval (MEDI) is sensitive to, deferring dedicated analyses to Sec. III. We then derive measurements of the MEDI from acoustic scale observations, discussing their robustness to the low-redshift expansion history and to nonminimal physics around photon–baryon decoupling. Finally, Sec. II C demonstrates that the tension between CMB data and BAO data from DESI is generally described as a matter-era distance excess. In particular, we show how this tension manifests as a matter density deficit in standard cosmology that penalizes nonzero neutrino masses.

### A. Theoretical description

The photons observed by large-scale structure surveys traversed a large fraction of their distance during dark energy domination, despite it beginning only a fraction of an  $e$ -fold ago. CMB photons travel a uniquely large distance during matter domination, but still retain a sizeable sensitivity to dark energy. To isolate the (majority of the) impact of matter on distances, we separate the comoving distance  $\chi(a)$  into contributions from during and after the matter era as

$$\chi(a) = \int_a^1 \frac{d \ln \tilde{a}}{\tilde{a}H(\tilde{a})} = \int_a^{a_m} \frac{d \ln \tilde{a}}{\tilde{a}H(\tilde{a})} + \int_{a_m}^1 \frac{d \ln \tilde{a}}{\tilde{a}H(\tilde{a})} \equiv \chi(a, a_m) + \chi(a_m), \quad (2.1)$$

with  $\chi(a_1, a_2)$  denoting the comoving distance interval between  $a_1$  and  $a_2$ ,  $\chi(a) = \chi(a, 1)$ , and  $a_m$  some yet-unspecified scale factor late in the matter era. The matter-era distance interval  $\chi(a, a_m)$  may be approximated (for illustrative if not quantitative purposes) by a Universe without dark energy, while the distance to matter domination  $\chi(a_m)$ , so to speak, requires the full energy content from  $a_m$  to today. We may generalize  $\chi(a_1, a_2)$  in terms of the transverse distance  $D_M \equiv \chi \operatorname{sinc}[\chi/R_k]$ , with  $R_k^2 = -1/\omega_k H_{100}^2$  the curvature radius and  $\omega_k$  the (signed) present density in curvature,<sup>1</sup> via  $D_M(a_1, a_2) \equiv D_M(a_1) - D_M(a_2)$ ; except for in Sec. **III B 3**, we fix a flat Universe and refer to  $\chi$  in such calculations, but we denote measurements from data by  $D_M$ .

### 1. Matter and radiation

In a standard matter–radiation Universe with matter density  $\omega_m$  that equals the radiation density at an equality scale factor  $a_{\text{eq}} = \omega_r/\omega_m$ ,

$$\chi_{mr}(a_d, a_m) = \frac{\sqrt{a_m + a_{\text{eq}}} - \sqrt{a_d + a_{\text{eq}}}}{H_{100}\sqrt{\omega_m}/2}. \quad (2.2)$$

Here we take photon–baryon decoupling ( $a_d$ ) as the high-redshift anchor, anticipating arguments made in Sec. **II B**. At fixed radiation density (or just  $a_{\text{eq}}$  as constrained by the CMB with  $\omega_r$  free), Eq. (2.2) is parametrized by  $\omega_m$  alone. To the extent that low-redshift distances directly constrain the expansion history between the present and the end of the matter era [and therefore  $\chi(a_m)$ ], a geometric measurement of the matter density reduces to inverting Eq. (2.2) for  $\omega_m$ , analogous to that which the distance to last scattering would provide in an Einstein–de Sitter Universe.

If no additional matter components become relevant after decoupling, the size of the Universe in the matter era is determined by the density  $\bar{\rho}_{cb}$  in baryons and CDM. The shape of the temperature and polarization spectra measures  $\bar{\rho}_{cb}(a)/\bar{\rho}_r(a) = a/a_{\text{eq}}$  around last scattering [9, 16, 27, 40–42], setting a baseline expectation for the acoustic scale with  $\omega_m$  determined by  $a_\star^3 \bar{\rho}_{cb}(a_\star) = \omega_{cb}$  with  $a_\star$  the scale factor of peak visibility. In more generality,  $\chi(a_d, a_m)$  is sensitive to physics that modifies the extrapolation of the CMB-calibrated density in dark matter and baryons to the present, i.e., that the total matter density  $\bar{\rho}_m(a \gg a_\star)$  might differ from  $\bar{\rho}_{cb}(a_\star)/(a/a_\star)^3$ . Photons travel furthest when the Universe is largest, making the transverse distances out to any redshift most sensitive to the density in matter at late times. We consider specific models featuring nonminimal dynamics of matter in Sec. **III B** and treat the most important application, massive neutrinos, in Sec. **II A 2**; for our present, illustrative purposes, it suffices to treat the “late-time” matter density (that measured by distances) as an independent parameter without specifying its physical makeup.

To build intuition for these more general scenarios, we employ a simplified treatment in which the matter density instantaneously changes at some scale factor  $a_\times$  after decoupling. Simply treating  $\omega_m = a^3 \bar{\rho}_m(a)/3H_{100}^2 M_{\text{pl}}^2$  (at  $a > a_\times$ ) as a free parameter not necessarily equal to  $\omega_{cb}$ , we apply Eq. (2.2) to write  $\chi(a_d, a_m) = \chi(a_d, a_\times) + \chi(a_\times, a_m)$  and

$$\chi(a_d, a_m) \simeq \frac{\sqrt{a_m} - \sqrt{a_d + a_{\text{eq}}}}{H_{100}\sqrt{\omega_m}/2} \left[ 1 + \left( \sqrt{\frac{\omega_m}{\omega_{cb}}} - 1 \right) \frac{\sqrt{a_\times} - \sqrt{a_d + a_{\text{eq}}}}{\sqrt{a_m} - \sqrt{a_d + a_{\text{eq}}}} \right]. \quad (2.3)$$

For simplicity, we take  $a_m > a_\times \gg a_{\text{eq}}$  (which also hides any small sensitivity to model-dependent changes in the relative amount of matter and radiation). The dependence of Eq. (2.3) on  $a_\times$  is suppressed by the smallness of the change in matter density and any hierarchy in  $a_\times$  and  $a_m$ ; however, the larger  $\sqrt{a_\times/a_m}$ , the more sensitive a measurement of  $\omega_m/\omega_{cb}$  is to the transition (including its noninstantaneous dynamics in any particular scenario).

<sup>1</sup> We parametrize present-day densities with  $\omega_X \equiv \bar{\rho}_{X,0}/3H_{100}^2 M_{\text{pl}}^2$  where  $H_0 = h \cdot 100 \text{ Mpc}^{-1} \text{ km/s} \equiv h H_{100}$ .

The variability of  $a_{\text{eq}}$  and  $a_{\text{d}}$  is a highly subdominant source of uncertainty in Eq. (2.2). (Per above,  $\omega_m$  is not set by  $\omega_r/a_{\text{eq}}$  in general.) That is, since  $a_{\text{eq}} < a_{\text{d}} \ll a_m$ , the relative sensitivities of Eq. (2.2) are  $\partial \ln \chi_{mr}(a_{\text{d}}, a_m)/\partial \ln a_{\text{eq}} \simeq -a_{\text{eq}}/2\sqrt{a_m(a_{\text{d}} + a_{\text{eq}})} \approx -0.008$  and  $\partial \ln \chi_{mr}(a_{\text{d}}, a_m)/\partial \ln a_{\text{d}} \simeq -a_{\text{d}}/2\sqrt{a_m(a_{\text{d}} + a_{\text{eq}})} \approx -0.03$ . The subpercent and (well) subpermille constraints on  $a_{\text{eq}}$  and  $a_{\text{d}}$ , respectively, from current CMB data in  $\Lambda$ CDM thus propagate uncertainty to the MEDI that is subdominant even to the uncertainty in the CMB's acoustic scale information (by respective factors of  $\sim 5$  and  $\sim 50$ ) and do not impede the extraction of matter-era information.

## 2. Massive neutrinos

An increase in the matter abundance after decoupling is an irreducible prediction of standard cosmology and particle physics [11],<sup>2</sup> as neutrinos with mass  $m_{\nu_i}$  (that are light enough to satisfy even the most conservative bounds from the CMB [1, 43]) become nonrelativistic after decoupling at

$$z_{\nu_i} + 1 = 1/a_{\nu_i} = \frac{m_{\nu_i}}{3.15T_{\nu}(a_0)} = 94.3 \frac{m_{\nu_i}}{50 \text{ meV}} \quad (2.4)$$

and have a present-day mass density

$$\omega_{\nu_i} = \frac{3\zeta(3)}{2\pi^2} \frac{m_{\nu_i} T_{\nu}(a_0)^3}{3H_{100}^2 M_{\text{pl}}^2} = \frac{m_{\nu_i}}{93.1 \text{ eV}}. \quad (2.5)$$

Neutrino oscillation experiments require their summed mass  $M_{\nu}$  be at least 0.0588 eV or 0.099 eV in the normal and inverted hierarchies, respectively [44, 45], for a respective total mass density  $\omega_{\nu} = M_{\nu}/93.1 = 6.23 \times 10^{-4}$  or  $1.06 \times 10^{-3}$ . For both hierarchies, at least one mass eigenstate is heavier than 50 meV and therefore becomes nonrelativistic around redshift 94.3. In practice, we follow convention in taking a degenerate mass hierarchy for simplicity and in order to consider mass sums as small as zero, for which reason we do not distinguish between eigenstates below.

Since  $a_{\nu}/a_m$  is not especially small, the impact of neutrino masses on the MEDI decreases superlinearly with smaller neutrino fraction  $f_{\nu} \equiv \omega_{\nu}/(\omega_{\text{cb}} + \omega_{\nu}) \approx M_{\nu}/13.2 \text{ eV} \cdot (\omega_{\text{cb}}/0.142)^{-1}$ . A piecewise approximation in the style of Eq. (2.3) suggests the sensitivity coefficient is roughly  $\partial \ln \chi(a_{\text{d}}, a_m)/\partial f_{\nu} = -(1 - \sqrt{a_{\nu}/a_m})/2$ , which does provide a good estimate. The neutrinos' nonrelativistic transition is rather gradual, however; in Appendix A 1 a we derive an improved analytic result that accounts for this transition, following a perturbative approach described in Sec. III B:

$$\frac{\Delta \chi(a_{\text{d}}, a_m)}{1/H_{100}\sqrt{\omega_{\text{cb}}}} \simeq -f_{\nu}\sqrt{a_m} \left[ 1 + \frac{\sqrt{a_{\nu}/a_m}}{\sqrt{a_{\times}/a_{\nu}}} \left( \frac{7\pi^6 (a_{\times}/a_{\nu})^2}{19440\zeta(3)^2} - \frac{a_{\times}}{a_{\nu}} - 1 \right) + a_{\nu}/a_m \right]. \quad (2.6)$$

Here  $a_{\times}$  is a matching scale factor chosen near  $a_{\nu}$  to minimize errors; Appendix A 1 a describes the rather good accuracy of Eq. (2.6) for  $a_m = 1/(1 + 2.330)$  with  $a_{\times} = 1.32a_{\nu}$ , in which case the numerical coefficient multiplying  $\sqrt{a_{\nu}/a_m}$  is about  $-1.66$ . Equation (2.6) [but not Eq. (A6)] takes  $a_{\text{d}}$  and  $a_{\text{eq}}$  to be negligible compared to  $a_m$  and  $a_{\nu}$  for simplicity's sake.

## 3. Cosmological constant

The express purpose of the matter-era distance interval is to maximally sequester the impact of dark energy on distances. Nevertheless, precision inference is sensitive to the nominally small

<sup>2</sup> The postdecoupling dynamics of hyperlight scalar fields closely resemble those of massive neutrinos; we leave a discussion thereof to Appendix A 1 b.

effects of dark energy, especially since its presence only increases the total density (and decreases distances). Fortunately, the smallness of the effect on the MEDI (in contrast to any individual distance) permits analytic approximations. The comoving distance in a Universe with matter and cosmological constant whose densities are equal at scale factor  $a_{m-\Lambda} = \sqrt[3]{\omega_m/\omega_\Lambda} = \sqrt[3]{\Omega_m/(1-\Omega_m)}$  is [46]

$$\chi(a) = \frac{2}{\sqrt{\omega_m} H_{100}/c} [F_M(1; a_{m-\Lambda}) - F_M(a; a_{m-\Lambda})]. \quad (2.7)$$

Here  $F_M(a; a_{m-\Lambda})$  encodes the correction from  $\Lambda$  to the result for a pure matter Universe [ $F_M(a; a_{m-\Lambda}) \rightarrow \sqrt{a}$  for  $a_{m-\Lambda} \rightarrow \infty$ ] and is given in terms of the hypergeometric function  ${}_2F_1$  by

$$F_M(a; a_{m-\Lambda}) \equiv \sqrt{a} \cdot {}_2F_1(1/6, 1/2; 7/6, -[a/a_{m-\Lambda}]^3) \quad (2.8)$$

$$= \sqrt{a} [1 - (a/a_{m-\Lambda})^3/14 + \mathcal{O}([a/a_{m-\Lambda}]^6)], \quad (2.9)$$

the latter expression indicating the leading-order result in small  $a/a_{m-\Lambda}$ . Comparing Eqs. (2.7) and (2.8) for a matter- $\Lambda$  Universe and Eq. (2.2) for a matter-radiation Universe motivates a factorized ansatz for  $\chi(a)$  that replaces  $\sqrt{a}$  in Eq. (2.8) with  $\sqrt{a + a_{\text{eq}}}$ , which is in fact accurate at the 0.03% level or better. The error from applying the factorized approximation to the MEDI in the form

$$\chi(a_d, a_m) \simeq \frac{[1 - (a_m/a_{m-\Lambda})^3/14] \sqrt{a_m + a_{\text{eq}}} - \sqrt{a_d + a_{\text{eq}}}}{H_{100} \sqrt{\omega_m}/2} \quad (2.10)$$

[neglecting  $(a_d/a_{m-\Lambda})^3 \sim 10^{-9}$ ] is below  $10^{-4}$  at all redshifts  $z_m = 1/a_m - 1 \gtrsim 2$  (i.e., those of interest). Even simply multiplying the matter-radiation result  $\chi_{mr}(a_d, a_m)$  [Eq. (2.2)] by the approximate correction in Eq. (2.9) achieves comparable accuracy. We generalize this result beyond a cosmological constant in Sec. III D 1.

The coefficient 1/14 in Eq. (2.10) affirms the suppressed sensitivity of the integrated distance to dark energy's instantaneous contribution to the energy density. For instance, the fiducial  $\sim 5.7\%$  contribution at  $z_m = 2.330$  (for DESI DR2's Lyman- $\alpha$  sample) corresponds to a 0.4% effect on  $\chi(a_d, a_m)$ . Taking the matching redshift  $z_m$  to be the highest redshift measured by BAO distances thus serendipitously compartmentalizes the support of the distance to decoupling into the interval that is directly measured from tracers of large-scale structure [ $\chi(a)$  for  $a < a_m$ ] and that which depends almost exclusively on matter [ $\chi(a_d, a_m)$ ]. Dark energy's nominal half-percent effect is of course not irrelevant for deriving subpercent measurements of the matter density (or other effects on the MEDI), but it does indicate a large hierarchy in information.<sup>3</sup> That is, while  $\partial \ln \chi(a_d, a_m)/\partial \ln \omega_m = -1/2$ , the sensitivity to dark energy drops with its density fraction and is further suppressed by the smallness of its contribution to the full MEDI:  $\partial \ln \chi(a_d, a_m)/\partial \ln \Omega_{\text{DE}}(a_m) \simeq \Omega_{\text{DE}}(a_m)/14$ , smaller than the former by more than a factor of 100. Lower-redshift distances  $\chi(a)$ , however parametrized, necessarily have order-unity sensitivity to dark energy.

## B. Measurement from the acoustic scale

We proceed by devising model-independent measurements of the matter-era distance interval. Redshift surveys extract distances from the acoustic scale via the transverse and longitudinal scales

$$\theta_\perp(a) \equiv r_d/D_M(a) \quad (2.11a)$$

$$\theta_\parallel(a) \equiv r_d/cH(a)^{-1} \equiv r_d/D_H(a), \quad (2.11b)$$

<sup>3</sup> The logarithmic sensitivities we quote translate the relative precision of the measurement to the relative precision of the resulting parameter constraint.

or, when sample statistics preclude separate measurements thereof, a volume average of the two,

$$\theta_{\text{BAO}}(a) \equiv \sqrt[3]{\theta_{\perp}(a)^2 \theta_{\parallel}(a) (1/a - 1)}. \quad (2.11c)$$

Here  $r_{\text{d}}$  is the sound horizon at baryon decoupling,  $a_{\text{d}}$ . The MEDI is best measured by the difference in distance to photon–baryon decoupling as inferred from the CMB and to some scale factor  $a_m$  later in the matter era from, say, BAO, taking the form  $D_M(a_{\text{d}}, a_m)/r_{\text{d}} = 1/\theta_{\perp}(a_{\text{d}}) - 1/\theta_{\perp}(a_m)$ . Since the high-redshift end is supplied by the CMB, of which there is only a single (and exceedingly precise) realization, the problem reduces to measuring the distance to matter domination, loosely defined. We next discuss how the CMB (i.e., the photon distribution) constrains the acoustic feature in the baryon distribution at decoupling, the measurements of  $D_M(a_m)/r_{\text{d}}$  from BAO data, and the implications of the drag horizon serving as a distance calibrator.

### 1. Distance to decoupling

We denote the CMB’s transverse distance measurement by  $\theta_{\perp}(a_{\text{d}})$ , which is not the conventional  $\theta_s = r_s(a_{\star})/D_M(a_{\star})$  (with  $a_{\star}$  the scale factor of peak photon visibility) but rather  $r_{\text{d}}/D_M(a_{\text{d}})$ . We phrase the CMB’s acoustic scale information via the so-called drag horizon, i.e., the sound horizon evaluated when baryons (rather than photons) decouple from Thomson scattering, because it is measured nearly as well as (and is tightly related to [47]) the photon sound horizon and is directly comparable with BAO measurements from the galaxy distribution [7]. Working with  $\theta_{\perp}(a_{\text{d}})$  rather than  $\theta_s$  is thus significantly more convenient, though not necessary. Any model that breaks the strong correlation between the acoustic scale that imprints in the photon and baryon distributions would be a candidate explanation of the BAO–CMB tension (see Ref. [48] for an example).

The CMB’s geometric information is completely insensitive to the postdecoupling expansion history and is usually quite insensitive to modified physics before decoupling, with a notable exception being the radiation content (i.e., the fraction of radiation that freely streams) [49, 50]. Even in this case, the impact on  $\theta_{\perp}(a_{\text{d}})$  is marginal, and, moreover, it is accompanied by a different calibration of the MEDI; we therefore defer a discussion thereof to Sec. III A. For most of the scenarios we consider, the CMB robustly constrains  $1/\theta_{\perp}(a_{\text{d}}) = 94.304 \pm 0.028$ , which is also largely uncorrelated with the MEDI that it calibrates in  $\Lambda$ CDM.

### 2. Distance to matter domination

DESI directly measures distances at redshift 2.330 via its current Lyman- $\alpha$  forest sample. DESI DR2’s Lyman- $\alpha$  measurement at  $z = 2.330$ , marginalized over its longitudinal distance, is  $D_M(1/[1 + 2.330])/r_{\text{d}} = 38.988 \pm 0.531$  [51], while combining DR2 BAO with the Alcock–Paczynski (AP) effect from DR1 yields  $D_M(1/[1 + 2.330])/r_{\text{d}} = 38.90 \pm 0.38$  [52]. Though the resulting 0.7% measurement of the MEDI is completely independent of cosmological dynamics (up to the well-established assumptions involved in the derivations of the individual distances), it is insufficiently precise to be of practical use (having uncertainty larger, for instance, than the impact of a cosmological constant quoted in Sec. II A 3). Including additional data from lower redshifts enables better constraints on  $\theta_{\perp}(a_m)$  that can reduce this uncertainty, so long as one specifies a model for the low-redshift Universe to enable its inference.

Even with relatively arbitrary freedom, lower-redshift data stand to contribute meaningfully to the inference of  $\theta_{\perp}(a_m)$ . Transverse distance data constrain the accumulation of distance along the line of sight  $\sim \int_0^a d\tilde{a}/\tilde{a}H(\tilde{a})$ , while longitudinal data constrain the instantaneous rate  $\sim 1/aH(a)$  of propagated distance, i.e., between DESI’s different samples. As illustrated in Fig. 1, the longitudinal

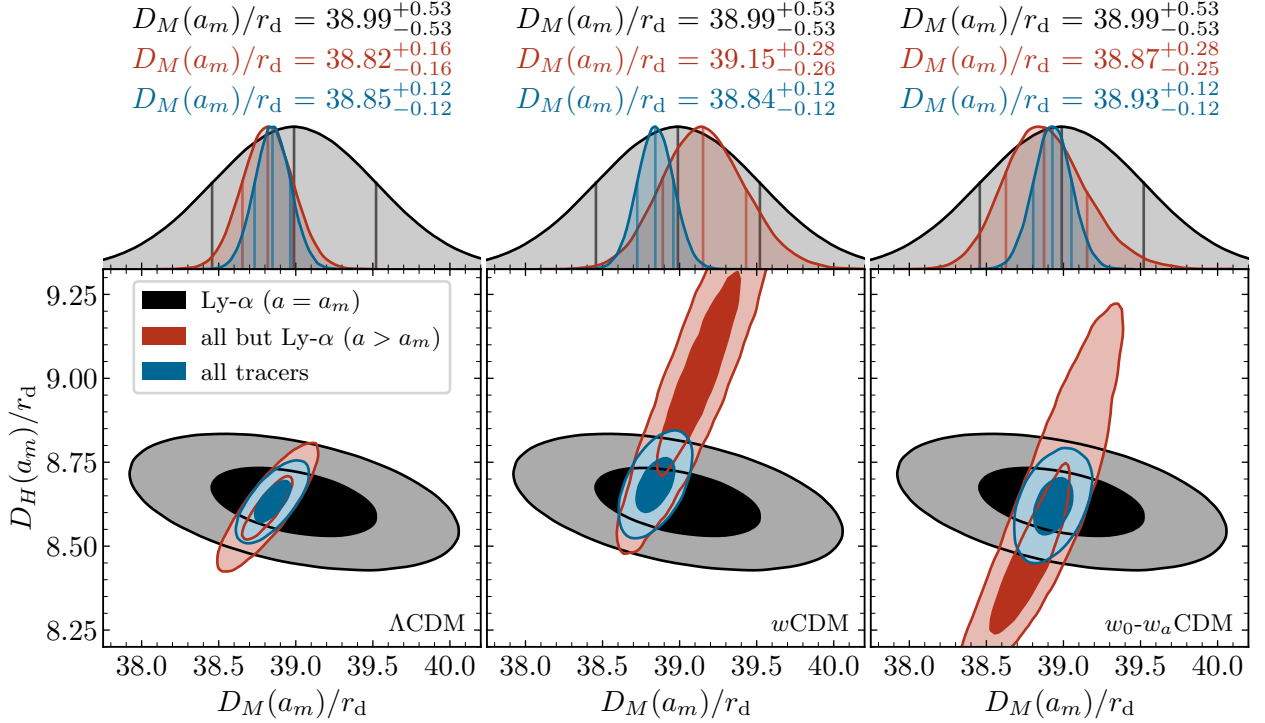


Figure 1. Robustness of the jointly inferred distance to DESI DR2’s highest-redshift BAO tracer (Lyman- $\alpha$  at  $z_m = 2.330$  [51]) to increasing dynamical freedom of dark energy (by panel as labelled). The Lyman- $\alpha$  likelihood (whose 1 and  $2\sigma$  mass levels appear in black) combines with the predictions of each model as calibrated to all lower-redshift DESI data (red) to yield joint measurements (blue) of the transverse distance  $D_M(a_m)/r_d$  with more than four times the precision of the direct one. The Lyman- $\alpha$  sample’s transverse measurement is in fact almost completely irrelevant: its most important role is rather to constrain the expansion rate  $[D_H(a_m)/r_d]$  at high redshift and therefore how much distance photons accumulate from lower redshift (as measured by the observations at lower redshift).

measurement limits the allowed range of densities between DESI’s Lyman- $\alpha$  sample and the next highest-redshift sample. (See Appendix A 2 for details on parameter sampling methods.) Combined, the longitudinal data regularize the amount of distance photons can accumulate between the Lyman- $\alpha$  sample and the next highest-redshift bin, the distance to which is itself well measured (the argument continuing by induction). The longitudinal Lyman- $\alpha$  measurement breaks the degeneracy between  $D_M(a_m)/r_d$  and  $D_H(a_m)/r_d$  from the lower- $z$  data, resulting in a joint constraint on  $D_M(a_m)/r_d$  more precise than the direct measurement by a factor greater than four.<sup>4</sup>

Figure 1 also demonstrates the robustness of this inference of  $D_M(a_m)/r_d$  to increasing freedom in the dark-energy equation of state (as a proxy for freedom in the low-redshift expansion history). The uncertainty is unchanged, while only under the linear-in- $a$  (or  $w_0-w_a$ ) equation of state model [53, 54] does the median shift at all, and only by  $0.66\sigma$  toward the mean of the direct measurement. Experiments with fitting an arbitrarily evolving dark energy density [as splines of  $\ln \bar{\rho}_{DE}(\ln a)$ ] yield results quite similar to the  $w_0-w_a$  result, so long as no more than one node lies between each DESI measurement (otherwise, the two degrees of freedom are sufficient to fit two measurements from the next-highest redshift independently of the fit at lower redshift).

<sup>4</sup> Including the aforementioned AP effect measurement from DESI DR1 data [52], which improves the direct measurement of  $D_M(a_m)/r_d$  to 1% precision, has no effect on the jointly inferred measurement—a testament to the irrelevance of the direct transverse information.

### 3. Drag horizon as units

By and large, acoustic scale measurements themselves are independent of early-Universe dynamics [55], in that the relevant information is robustly compressed by the usage of the drag horizon as the “ruler” for an intrinsically dimensionless observable. The  $\Lambda$ CDM prediction for the MEDI [Eq. (2.10)] measured from the acoustic scale is approximately

$$\frac{\chi(a_d, a_m)}{r_d} \simeq \frac{[1 - (a_m/a_{m-\Lambda})^3/14] \sqrt{a_m + a_{\text{eq}}} - \sqrt{a_d + a_{\text{eq}}}}{H_{100} \sqrt{\omega_m} r_d / 2}. \quad (2.12)$$

The dependence of Eq. (2.12) (and all acoustic scale observables) on absolute densities and the drag horizon always arises in combinations like  $\omega_m r_d^2$  [7, 9]. In most of our analyses, we therefore treat the drag horizon as setting units for distances and densities. Comparing dimensionless distances that share common units avoids any problems of calibration, repackaging the dependence of the observable on predecoupling physics in a manner that is maximally compartmentalized from postdecoupling dynamics.

Measuring dimensionful length scales (from which absolute cosmological densities may be inferred) with the acoustic scale requires modeling (and calibrating) the drag horizon, which we return to in Sec. III A. Absolute rather than relative densities, however, are only of interest for comparison with the inference of other, independent observables that do not share the same calibration, such as local measurements of the Hubble constant [56–58] or laboratory limits on the neutrino mass sum [44, 45]. Notably, the aforementioned strong correlation between the acoustic scale in the photon and galaxy distributions [7, 47] implies that BAO and CMB observations do share a common ruler; in effectively full generality, their agreement or disagreement may be quantified without reference to dimensionful values. A miscalibrated drag horizon therefore cannot (on its own) explain the tension between BAO and CMB data nor their joint incompatibility with neutrino masses (as has been claimed), a subtlety which we elaborate on further in Sec. III A.

### C. The BAO–CMB tension as a matter-era distance excess

We now show that the matter-era distance interval effectively summarizes the present tension between DESI’s BAO measurements and CMB observations.<sup>5</sup> This tension may be equivalently understood either by comparing BAO measurements to the low-redshift distances extrapolated by the CMB or by comparing the matter-era distance interval measured by the acoustic scale (from both BAO and the CMB) with that predicted by the shape of the CMB anisotropy spectra. The former maintains the separation of BAO and CMB likelihoods by studying the CMB’s prediction for  $D_M(a_m)/r_d$  in the form  $1/\theta_\perp(a_d) - D_M(a_d, a_m)/r_d$ , which in  $\Lambda$ CDM is fully calibrated by physics before decoupling (up to the small impact of dark energy). From this point of view, our results below show that the tension can be effectively reduced to one in this single distance as jointly inferred by low-redshift measurements (see Sec. II B 2) and as independently predicted by the CMB.

The latter description instead separates the more direct distance measurements from the acoustic scale by rearranging the comparison to the matter-era distance interval  $D_M(a_d, a_m)$  itself, as motivated by the typical insensitivity of  $\theta_\perp(a_d)$  to dynamics after decoupling and its negligible correlation with the extrapolated MEDI. Certain exceptional cases featuring particular effects on the dynamics of the plasma before decoupling do modify the inference of  $\theta_\perp(a_d)$  (see Sec. III A 2), for which the previous formulation is more apt, but the MEDI isolates the observable that is most

<sup>5</sup> Throughout this work, the CMB dataset we employ is always a combination from *Planck* [59], the Atacama Cosmology Telescope [2], and the South Pole Telescope [3]; see Appendix A 2.

sensitive to all postdecoupling (and numerous predecoupling) extensions of  $\Lambda$ CDM. This description thus inherits the advantages of the MEDI’s analytic tractability and physical transparency by compartmentalizing model-independent measurements from the acoustic scale and model-dependent predictions from high-redshift physics.

Moreover, as shown in Sec. II A, the matter-era distance interval (as predicted by the CMB) is almost fully determined by the matter density in  $\Lambda$ CDM, suggesting that the matter density deficit evident from DESI and CMB data [7, 22] implies a matter-era distance excess. In Sec. II C 1, we demonstrate the converse: by applying the analytic results of Sec. II A to interpret the joint inference of the late-time matter density from the acoustic scale, we show that even in  $\Lambda$ CDM the MEDI contains most of the information thereof. A matter-era distance excess is therefore the generalized statement of tension from BAO and CMB data. We explain the CMB side of the tension in Sec. II C 2, highlighting the role of massive neutrinos in the predicted MEDI, and we also discuss the general implications of our analysis for solutions to the excess.

### 1. Matter density measurements

We now investigate the relative importance of the matter-era distance interval and of individual BAO distance measurements in determining the matter density at late times. We derive measurements of the matter density from the MEDI alone analytically using Eq. (2.3), exploiting the large hierarchy in information to treat a likelihood for the MEDI as a posterior for  $\omega_m r_d^2$  that is conditioned on (rather than jointly distributed with)  $a_{\text{eq}}$ ,  $a_{m-\Lambda}$ , and  $\omega_{cb} r_d^2$ , while still marginalizing over these parameters drawn from independent priors. In other words, we propagate the uncertainty in these parameters to the matter density  $\omega_m r_d^2$  inferred from the MEDI while neglecting the (highly) subdominant information the likelihood adds for parameters other than  $\omega_m r_d^2$ . We take a brute-force sampling approach, which is less cumbersome than analytically propagating the uncertainty from the prior distribution but is still analytic in the sense of solving the likelihood for  $\omega_m r_d^2$  rather than sampling parameters from it (e.g., with Markov chain Monte Carlo methods).

In more detail, to account for the effects of radiation and cosmological constant, we sample  $a_{m-\Lambda}$  and  $a_{\text{eq}}$  from conservative priors—namely,  $a_{m-\Lambda} \sim \mathcal{N}(0.75, 0.02)$  [double the uncertainty from DESI DR2 alone and quadruple that when including the CMB’s  $\theta_{\perp}(a_d)$ ] and  $3401 a_{\text{eq}} \sim \mathcal{N}(1, 0.032)$  (four times broader than that inferred by CMB data). This procedure is additionally conservative in neglecting any correlation between these parameters and with  $\omega_m r_d^2$ . Combined, these priors propagate just 0.047% uncertainty at any fixed value of  $\omega_m r_d^2$ . We then sample  $\theta_{\perp}(a_d)$  and  $\omega_{cb} r_d^2$  from a joint CMB prior. Finally, we draw  $\log_{10} a_{\times} \sim \mathcal{U}(-3, -2.75)$ , which contributes negligibly to the uncertainty, in order to roughly match measurements in  $\Lambda$ CDM that fix the matter abundance  $a^3 \bar{\rho}_m$  at all redshift. (The resulting MEDI is therefore quite insensitive to  $\omega_{cb} r_d^2$ .) We then analytically solve for  $\omega_m r_d^2$  by inverting Eq. (2.3) with whatever given sample of  $D_M(a_d, a_m)/r_d$ .

Figure 2 demonstrates how the MEDI measures the matter density in  $\Lambda$ CDM. We start by analyzing the “distance to matter domination”  $D_M(a_m)/r_d$ , keeping BAO and CMB information as separate as possible, and then translate to the acoustic scale measurement of the MEDI. We compare the posterior over  $D_M(a_m)/r_d$  and  $\omega_m r_d^2$  derived from DESI DR2 data alone and all acoustic scale data [including  $\theta_{\perp}(a_d)$  from the CMB]. Following the above analytic procedure, we sample the MEDI from a broad, uniform distribution to depict the joint distribution of  $\omega_m r_d^2$  and  $D_M(a_m)/r_d$  compatible with the conservative prior described above. (One could equivalently draw  $\omega_m r_d^2$  from a uniform distribution and then compute the MEDI.) Finally, we draw values of the MEDI from the acoustic scale measurement, i.e.,  $1/\theta_{\perp}(a_d)$  drawn from the CMB prior minus DESI’s marginalized measurement of  $D_M(a_m)/r_d$ , and apply the analytic procedure to infer the matter density from the MEDI alone. The right axis of Fig. 2 illustrates the corresponding values of the MEDI, neglecting

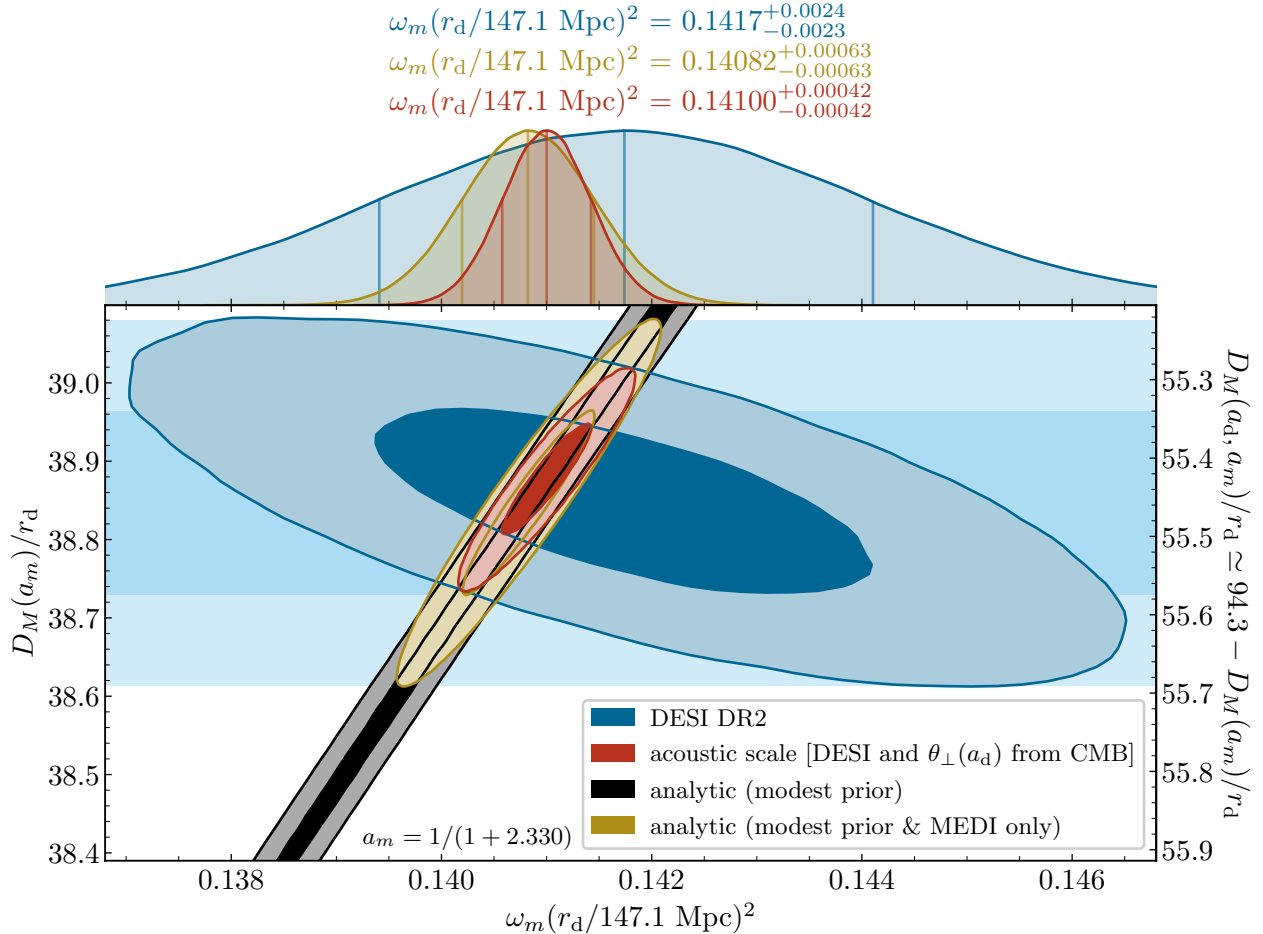


Figure 2. Measurements of the late-time matter density  $\omega_m r_d^2$  from the acoustic scale and the matter-era distance interval  $D_M(a_d, a_m)/r_d \equiv D_M(a_d)/r_d - D_M(a_m)/r_d$ . The 1 and  $2\sigma$  mass levels of the joint distribution over  $\omega_m r_d^2$  and  $D_M(a_m)/r_d$  deriving from DESI DR2 and from all acoustic scale data (i.e., DESI and the CMB’s geometric information) appear in blue and red, respectively. Black and gold regions depict results computed analytically with a minimal prior as described in the main text, with the MEDI respectively drawn from a broad, uniform distribution and computed as the difference of the CMB’s measured  $1/\theta_\perp(a_d)$  and DESI’s measured  $D_M(a_m)/r_d$  (horizontal blue bands); the latter represents an acoustic scale measurement agnostic to dynamics at  $a > a_m$ . The right axis depicts the MEDI corresponding to  $D_M(a_m)/r_d$ , taking the CMB’s mean  $1/\theta_\perp(a_d)$  (neglecting its small uncertainty). Comparing the marginal measurements of the matter density demonstrates the critical role of the MEDI and the relative unimportance of DESI’s matter density information from late times ( $a > a_m$ ).

the subdominant uncertainty in  $1/\theta_\perp(a_d)$ ; the red and blue posteriors then represent results from all acoustic scale data that respectively model the expansion history consistently at all redshift and are agnostic to it at  $z > z_m = 2.330$ .

Figure 2 evidences the critical role of the CMB’s geometric information in the inference of the late-time matter density. Even in a model with as little freedom as  $\Lambda$ CDM, with only one additional relevant parameter ( $\Lambda$ ) constrained by 13 percent-level data points, DESI’s measurement of the matter density is dwarfed by that from the matter-era distance interval alone. One could interpret this exercise as modeling the expansion history with the matter abundance taking independent values below and above  $z_m$ , whose respective measurements are that obtained by DESI alone and that from the MEDI alone. The full measurement from all acoustic scale data (modeled consistently) is only 1.5 times more precise than the MEDI’s, deriving from the mild correlation between DESI’s

inference of  $\omega_m r_d^2$  and  $D_M(a_m)/r_d$ . Artificially increasing DESI’s preferred matter density would have only a minor effect on the joint measurement compared with instead increasing its measured distance to  $z = 2.330$  (i.e., decreasing the MEDI). Freedom in the equation of state of dark energy, which we discuss further in Sec. III D 1, largely decorrelates the two, such that the MEDI represents nearly the totality of the information on the matter density.

## 2. From density deficit to distance excess

Section II C 1 establishes that analyzing the full set of acoustic scale observations from BAO and the CMB, in particular through the matter-era distance interval, is key to physically interpret their combination (or tension). The remaining information from the CMB—from the shape of the anisotropy spectra—calibrates the densities in all species relevant around and before photon–baryon decoupling (within any given model) and thus predicts the MEDI by extrapolating those densities to late times. In the  $\Lambda$ CDM model with massless neutrinos, the CMB measures  $\omega_{cb}(r_d/147.1 \text{ Mpc})^2 = 0.14224 \pm 0.00061$  and therefore predicts  $D_M(a_d, a_m)/r_d = 55.2 \pm 0.11$  as a baseline expectation. The measurements of the MEDI in Fig. 2, whether marginalized over DESI’s matter density information or not, exceed this prediction by about  $1.7\sigma$ . That the tension must be understood as between the acoustic scale and the shape of the CMB rather than between the CMB and DESI itself is best evidenced by the irrelevance of DESI’s independent inference of the matter density,  $\omega_m r_d^2 = 0.1417 \pm 0.0024$ , whose  $\pm 1\sigma$  interval encompasses the CMB’s  $-5\sigma$  and  $+3\sigma$  limits of  $\omega_{cb} r_d^2$ .

Comparing the measured MEDI to CMB predictions in the base  $\Lambda$ CDM model, however, understates the severity of the tension, given that neutrinos (with masses compatible with neutrino oscillations) must increase the late-time matter density by at least a half percent over that from CDM and baryons alone. To fully quantify the  $M_\nu$ -marginalized matter-era distance tension, Fig. 3 compares complete CMB predictions within  $\Lambda$ CDM (under various assumptions on neutrino masses) to acoustic scale measurements (under various assumptions on the expansion history). The CMB predictions in Fig. 3 do not include lensing reconstruction data, simply to avoid adding more late-time information that might be modified by any physics invoked to modify the predicted MEDI; we comment on the lensing information intrinsic in temperature and polarization anisotropies in Sec. III A 3. In the most minimal and motivated case (a cosmological constant and  $M_\nu$  compatible with neutrino oscillations), the tension between the acoustic scale and the prediction extrapolated by the CMB is  $2.6\sigma$ , degrading only by about  $0.5\sigma$  if taking dynamical dark energy at  $z < z_m$  or allowing sub-59 meV neutrinos.<sup>6</sup> For comparison, the tension between DESI and the CMB in  $\Lambda$ CDM, quantified as the difference in posterior mean vectors  $(\omega_m r_d^2, \Omega_m)$  with the summed covariance serving as the metric, is about the same size.

An analytic approach like that used to measure the late-time matter density in Sec. II C 1 is less apt to measure neutrino masses, as the MEDI likelihood peaks at distances longer rather than shorter than the CMB prediction even for massless neutrinos—that is, most of its probability mass would be cut off by the prior that  $M_\nu$  is nonnegative. We may, however, reliably estimate the increase in tension from any *fixed* neutrino mass sum by adding Eq. (2.6) to the CMB’s aforementioned prediction with massless neutrinos, and computing the tension with the high-redshift–agnostic acoustic scale measurement of  $55.46 \pm 0.12$  in Fig. 3.<sup>7</sup> Series expanding Eq. (2.6) about  $M_\nu = 59 \text{ meV}$  and taking a fiducial  $r_d = 147.1 \text{ Mpc}$ , we find that the matter-era distance

<sup>6</sup> The degenerate mass hierarchy is least accurate for mass sums closest to the minimum, which dominate the posterior’s mass density. The effect on the MEDI, however, is quite small: summing each mass eigenstate’s contribution using Eq. (2.6), the modification to the sensitivity coefficient multiplying  $f_\nu$  is  $\sim 10\%$  at most, rapidly diminishing with larger  $M_\nu$ . The degenerate hierarchy thus remains suitable, as tested explicitly by Ref. [60].

<sup>7</sup> In doing so, we ignore any adjustment to the CMB’s inferred  $\omega_{cb} r_d^2$ , etc., in response to the suppression of the lensing amplitude by massive neutrinos at late times. Marginalizing over  $M_\nu > 0$  only shifts the CMB’s preferred  $\omega_{cb} r_d^2$  upward by just  $0.2\sigma$ , so this approximation only slightly underestimates the increase in tension.

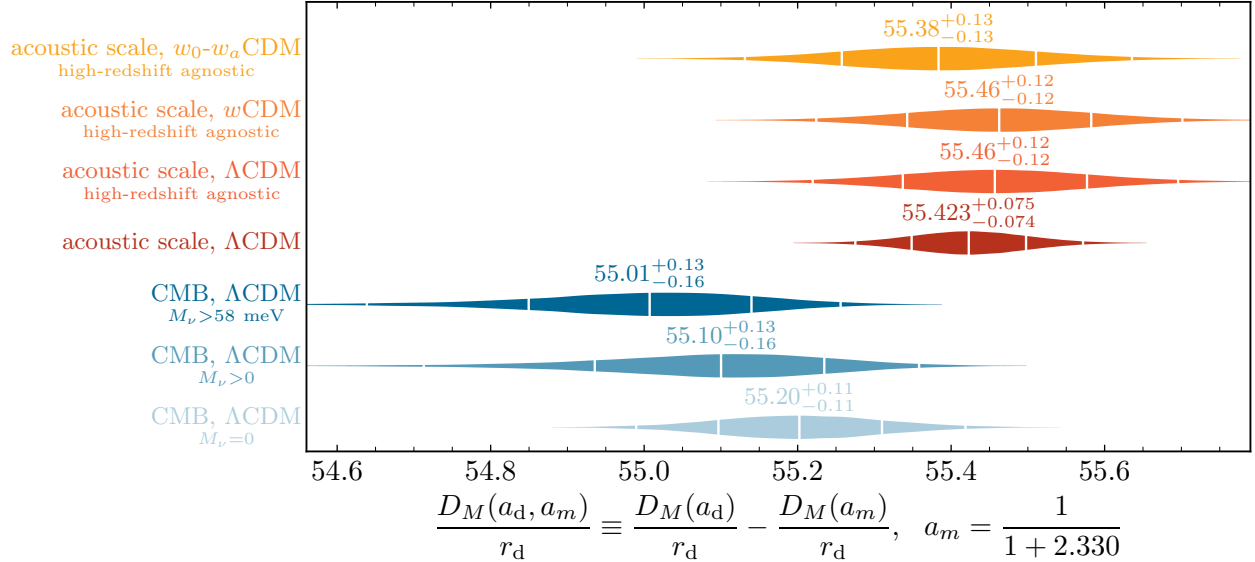


Figure 3. Quantification of the matter-era distance excess that underlies the BAO–CMB tension, i.e., between CMB predictions and acoustic scale measurements of the matter-era distance interval. Blue posteriors depict  $\Lambda$ CDM predictions calibrated by CMB temperature and polarization data from *Planck* PR3, ACT DR6, and SPT-3G D1, either fixing the neutrino mass sum to zero, marginalizing it over nonnegative values, or marginalizing it over values compatible with neutrino oscillations; these results depend only on nongeometric information. Red/orange results indicate measurements from the acoustic scale, with the darkest red indicating the constraint in standard  $\Lambda$ CDM from DESI DR2 data and the CMB’s geometric information  $[1/\theta_{\perp}(a_d)]$  alone, in noticeable tension with the prediction from the CMB’s nongeometric information. Lighter shades display more conservative results that assume nothing about the expansion history at  $z > z_m$ , instead taking  $D_M(a_d)/r_d$  from the CMB’s fully marginalized measurement of  $1/\theta_{\perp}(a_d)$ . The low-redshift expansion history is then modeled under varying assumptions in order to combine all DESI data to measure the “distance to matter domination”  $D_M(a_m)/r_d$ , taking a cosmological constant, a dark energy fluid with fixed equation of state, or one with equation of state evolving linearly with  $a$ . These results thus represent measurements of the matter-era distance interval that are independent of physics between  $a_m$  and  $a_d$ , which remain in tension with the CMB’s predictions thereof, especially when massive neutrinos are properly accounted for.

tension is about  $[2.06 + (M_{\nu} - 59 \text{ meV})/97 \text{ meV}] \sigma$ . The minimum mass sums for the normal and inverted mass hierarchies thus increase the tension to  $2.1\sigma$  and  $2.5\sigma$ , respectively.

The matter-era distance interval enables a generalized description of the geometric sensitivity of CMB and BAO data to neutrino masses. In  $\Lambda$ CDM, the steep increase in the matter fraction (or increase in  $a_{m-\Lambda}$ ) with  $M_{\nu}$  required to fix the distance to last scattering enables photons to travel far enough during dark energy domination to compensate for the reduced horizon during matter domination [7]. BAO data break this degeneracy largely by directly measuring  $a_{m-\Lambda}$ , thereby determining the relative amount of distance traveled in each era. The MEDI generalizes this logic: BAO data at low redshift measure the distance to matter domination (Sec. IIB 2) and thus also the remaining portion of the distance to last scattering that accrued deep in the matter era. The arguments of this section show that the majority of the information (and the present geometric tension) originates in the latter portion.

Recently, Ref. [61] attempted to quantify the geometric tension between the CMB and BAO data by introducing an effective, signed neutrino mass parameter. Their model, however, only modifies low-redshift distances for BAO and not the CMB itself (i.e., not its own geometric information) and therefore does not capture the main effect (on the MEDI). The distance to last scattering in their treatment is a function of  $\omega_{cb} r_d^2$  and  $\Omega_m$  alone as in  $\Lambda$ CDM; with the former well measured

by the shape of the CMB spectra,  $\theta_s$  measures  $\Omega_m$  (rather, the dark energy density) independent of this effective neutrino mass. Imposing this effective prior on  $\Omega_m$  thus artificially sharpens the measurement of the full late-time matter density (including the effective, neutrino-like contribution) from low-redshift BAO data. Such a measurement does not reflect the actual physical origin of the acoustic scale’s sensitivity to neutrino masses (nor any consistent cosmological model<sup>8</sup>), as underscored by the importance of the matter-era distance interval—namely, the physical inputs that modify its prediction, rather than the low-redshift BAO distances themselves.

The matter-era distance excess persists even if the acoustic scale measurement is made fully agnostic to dynamics at  $a < a_m$ . When simply taking  $D_M(a_d)/r_d = 1/\theta_\perp(a_d)$  as measured by the CMB independent of all other parameters (rather than jointly modeling and fitting it), the measured MEDI only shifts slightly higher (see Fig. 3), with precision degrading by a factor of 1.6 (with size similar to the CMB’s uncertainty). In  $\Lambda$ CDM, this exercise effectively allows the matter abundance to differ above and below  $a_m$ , with the improvement in precision deriving from imposing that the values match as illustrated in Fig. 2. Furthermore, the robustness of the high-redshift-agnostic MEDI measurements from the acoustic scale to dark energy dynamics demonstrates that the excess is far more likely to be explained by dynamics at high redshift ( $z > z_m$ ) than at low redshift.<sup>9</sup>

### III. HIGH-REDSHIFT SOLUTIONS

Given that DESI itself is compatible with quite a broad range of matter densities (i.e., as inferred from its low-redshift distances alone), Sec. II C shows that solving the matter-era distance excess would leave DESI compatible with rather heavy neutrinos, even if the Universe were completely described by  $\Lambda$ CDM at low redshift. The robustness of the matter-era distance interval measured by the acoustic scale, as evident in Fig. 3, leaves little room to resolve or even alleviate the matter-era distance tension by modifying the distances predicted at  $z \leq z_m$ . Conversely, the sensitivity of the CMB’s prediction to assumptions on neutrino masses reflects the MEDI’s importance in constraining the expansion history after photon–baryon decoupling more broadly. The baseline expectation for the MEDI from the CMB is also sensitive to dynamics before decoupling insofar as they determine the densities in baryons and CDM (relative to the sound horizon).

We now consider what nonstandard physics before (Sec. III A) and after (Sec. III B) decoupling may modify the CMB prediction and resolve the matter-era distance tension. We summarize their implications for neutrino masses in Sec. III C. Finally, in Sec. III D we show that dynamical dark energy addresses the matter-era distance excess not through its dynamics at late times (as already evident in Fig. 3) but at high redshift. We demonstrate that the alternative solutions to the excess from Secs. III A and III B reduce the evidence for dark energy dynamics and identify the features in DESI’s data that underlie the residual preference.

#### A. Predecoupling physics

In general, parametrizing the overall, dimensionless amplitude of acoustic scale observables in terms of  $\omega_m r_d^2$  (rather than the more conventional  $hr_d$ ) more transparently identifies its dependence on early-Universe physics (rather than dark energy) [7, 9]. This advantage is especially clear for the matter-era distance interval, as the distance photons travel during matter domination is (by definition) independent of dark energy and the present-day expansion rate. In  $\Lambda$ CDM, the CMB

<sup>8</sup> CMB photons and photons emitted by tracers of structure accumulate the same distance out to the redshifts observed by BAO surveys. In effect, the model of Ref. [61] imposes some modification to the expansion history at high redshift that exactly cancels the shift in distance induced by their effective neutrino density at low redshift.

<sup>9</sup> The MEDI measurements in  $\Lambda$ CDM from DESI DR1 [8] and the Sloan Digital Sky Survey [62, 63], using the same CMB prior on  $\theta_\perp(a_d)$ , are  $55.46 \pm 0.12$  and  $55.24^{+0.14}_{-0.13}$ , respectively; the high-redshift-agnostic counterparts are  $55.49 \pm 0.2$  and  $55.11 \pm 0.28$  and are robust to dark energy dynamics to an extent similar to that from DESI DR2.

measures  $\omega_{cb}r_d^2$  even better than it measures  $\omega_{cb}$ , setting a baseline expectation for the MEDI (the  $M_\nu = 0$  result in Fig. 3). In this section, we generalize this statement to models that modify the CMB’s calibration of the MEDI and explain why the actual value of the drag horizon is not uniquely relevant to the present tension between DESI’s measurements and the CMB, as has been suggested previously [39, 64, 65]. We explain what features of predecoupling physics genuinely modify acoustic scale predictions, following arguments from Refs. [7, 16].

We begin by reviewing how the CMB calibrates the density in matter components. The CMB anisotropy spectra are dimensionless observables and therefore only measure density ratios [9, 16, 40, 41]; furthermore, the anisotropies generated at last scattering depend on density ratios evaluated at that epoch, not the present [16, 27]. The shape of the temperature and polarization spectra measures the matter-to-radiation ratio  $\bar{\rho}_{cb}(a)/\bar{\rho}_r(a)$  around last scattering, primarily via the radiation-driving and early integrated Sachs–Wolfe effects [16, 27, 40–42, 66, 67]. This information is effectively summarized by the radiation-matter ratio evaluated at peak visibility,

$$x_{\text{eq}} \equiv \frac{\bar{\rho}_r(a_\star)}{\bar{\rho}_m(a_\star)} = \frac{\omega_r}{\omega_{cb}a_\star} = \frac{a_{\text{eq}}}{a_\star}, \quad (3.1)$$

which, for standard matter and radiation, reduces to the amount of expansion between matter–radiation equality and last scattering. The acoustic peak structure and damping tail also measure the baryon-to-photon ratio [66–68]

$$R_\star \equiv \frac{3\bar{\rho}_b(a_\star)}{4\bar{\rho}_\gamma(a_\star)} \propto \frac{3\omega_b a_\star}{4\omega_\gamma}. \quad (3.2)$$

The CMB precisely measures  $R_\star$  and  $x_{\text{eq}}$  (respectively reaching 0.44% and 0.77% precision from the latest combination of *Planck*, ACT, and SPT temperature and polarization data [1–3]) and does so robustly in a range of extended cosmologies [7, 16].

The sound horizon depends on the baryon and CDM densities only via  $R_\star$  and  $x_{\text{eq}}$  [7, 16, 69]:

$$r_s(a) = \frac{a_\star}{\sqrt{\omega_r}} \frac{2\sqrt{x_{\text{eq}}/3R_\star}}{H_{100}/c} \ln \left( \frac{\sqrt{R_\star}\sqrt{x+x_{\text{eq}}} + \sqrt{1+R_\star x}}{1 + \sqrt{R_\star x_{\text{eq}}}} \right), \quad (3.3)$$

where  $x \equiv a/a_\star$ .<sup>10</sup> Its dimensionful value is thus determined by the calibration of the radiation density  $\omega_r \equiv a_\star^4 \bar{\rho}_r(a_\star)/3H_{100}^2 M_{\text{pl}}^2$ , i.e., the density in relativistic species at last scattering translated to the present,<sup>11</sup> but this dependence is absorbed into a dimensionless ratio in acoustic scale observables [i.e.,  $D_M(a)/r_d$  and  $D_H(a)/r_d$ ]. Evaluating the drag horizon  $r_d \equiv r_s(a_d)$  from Eq. (3.3) also requires the ratio of the temperatures of photon and baryon decoupling,  $x_d = a_d/a_\star = T_\star/T_d$ , which in  $\Lambda$ CDM is strongly constrained ( $1.0270 \pm 0.0003$ ) and also varies little in extensions [7, 47]. For this reason, the drag scale  $D_M(a_d)/r_d$  provides nearly as precise a summary statistic for the CMB’s geometric information as the photon sound horizon does via  $D_M(a_\star)/r_s(a_\star)$ .

Only with knowledge of the amount of expansion since last scattering (and the dilution rate of densities with redshift) can density ratios at last scattering be translated to late times.<sup>12</sup> For standard matter content, these density-ratio measurements set a baseline expectation for the MEDI [Eq. (2.2)] with  $\omega_m r_d^2$  determined by  $a_\star^3 \bar{\rho}_{cb}(a_\star) r_d^2 = a_\star^3 \bar{\rho}_r(a_\star) r_d^2 / x_{\text{eq}}$ . [We consider modifications to

<sup>10</sup> The analogous equation in Ref. [7], Eq. (2.7), omitted the subscript  $\star$  in the leading factor of  $a$ .

<sup>11</sup> The present-day radiation density proves most convenient simply because the present-day CMB temperature is measured and the total relativistic density at last scattering is quantified relative to the photon density. Written in terms of  $T_\star$  and  $T_0$ ,  $r_s(a) \propto H_{100} M_{\text{pl}} / T_0 T_\star \cdot \sqrt{\omega_\gamma / \omega_r}$ .

<sup>12</sup> Further converting ratios to absolute densities relies on the present energy density of CMB photons, i.e., the measured CMB temperature, and also the amount of additional density in relativistic species around last scattering (whether the prediction for Standard Model neutrinos, i.e.,  $N_{\text{eff}}$ , or otherwise) [7, 16]; as mentioned previously, calibrating these densities is not necessary to test CMB predictions against acoustic scale observations.

the standard  $(a/a_\star)^{-3}$  extrapolation in Sec. III B.] Allowing for an instantaneous change in the pre- and postdecoupling matter abundances ( $\omega_{cb}$  and  $\omega_m$ ), the prediction for the MEDI reduces to

$$\frac{\chi(a_d, a_m)}{r_d} = \sqrt{\frac{\omega_{cb}}{\omega_m}} (\sqrt{x_m + x_{\text{eq}}} - \sqrt{x_d + x_{\text{eq}}}) \sqrt{3R_\star} \ln \left[ \frac{\sqrt{R_\star} \sqrt{x_d + x_{\text{eq}}} + \sqrt{1 + R_\star x_d}}{1 + \sqrt{R_\star x_{\text{eq}}}} \right]^{-1}, \quad (3.4)$$

which depends on the temperature and densities at recombination only in the form of dimensionless parameters that are well constrained by independent information in the shape of the CMB spectra ( $R_\star$ ,  $x_{\text{eq}}$ , and  $x_d$ ). Therefore, adjusting the density in *any* single component of the standard cosmological model cannot alter the prediction Eq. (3.4) (or any acoustic scale observable) without modifying the fit to the CMB spectra. (All acoustic scale observables depend on predecoupling physics in this manner, not just the MEDI.) Otherwise, Eq. (3.4) only depends on  $x_m = a_m/a_\star$ , where  $a_m$  is determined, e.g., by the measured redshift of a galaxy sample (or whatever redshift a collection of BAO measurements best constrain), which is unrelated to recombination physics. We next discuss the implications of these insights for modified recombination and high-density recombination models.

### 1. High-temperature recombination, or low-temperature present

The most trivial means to alter the relationship between density ratios at recombination and at the present is to change how much expansion elapsed in between,  $a_0/a_\star = T_\star/T_0$ . Such a possibility either requires that the CMB temperature is mismeasured [29] or that nonstandard recombination physics modifies the temperature at last scattering  $T_\star$  [16, 28, 70–74]. Modifying the redshift of recombination is most effectively realized microphysically via a hyperlight scalar field that modulates the electron mass in time [16, 75], which leaves few to no signatures in the CMB anisotropies as generated at last scattering; introducing arbitrary additional freedom in the recombination history [72–74] does not appear to introduce any additional qualitative features. Varying the CMB temperature from its measured value also modifies  $a_\star$  without disrupting density ratios at decoupling and thus modifies acoustic scale observables in an identical manner.

Since  $\omega_{cb} r_d^2 \propto a_\star$  at fixed  $x_{\text{eq}}$  and  $R_\star$  (with no other parameter dependence), modified recombination changes the predicted MEDI relative to the drag horizon, as encoded by  $x_m = a_m/a_\star$  in Eq. (3.4). In  $\Lambda$ CDM, the reduction in  $\omega_m r_d^2$ , combined with the strongly correlated reduction in  $\Omega_m \propto (\omega_m r_d^2)^5$  at fixed  $\theta_s$ , fully mediates the tension between DESI and the CMB [7, 16]. More generally, early recombination (or “late present,” i.e., smaller  $T_0$ ) mediates the matter-era distance excess by reducing the sound horizon squared more so than it increases the matter density at any fixed redshift. From Eq. (3.4),  $\chi(a_d, a_m)/r_d \propto 1/\sqrt{a_\star}$ ; a reduction in  $a_\star$  by about a percent accommodates the half-percent increase in the MEDI preferred by DESI, with nonzero neutrino masses allowed via a further reduction by about  $1/\sqrt{1 + f_\nu}$  [7, 16].

More quantitatively, we may estimate the measurement of  $a_\star/a_0$  from the MEDI semianalytically by computing  $a_\star/a_{\star, \text{fid}} = \omega_{cb} r_d^2 / \omega_m r_d^2$ , with the denominator measured by the acoustic scale as in Fig. 2, the numerator taken from a CMB posterior, and  $a_{\star, \text{fid}}$  the scale factor of last scattering in standard cosmology. This quantity corresponds to the ratio of the electron mass at early and late times, if it evolves, or the inverse of the CMB temperature divided by its measured value, if supposed to be different. The result,  $1 + (0.88 \pm 0.52) \times 10^{-2}$ , closely matches that from a full fit to the CMB and DESI DR2 in the varying electron mass scenario,  $1 + (0.76 \pm 0.48) \times 10^{-2}$ . When additionally varying the neutrino mass sum (allowing any nonnegative value), the result shifts to  $1 + (1.1_{-0.54}^{+0.62}) \times 10^{-2}$ , while the 95th percentile of the marginal posterior over  $M_\nu$  is 160 meV (see Fig. 8), slightly tighter than the limit of 200 meV derived in Ref. [7] for *Planck* CMB data alone with DESI DR1.

## 2. High-density recombination

When the amount of expansion between last scattering and today is unchanged, and to the extent that the CMB measures the density in baryons and CDM relative to the total radiation density alone, a change in the calibrated, absolute density has no effect on acoustic scale observables. Namely, fixing  $x_{\text{eq}}$  requires that  $\omega_{cb}$  increases by exactly the amount  $r_d^2 \propto 1/\omega_r$  decreases. This feature is manifest in Eq. (3.4) in its lack of dependence on the total radiation density, reflecting that all acoustic scale observables (and CMB anisotropies) are dimensionless. The insensitivity of acoustic scale observables to the radiation density explains why BAO data contribute comparatively little to CMB constraints on the effective number of relativistic neutrinos  $N_{\text{eff}}$ .

Strictly speaking, however, the invariance of the primary CMB at fixed  $x_{\text{eq}}$  and  $R_\star$  only holds when additionally fixing the diffusion rate per  $e$ -fold [16, 76, 77] and the fraction of the total radiation density that is collisionless [77, 78] (which is respected by the high-redshift recombination models discussed in Sec. III A 1). [Equations (3.3) and (3.4) are correct nonetheless because they depend only on the cosmological background.] In practice, CMB preferences for  $\omega_{cb}$  are driven by a tradeoff between fixing  $x_{\text{eq}}$  and the fraction of pressure-supported matter  $f_b = \bar{\rho}_b(a_\star)/\bar{\rho}_{cb}(a_\star)$  [77], while its measurements of  $\omega_b$  compromise between fixing the acoustic peak structure ( $R_\star$ ) and the damping tail (unless introducing additional parameter freedom). Combined, the baryon density increases marginally with the radiation density, while the density in baryons and CDM combined increases sublinearly with the radiation density. Reference [77] shows that, when strictly adding radiation on top of the Standard Model prediction, the changes to inferred density ratios lead the CMB to predict smaller values of  $\omega_{cb}r_d^2$  that are more consistent with DESI’s BAO data (i.e., that alleviate the matter-era distance excess).

Moreover, the fraction of radiation that freely streams affects the propagation of acoustic waves, modulating their amplitude and phase [49, 50]. Figure 4 shows that current CMB data prefer values lower than the prediction of Standard Model neutrinos [79] (i.e., low- rather than high-density recombination), whose net impact is to exacerbate the matter-era distance excess. On the one hand, the reduced free-streaming fraction shifts the acoustic peaks to higher multipoles, which is compensated for by decreasing the distance to last scattering [and therefore also  $D_M(a_d)/r_d$ ]. [Since the phase shift affects the CMB’s inference of  $\theta_\perp(a_d)$ , we present both the MEDI and  $D_M(a_m)/r_d$  in Fig. 4, with the latter being the more relevant prediction from the CMB to compare with DESI data.] On its own, a reduced phase shift would then alleviate the matter-era distance tension; however, its effect is outweighed by the increase in  $\omega_{cb}r_d^2$ .

With the photon density (i.e., the density in collisional radiation) fixed, however, varying the free-streaming fraction via the number of effective degrees of freedom in radiation is quite limited by the correlated impact on diffusion damping. Extending the parameter freedom to include the helium yield from nucleosynthesis is a common choice to absorb some of the impact on diffusion. We find that the helium yield has little impact on acoustic scale predictions, while instead varying the fine-structure constant [16, 75, 80–82] (which also modulates the diffusion rate) has a more substantial effect. In fact, a time-varying fine-structure constant alone resolves the matter-era distance excess; Fig. 4 shows that current CMB data prefer a larger early-time value at the  $2\sigma$  level [79], which can be realized with a hyperlight scalar field [16, 75].<sup>13</sup> That said, the results in Fig. 4 take massless neutrinos and only just resolve the excess, so at best they modestly alleviate geometric limits on neutrino masses.

The extent to which the CMB permits different density ratios depends in general upon the

<sup>13</sup> We find that the fine-structure constant and helium yield are strongly degenerate in CMB predictions, simultaneously in their impact on diffusion and polarization [16], which in fact allows for a range of recombination redshifts nearly as wide as that from electron-mass variations. The degenerate combination, however, is not well aligned with the predicted variation of the helium yield with  $\alpha$  from nucleosynthesis calculations [75]. For this reason, and because it offers no relevant phenomenology not captured by a varying electron mass, we do not explore this scenario further, though it would be interesting to understand the physical mechanism for the degeneracy.

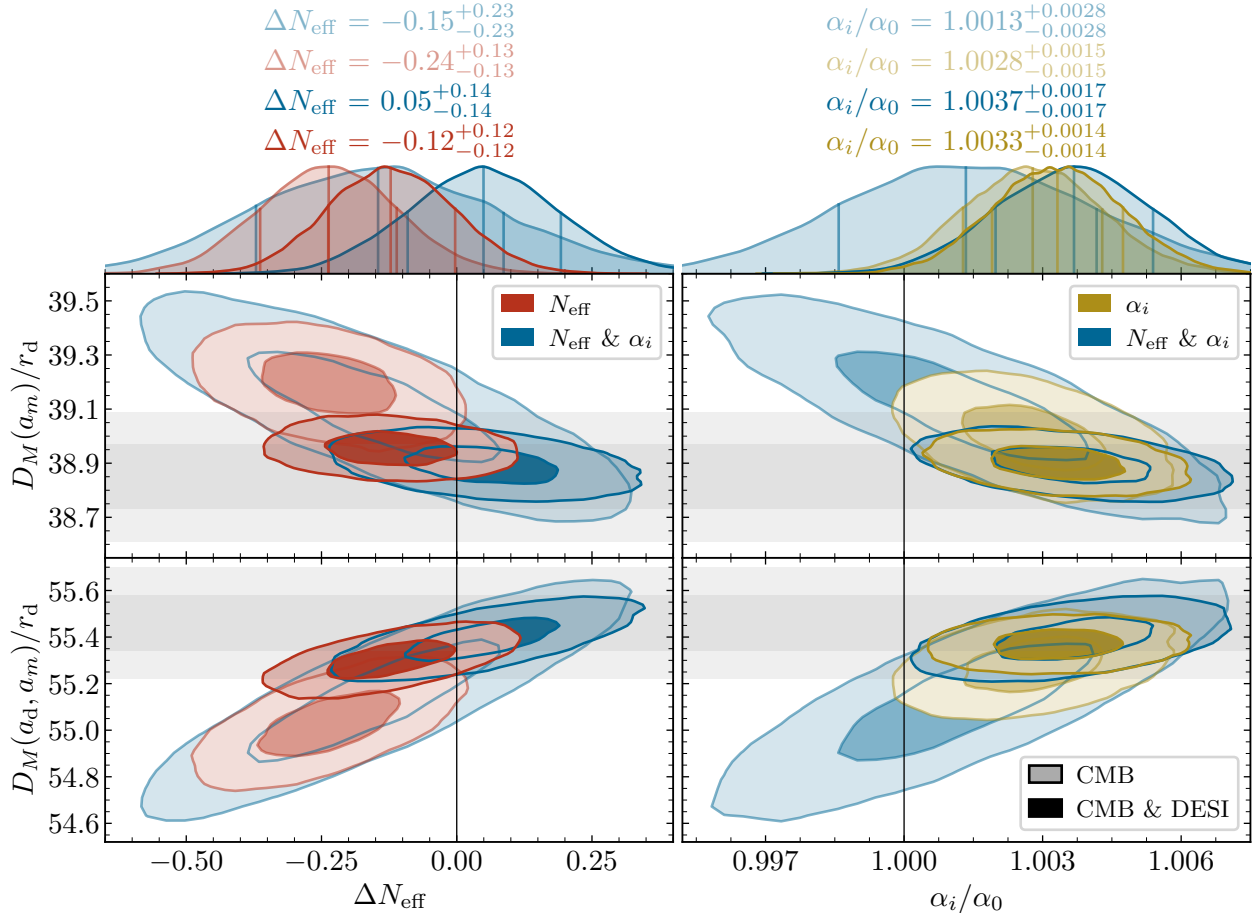


Figure 4. Concordance of CMB predictions and acoustic scale measurements in a selection of scenarios modifying physics before decoupling: varying the effective number of neutrino species  $N_{\text{eff}}$  (red), the early-time value of the fine-structure constant (gold), or both (blue). Middle and bottom panels display the joint posterior over each parameter and the “distance to matter domination”  $D_M(a_m)/r_d$  and the matter-era distance interval  $D_M(a_d, a_m)/r_d$ , respectively; up to the small effect of  $\Delta N_{\text{eff}}$  on the inferred  $D_M(a_d)/r_d$ , both rows contain the same information. Horizontal shaded regions depict the 1 and 2 $\sigma$  limits of acoustic scale measurements from Figs. 1 and 3. Current CMB data alone prefer  $N_{\text{eff}}$  below the Standard Model prediction, which exacerbates the matter-era distance tension, but prefer  $\alpha_i$  larger than the present-day value by  $\gtrsim 2\sigma$ , which alleviates the tension. Results fix the neutrino mass sum to zero to isolate early-time effects on extrapolated distances; since CMB predictions at best match acoustic scale measurements in each scenario, none can fully reconcile the matter-era distance excess for arbitrarily large  $M_\nu$ . Varying the helium yield to absorb the impact of  $\Delta N_{\text{eff}}$  on diffusion has no substantive impact on acoustic scale predictions.

detailed impact of new components on the evolution of the photon–baryon plasma. For instance, the impact of strongly interacting (as opposed to collisionless) dark radiation on CMB anisotropies is more effectively absorbed by shifts to  $\Lambda$ CDM parameters, permitting better compatibility with DESI BAO data [77]. Unlike free-streaming radiation (studied in Fig. 4), the decrease in  $\omega_{cb}r_d^2$  with increasing radiation density is accompanied by a decrease rather than an increase in  $D_M(a_d)/r_d$  (due to the phase shift as discussed above). For the same increase in radiation density, new fluidlike radiation therefore more greatly reduces the BAO–CMB tension than new free-streaming radiation.

While the analytic results above [Eqs. (3.3) and (3.4)] are only exact in standard cosmology (with arbitrary radiation density), other classes of high-density recombination are subject to similar considerations. For instance, CMB fits with early dark energy require  $\omega_c$  to increase with the EDE

fraction [33, 37, 83], which has been argued to preserve the early integrated Sachs–Wolfe feature on moderate angular scales [37, 83]; this suggests that the matter–radiation ratio at recombination (as encoded by  $x_{\text{eq}}$ ) generalizes to a matter–nonmatter ratio. References [84, 85] indeed showed that early dark energy cannot mediate the BAO–CMB tension, as the inference of  $\omega_{cb}r_d^2$  from the CMB is only marginally altered (see in particular Fig. 2 of Ref [85], which quoted only marginal improvements to  $2.3\sigma$  from  $2.8\sigma$  in  $\Lambda\text{CDM}$ ). Given the typically large sound speed of its fluid perturbations [37], early dark energy is likely more akin to free-streaming than fluidlike radiation.

We conclude by commenting on analyses of acoustic scale data that are agnostic to predecoupling physics. References [64, 86] attempt to derive constraints from acoustic scale data that are independent of recombination-era physics by treating  $r_d$  as a free parameter. These analyses, however, simultaneously impose a prior on the matter density inferred from the CMB in  $\Lambda\text{CDM}$  (or constrain it using other datasets modeled within  $\Lambda\text{CDM}$ ). This choice is unmotivated (given that the CMB measures ratios of densities, and a change to the absolute density at recombination, whether because it occurs earlier or with additional dark components, is required to change the drag horizon) and corresponds to no known model. A larger inferred CDM density, as generally encoded by the CMB’s requirement to fix  $x_{\text{eq}}$ , is well established in early recombination via varying constants [16, 28] and phenomenological modifications to the ionization history [72] as well as high-density recombination via extra radiation [76] or other dark components like early dark energy [33, 37, 83]. The analysis of Refs. [64, 86] is thus not meaningfully agnostic to recombination-era physics; fixing the matter density is especially problematic for the inference of neutrino masses in Ref. [86], given that the neutrino density is actually determined via the difference between the matter abundance long after decoupling (measured by the acoustic scale) and before decoupling (that in CDM and baryons inferred by the CMB). Reference [87] performed an analysis similar to Refs. [64, 86] but discarded the CMB’s information on  $\omega_{cb}$  entirely, which is more principled but gives up the ability to geometrically discern massive neutrinos’ contribution to  $\omega_m$ . The approach taken in Sec. III C 1 and Ref. [7], of simply parametrizing densities in units  $\propto 1/r_d^2$ , incurs no such inconsistencies and maintains maximal generality, beyond which one must specify (not ignore) the relationship between the drag scale and early-time densities and ratios thereof.

### 3. Optical depth, or the CMB lensing excess

We now discuss how the optical depth to reionization  $\tau_{\text{reio}}$ —that is, supposing its value is underestimated by large-scale CMB polarization data—alleviates the BAO–CMB tension, as noted in Refs. [38, 39]. We first explain the effective equivalence of the optical depth and a modulation of CMB lensing on small scales. Beyond dynamical effects around last scattering, the joint density in baryons and CDM determines the turnover scale in the transfer function,  $k_{\text{eq}} = a_{\text{eq}}H(a_{\text{eq}}) = \omega_{cb}/\sqrt{\omega_r/2} \cdot H_{100}$ . A higher CDM density (i.e.,  $x_{\text{eq}}$ ) can explain the preference for excess lensing of the CMB’s acoustic peaks [1–3, 88], though not without degrading the fit at large angular scales that are relatively unaffected by lensing. Namely, the more density in matter compared to radiation, the smaller the turnover scale and the larger amplitude of late-time structure at fixed wave number. This tension between low and high multipoles [89] can be mediated by enhanced structure growth after decoupling, as frequently tested via a phenomenological rescaling of the lensing amplitude  $A_L$  [90].

Given that the overall amplitude of the CMB anisotropy spectra at  $\ell \gg 30$  is suppressed by late-time reionization by a factor  $e^{-2\tau_{\text{reio}}}$ , the CMB lensing excess is equivalent to the preference for larger  $\tau_{\text{reio}}$  inferred indirectly from CMB lensing [1, 7] than that measured from features in polarization on large angular scales. That is, increasing the optical depth and the amplitude of the primordial power spectrum in tandem preserves the overall amplitude of the CMB while

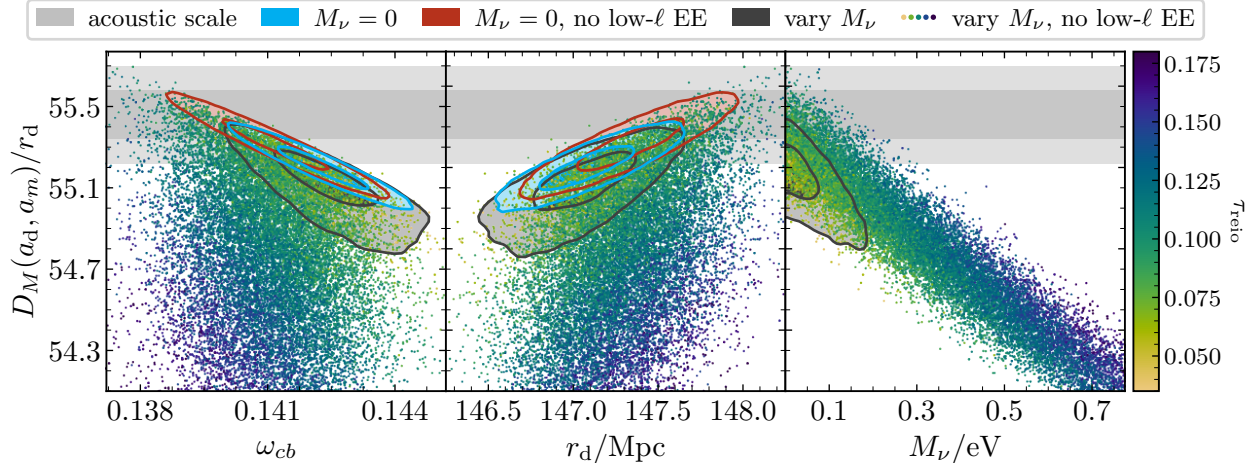


Figure 5. Posterior distribution over the matter-era distance interval and the density in baryons and CDM, the drag horizon, and the neutrino mass sum. Results that vary  $M_\nu$  and exclude low- $\ell$  polarization data are displayed as scatter colored by the optical depth, with the 1 and  $2\sigma$  mass levels thereof that include all CMB data appearing in black. The same mass levels of posteriors that fix  $M_\nu = 0$  and either exclude and include low- $\ell$  polarization data appear in red and blue, respectively. Horizontal shaded regions depict the 1 and  $2\sigma$  limits of the MEDI as measured by the acoustic scale (see Fig. 3).

enhancing the amplitude of large-scale structure itself. A higher lensing amplitude permits lower CDM densities that better fit the CMB on unlensed scales, i.e.,  $\ell \lesssim 1000$  or so. In  $\Lambda$ CDM, a decreased CDM density is compensated for by an increased dark energy density to fix  $\theta_s$ , resulting in the exacerbated decrease in the matter fraction  $\Omega_m$  correlated with  $\tau_{\text{reio}}$  that was noted in Ref. [38].

To explain the relevance to the BAO–CMB tension, Ref. [39] claimed that lensing contributes significantly to the CMB’s calibration of the sound horizon and that freeing the lensing amplitude (via the optical depth, for instance) therefore mediates tension by weakening constraints on  $r_d$ . However, neither the premise nor the conclusion is the case. First, removing lensing information has no appreciable effect on the uncertainty in  $r_d$ , which increases only from 0.17% to 0.19% by excluding CMB lensing reconstruction data and to 0.21% by additionally marginalizing over the amplitude of two-point lensing (via a phenomenological rescaling  $A_{\text{smear}}$ ). Second, the decrease in  $\omega_c$  with increasing  $A_L$  or  $\tau_{\text{reio}}$  increases the sound horizon  $\propto x_{\text{eq}}^{0.25} \propto \omega_c^{-0.21}$  at fixed  $R_\star$  (i.e., the Universe is larger at decoupling), which on its own decreases the CMB-calibrated MEDI in Fig. 3 (though only by a tenth of a percent) and exacerbates rather than alleviates the tension. As emphasized in Secs. II B 3 and III A 2 and Ref. [7], the sound horizon only determines the units with which densities are measured by the acoustic scale; a small rescaling of units cannot explain the sign of the matter-era distance tension (i.e., the matter density deficit). The salient effect of the lensing amplitude is the decrease in  $\omega_{cb}$  that overcompensates for the resulting increase in  $r_d^2$ , yielding a smaller  $\omega_{cb}r_d^2$  and larger MEDI.

Figure 5 demonstrates the positive correlation between the MEDI and the drag horizon calibrated by the CMB, despite the former’s inverse dependence on the latter, and a stronger anticorrelation with  $\omega_{cb}$ . The larger values of  $\tau_{\text{reio}}$  permitted by excluding *Planck*’s large-scale polarization data allow for lower  $\omega_{cb}$  and thus predict larger  $D_M(a_d, a_m)/r_d \propto 1/\sqrt{\omega_{cb}r_d}$ , despite the slight, correlated increase in  $r_d$ . This trend leaves room for slightly heavier neutrinos (whose increased suppression of structure is also accommodated by a yet-larger optical depth), but not enough to fully resolve the tension, as the CMB still underpredicts the MEDI even with massless neutrinos; see Fig. 8. Note that including low- $\ell$  polarization data but marginalizing over  $A_{\text{smear}}$  indeed yields nearly identical results, with  $\ln A_{\text{smear}}/2$  taking the place of  $\tau_{\text{reio}}$ .

## B. Postdecoupling physics

We now take the CMB's calibration of  $\omega_{cb}r_d^2$  for granted and consider physics after photon–baryon decoupling that modify the extrapolated matter-era distance interval. With spatial curvature an exception treated separately in Sec. III B 3, such scenarios may be studied via (presumably perturbatively small) modifications to the expansion history during the matter era. The variation of the comoving distance  $\delta\chi(a)$  with small relative variations in the energy density  $\delta\ln\bar{\rho}(\ln\tilde{a})$  about the density  $\bar{\rho}_{mr}$  in matter and radiation is

$$\frac{\delta\chi(a)}{\delta\ln\bar{\rho}(\ln\tilde{a})} = -\int_0^a \frac{d\ln a'}{a'H(a')} \frac{\delta\ln H(a')}{\delta\ln\bar{\rho}(\ln\tilde{a})} = -\frac{1}{2\tilde{a}H(\tilde{a})}. \quad (3.5)$$

We take  $\ln\tilde{a}$  as the coordinate to obtain the sensitivity coefficient per  $e$ -fold. Writing  $H_{mr}(a) = \sqrt{\bar{\rho}_{mr}(a)/3M_{\text{pl}}^2}$  and recalling Eq. (2.2), the sensitivity of the MEDI evaluates to

$$\frac{\delta\ln\chi(a_d, a_m)}{\delta\ln\bar{\rho}(\ln a)} \simeq -\frac{1}{2aH_{mr}(a)\chi_{mr}(a_d, a_m)} = -\frac{1}{4} \frac{a}{\sqrt{a+a_{\text{eq}}}} \frac{1}{\sqrt{a_m+a_{\text{eq}}} - \sqrt{a_d+a_{\text{eq}}}}. \quad (3.6)$$

In general, the MEDI's sensitivity (per  $e$ -fold) to small modifications to the energy budget scales with  $1/aH_{mr}(a) \propto \sqrt{a}$  (for  $a \gg a_{\text{eq}}$ ), i.e., earlier modifications are modestly suppressed relative to later ones (when the comoving horizon is larger). Integrating yields the leading-order correction to the matter–radiation result,

$$\chi(a_d, a_m) \simeq \chi_{mr}(a_d, a_m) - \int_{a_d}^{a_m} \frac{d\ln a}{2aH_{mr}(a)} \frac{\bar{\rho}(a) - \bar{\rho}_{mr}(a)}{\bar{\rho}_{mr}(a)}. \quad (3.7)$$

This correction is naturally just the perturbation to the energy density integrated over conformal time  $\tau = \int d\ln a/aH$ ; which integration variable is most convenient (scale factor, time, or conformal time) depends on the particular application, though distances are observed at known redshift.

In Fig. 6 we compare the sensitivity of the MEDI [Eq. (3.6)] to the variations in energy density of a variety of postdecoupling scenarios, similar to an analysis of the sound horizon and diffusion scale in Ref. [91]. Figure 6 depicts the relatively greater sensitivity of the MEDI to later eras when the Universe is largest; nearly 90% of the weight lies below redshift 100 and 50% below 10. On top of that, the various scenarios we consider exhibit greater deviations at lower redshifts (though in some cases controlled by a second model parameter), making their effects well approximated by their impact on an otherwise matter-dominated Universe.

In the remainder of this section, we study the impact of these models on the matter-era distance interval (with massive neutrinos discussed in Sec. II A 2 and hyperlight scalars in Appendix A 1 b) analytically and numerically. We calculate their effect on the MEDI analytically from Eq. (3.7) (with details relegated to Appendix A 1 and spatial curvature treated separately), derive constraints from measurements of the MEDI alone using the semianalytic procedure presented in Sec. II C 1, and compare those results to fully numerical posterior distributions. For the latter, we use DESI DR2 data and CMB priors on  $x_{\text{eq}}$  and  $R_\star$  for simplicity of illustration (though neglecting modifications to the growth of structure has a small or negligible effect for all cases except decaying dark matter). In constructing the CMB priors, we continue to exclude lensing reconstruction data (which, in the case of dark forces in Sec. III B 2, is for technical reasons discussed in Ref. [27]). In all cases, for analytic estimates we conservatively quantify the matter-era distance tension with minimum-mass neutrinos, i.e., we add a  $M_\nu = 60$  meV contribution [Eq. (2.6)] to the  $M_\nu = 0$  result in Fig. 3, yielding  $\Delta D_M(a_d, a_m)/r_d = 0.36 \pm 0.16$ . We also comment on geometric degeneracies with varying (rather than fixed) neutrino masses and what influence each extension has on the growth of structure and CMB lensing excess, with complete analyses of CMB and BAO data presented in Sec. III C.

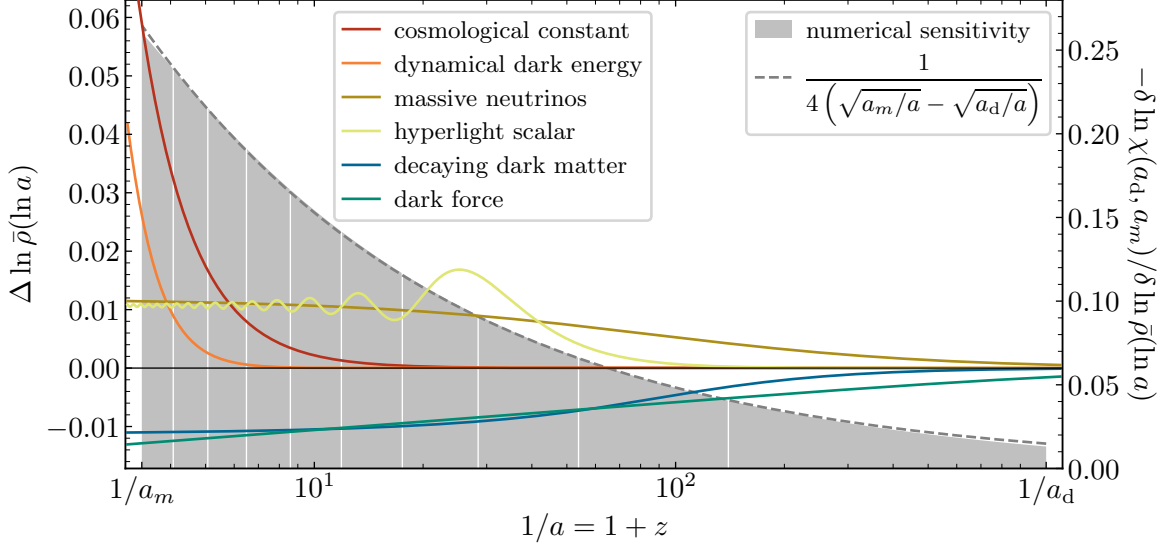


Figure 6. Sensitivity of the matter-era distance interval  $\chi(a_d, a_m)$  [with  $a_m = 1/(1 + 2.330)$ ] to modifications to the expansion history. The grey filled region depicts the sensitivity coefficient per  $e$ -fold to variations  $\delta \ln \bar{\rho}(\ln a)$  (right axis), divided into ten equal-weight intervals. The dashed grey line depicts an analytic approximation thereof [Eq. (3.6)]. Colored lines (left axis) display the relative change to the energy density  $\Delta \ln \bar{\rho}(\ln a)$  incurred by various extensions of or additions to a matter–radiation Universe, each discussed in detail in the main text. Parameters for all scenarios are chosen to match the fiducial 0.44% correction to the MEDI incurred by a cosmological constant ( $M_\nu = 157$  meV, 1.06% of dark matter in a hyperlight scalar, 1.33% of dark matter decaying, and a dark force strength  $2.94 \times 10^{-3}$  that of gravity), except for dynamical dark energy; in that case, parameters are chosen to be representative of preferences from contemporary data (see Sec. III D for discussion).

### 1. Decaying dark matter

A straightforward means to address the matter density deficit, and therefore the matter-era distance tension, is to deplete a subcomponent of dark matter via decays into, say, dark radiation on timescales long compared to the age of the Universe at decoupling but short compared to its present age [17–23]. Reference [22] explored how a compensatory decrease in the dark matter abundance, matching the late-time mass density in neutrinos and timed around their nonrelativistic transition, alleviates the incompatibility of BAO and CMB data with nonzero neutrino masses. Though the CMB’s preference for excess lensing curtails the model’s potential to alleviate the matter-era distance excess [22], we review this proposal as an application of the MEDI and our analytic methods.

Using the perturbative approach of Eq. (3.7), Appendix A 1 c analytically derives the impact of the decay of a dark matter subcomponent into dark radiation (accounting for the decay products and the noninstantaneous transition at leading order), which is well approximated by

$$\frac{\Delta \chi(a_d, a_m)}{1/H_{100}\sqrt{\omega_m}} \simeq f_{\text{ddm}}\sqrt{a_m} \left( 1 + \sqrt{\frac{a_{\text{dd}}}{a_m}} \left[ \frac{1}{10} \left( \frac{a_\times}{a_{\text{dd}}} \right)^2 - \sqrt{\frac{a_\times}{a_{\text{dd}}}} - \frac{\Gamma(5/3)}{\sqrt{a_\times/a_{\text{dd}}}} \right] + \Gamma(5/3) \frac{a_{\text{dd}}}{a_m} \right). \quad (3.8)$$

Here  $f_{\text{ddm}} = \lim_{a \rightarrow 0} \bar{\rho}_{\text{ddm}}(a)/\bar{\rho}_m(a)$  is the fraction of all matter (rather than dark matter, for simplicity) that decays and  $a_{\text{dd}}$  the scale factor of decay, defined as when the age of the Universe  $t(a_{\text{dd}}) \simeq 2a_{\text{dd}}^{3/2}/3\sqrt{\omega_m}H_{100}$  (in matter domination) matches the lifetime  $1/\Gamma_{\text{dd}}$ . Choosing  $a_\times = 1.12a_{\text{dd}}$  minimizes errors (see Appendix A 1 c for details). Finally, the fiducial value of the matter density  $\omega_m$  in Eq. (3.8) is set to the density in CDM and baryons inferred by the CMB, since the

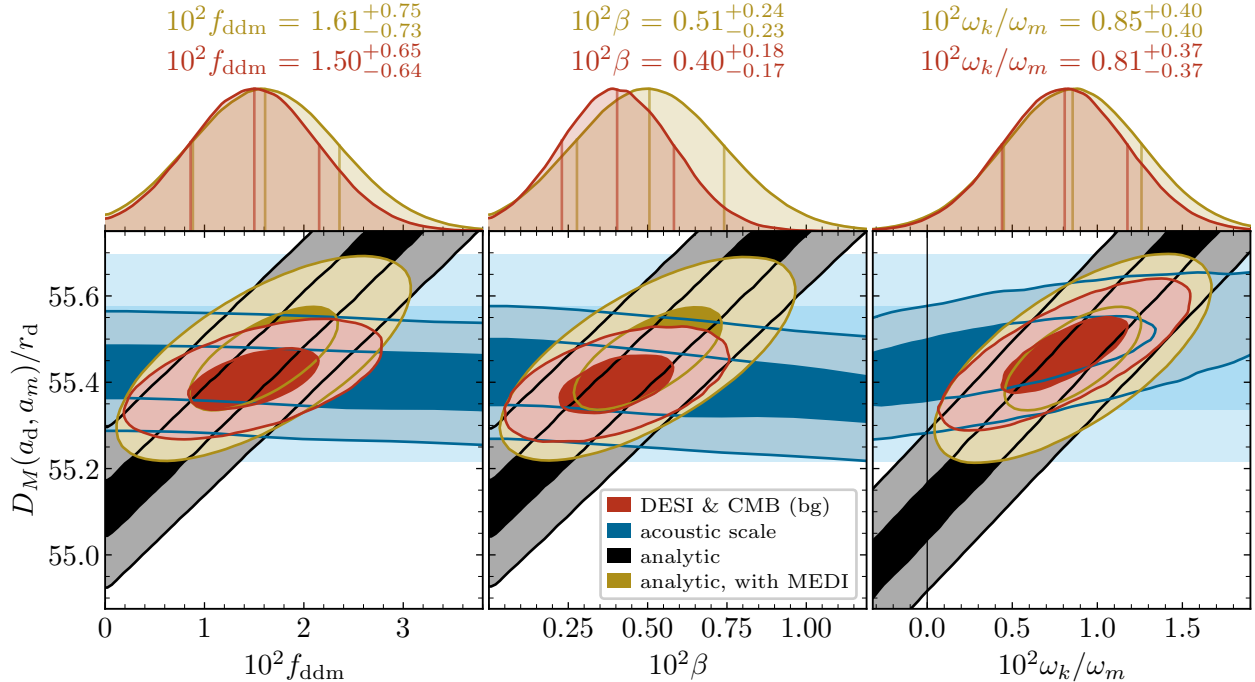


Figure 7. Acoustic scale constraints on postdecoupling modifications to the background cosmology from a fraction  $f_{\text{ddm}}$  of dark matter decaying at redshift  $\sim 150$  (left), a scalar-mediated long-range force acting on dark matter with strength  $\beta$  relative to gravity (middle), and nonzero curvature with density relative to that in matter  $\omega_k/\omega_m$  (right). Each panel depicts the distribution of the matter-era distance interval with each model’s new parameter, deriving from acoustic scale data from DESI DR2 and the CMB (blue) and combined with a CMB prior on the CDM and baryon densities at recombination (red), from this latter CMB prior combined with a weak one on  $a_{\text{eq}}$  and  $a_{m-\Lambda}$  (black, same as in Fig. 2), and from this prior combined with a fully marginalized measurement of the MEDI (gold); the latter two are derived with the analytic approximations from this section and the semianalytic procedure described in Sec. II C 1. The MEDI demonstrably contains most of the information for each extension parameter, with the discarded information being just its correlation with the MEDI measured by the acoustic scale (blue). Moreover, the  $> 2\sigma$  preference in each case derives from mediating the matter-era distance tension.

shape of the acoustic peaks is sensitive to the matter density before decoupling and therefore, for the parameters we consider, before decay.

For our fiducial  $a_m = 1/(1+2.330)$ , the sensitivity coefficient is  $\partial \ln \chi(a_d, a_m)/\partial \ln(1+f_{\text{ddm}}) \simeq 0.4$  for decay occurring at redshifts around 150, from which we estimate that the matter-era distance tension would be resolved by a fraction  $10^2 f_{\text{ddm}} = 1.6 \pm 0.7$  of dark matter decaying. This estimate agrees closely with the result derived from the semianalytic procedure outlined in Sec. II C 1, as depicted in Fig. 7. Moreover, Fig. 7 shows that the complete result (from all acoustic scale data and without analytic approximations) is only about 15% more precise and shifted by a bit more than a tenth of a standard uncertainty. The improvement derives from the correlation of the MEDI measured by the acoustic scale with  $f_{\text{ddm}}$ , which, since we impose a CMB prior on  $\omega_{\text{cb}} r_d^2$ , merely reflects its correlation with the late-time matter density  $\omega_m r_d^2$  evident in Fig. 2. Our simple approach of using the fully marginalized MEDI measurement in semianalytic results is conservative (e.g., with respect to possible dynamics of dark energy), though only intended for illustration.

The results in Fig. 7 neglect decaying dark matter’s effects on the growth of structure, which ultimately hinder its potential to alleviate neutrino mass limits [22, 23]. That said, our analytic results make the geometric degeneracy between the two transparent: the functional dependence of Eq. (3.8) on  $a_{\text{dd}}/a_m$  is identical to that of Eq. (2.6) on  $a_\nu/a_m$  for massive neutrinos, with numerical

coefficients differing by  $\sim 10\%$ . Prior work discussed how, when taking  $f_{\text{ddm}} = f_\nu$ , choosing  $\Gamma_{\text{dd}}$  to time decays at [22] or before [23]  $a_\nu$  largely cancels their effects on the expansion history; however, the cancellation cannot be made exact in  $\bar{\rho}(a)$  at all times, nor in distances out to epochs before their transitions (namely, the distance to last scattering). The analytic results Eqs. (2.6) and (3.8) enable a slightly different choice of  $a_{\text{dd}}$  in terms of  $a_\nu$  that cancels their most important observable effect (i.e., on the MEDI); however, without any direct probes of the expansion history so deep in the matter era, nor any subpercent measurement of the matter density at late times (independent of the MEDI), there is no particular need to fix  $f_{\text{ddm}} = f_\nu$  and match the MEDI by adjusting  $a_{\text{dd}}$  in this manner. Indeed, other observables like CMB lensing cannot be matched, even with a fixed expansion history: by reducing the density in clustering matter, the decay of dark matter suppresses perturbations in the density field  $\delta\rho$  by  $1 - f_{\text{ddm}}$ . Subsequently, the energy density in the decay products transiently suppresses the growth rate. The CMB lensing excess is therefore exacerbated in proportion to the degree to which decaying dark matter alleviates the matter-era distance excess.

## 2. Dark forces

The salient feature of decaying dark matter is not that the present-day matter density differs from that inferred from the primary CMB, but rather that the Universe dilutes faster on average during matter domination. The MEDI increases if dark matter redshifts faster than  $a^{-3}$  by whatever means—for instance, via the mass evolution characteristic of dark matter subject to a scalar-mediated long-range force [24–26]. This nontrivial background evolution is a main signature of such dark forces in linear cosmology, with the largest effect being the accumulated reduction in dark matter’s energy density as its mass decays with time [24, 27]. Given that the acoustic scale mostly measures the matter density via its integrated effect on the MEDI rather than its instantaneous value at late times, DESI’s sensitivity to dark matter’s modified rate of redshift in the last  $e$ -fold of expansion ( $z < z_m$ ) is far subdominant to the MEDI’s sensitivity to the preceding six  $e$ -folds. References [26, 27] indeed demonstrated a marginal preference for nonzero force strengths from CMB and DESI data; we now show that these results are reproduced by the MEDI alone.

Building on analytic results from Ref. [27] (leaving details to Appendix A 1 d), the sensitivity of the MEDI to a scalar-mediated force (whose range is not much smaller than the size of the Universe at  $a_m$ ) acting on a fraction  $f_\chi$  of all matter with strength  $\beta$  relative to gravity is approximately

$$\frac{\chi(a_d, a_m)}{\chi_{mr}(a_d, a_m)} - 1 \simeq \frac{\beta f_\chi^2 \sqrt{a_m} [\ln(a_m/4a_{\text{eq}}) - 4/3]}{2 \sqrt{a_m + a_{\text{eq}}} - \sqrt{a_d + a_{\text{eq}}}}. \quad (3.9)$$

The sensitivity coefficient for  $a_m = 1/(1 + 2.330)$  is  $\partial \ln \chi(a_d, a_m) / \partial \ln(1 + \beta f_\chi^2) \simeq 2.3$ . Since the dark matter mass begins evolving before decoupling (around equality), the appropriate choice of matter density in the fiducial MEDI  $\chi_{mr}(a_d, a_m)$  is less trivial than for decaying dark matter; Reference [27] showed that the CMB best measures the dark matter density around decoupling, corresponding roughly to  $\lim_{a \rightarrow 0} a^3 \bar{\rho}_\chi(a) (1 - \beta f_\chi^2)$ . To respect this distinction, when drawing values of  $\omega_{cb} r_d^2$  from a CMB prior for  $\Lambda$ CDM we set  $\omega_m r_d^2$  in  $\chi_{mr}(a_d, a_m)/r_d$  to  $\omega_{cb} r_d^2 / (1 - \beta f_\chi^2)$ , reducing the sensitivity coefficient of the MEDI to  $\beta f_\chi^2$  by one half.

With the force acting on all of dark matter ( $f_\chi \simeq 0.84$ ), we may estimate that the matter-era distance tension is resolved by a force strength  $10^2 \beta = 0.5 \pm 0.23$ , which again reproduces the result in Fig. 7 employing the semianalytic procedure from Sec. II C 1. Accounting for the correlation of the MEDI measured by the acoustic scale with  $\beta$  has a marginally more significant effect than for decaying dark matter (see Fig. 7), since the mass evolution impacts low-redshift distances less trivially than merely shifting the late-time matter density. These results also reproduce full parameter inference from Ref. [27], which obtained  $10^2 \beta = 0.3_{-0.15}^{+0.16}$  with  $M_\nu$  fixed to zero,

for which the tension is  $\Delta D_M(a_d, a_m)/r_d = 0.26 \pm 0.16$ ; our semianalytic result in this case is  $10^2\beta = 0.37 \pm 0.23$ , while the numerical result from the acoustic scale and the CMB prior is  $0.3^{+0.17}_{-0.16}$ .

The precise consistency of our results with those of Ref. [27], despite ignoring effects on perturbations, is no coincidence: the enhanced growth rate of dark matter overdensities due to the long-range force is precisely compensated by the faster decay of the background density, leaving all the gravitational effects of dark matter perturbations effectively unchanged [27]. Dark forces mediated by light scalars therefore have no impact on the CMB lensing excess, contradicting claims from Ref. [61], but rather only alleviate neutrino mass limits via background effects [27]. That said, dark forces are not subject to the same penalty as decaying dark matter from the CMB's preference for excess lensing. Reference [27] and Fig. 8 show that dark forces remove most of DESI's impact on neutrino mass limits, allowing mass sums nearly as large as allowed by the CMB alone.

### 3. Spatial curvature

The MEDI is the most sensitive geometric probe of spatial curvature. In a nonflat Universe where the transverse and comoving distances do not coincide, one may still compute the difference  $D_M(a_d, a_m) \equiv D_M(a_d) - D_M(a_m)$ —it just does not reduce to a single integral of  $1/aH$ . Curvature most affects the furthest distances, as  $D_M/\chi \approx 1 - (\chi/R_k)^2/6$  where again  $R_k^2 = -1/\omega_k H_{100}^2$  [92]. In particular, the distance to last scattering [and therefore the MEDI  $D_M(a_d, a_m)$ ] is parametrically more sensitive to curvature than low-redshift (nearby) distances, e.g., six times more so than DESI's furthest measurement (at  $z = 2.330$ ). The value of high-redshift BAO in mitigating the sensitivity of curvature measurements to dark energy was noted long ago [10]; the arguments of Sec. II A, particularly the improvement in  $D_M(a_m)/r_d$  from an ensemble of BAO measurements that is robust to dark energy dynamics, indicate that the MEDI represents the majority of the information even from all data. Reference [93] explained how curvature's impact on the distance to last scattering is preferred in combination with DESI and slightly alleviates the incompatibility with massive neutrinos; here we show that the matter-era distance excess underlies these results, and we augment their discussion of parameter degeneracies with an analytic derivation from the MEDI.

Curvature affects distances both in the comoving–transverse distance relation and in the Friedmann equation. To show that the former far dominates over the latter, we first note that, since  $\bar{\rho}_k \propto a^{-2}$ , the shift in the comoving MEDI is

$$\frac{\Delta\chi(a_d, a_m)}{1/H_{100}\sqrt{\omega_m}} \simeq -\frac{a_m^{3/2}\omega_k}{3\omega_m}. \quad (3.10)$$

Rewriting the total change, including the leading-order correction of  $D_M[\chi]$ , gives

$$\frac{D_M(a_d, a_m)}{\chi(a_d, a_m)} - 1 \simeq \frac{a_m\omega_k}{6\omega_m} \left( 4 \left[ \frac{\sqrt{\omega_m}\chi(a_d, a_m)}{2\sqrt{a_m}/H_{100}} \right]^2 \frac{\chi(a_d)^3 - \chi(a_m)^3}{[\chi(a_d) - \chi(a_m)]^3} - \left[ \frac{\sqrt{\omega_m}\chi(a_d, a_m)}{2\sqrt{a_m}/H_{100}} \right]^{-1} \right). \quad (3.11)$$

Since the quantity in parentheses multiplies the small parameter  $\omega_k/\omega_m$ , it may be approximated with fiducial values. Taking measured values from the acoustic scale of  $1/\theta_\perp(a_d) = 94.3$  and  $1/\theta_\perp(a_m) = 38.9$  [for our usual  $a_m = 1/(1 + 2.330)$ ], the difference of distances cubed divided by the cubed difference is about 4.6, while the combination  $\sqrt{\omega_m}H_{100}\chi(a_d, a_m)/2\sqrt{a_m}$  is about 0.93. Curvature's impact through the Friedmann equation is thus about 15 times less important than its effect on the transverse distance (i.e., at fixed  $\chi$ )—not surprising, given that a subpercent contribution to the total density today corresponds to a yet-smaller fractional contribution during matter domination that diminishes at higher redshift with  $1/(1 + z)$ .

The coefficient of  $\omega_k/\omega_m$  in Eq. (3.11) is about 0.75, so mediating the matter-era distance excess requires negative curvature (i.e., with positive density parameter). We estimate  $\omega_k/\omega_m = 0.87 \pm 0.39$ , which matches the semianalytic result in Fig. 7 precisely; the full, numerical result is hardly altered by including rather than marginalizing over the correlation between the MEDI and  $\omega_k$ . Taking  $\Omega_m \approx 0.295$  to convert the latter from  $\omega_k/\omega_m$  to  $\Omega_k$  yields  $10^3\Omega_k = 2.4 \pm 1.1$ , quite consistent with the full result from DESI and CMB data of  $2.3 \pm 1.1$  [6].

Our analytic results identify a degeneracy with neutrino masses that agrees with Ref. [93], who report its slope as  $\Delta f_\nu/\Delta\Omega_k = 3.5$ : from Eqs. (2.6) and (3.11), the sensitivity coefficients of the MEDI to  $f_\nu$  and  $\Omega_k$  are about  $-0.4$  (for a single massive eigenstate) and  $2.5$ , respectively, so we obtain a slope of  $2.5\Omega_k/0.4f_\nu \approx 3.3$  for  $M_\nu = 60$  meV and  $\Omega_k = 2.4 \times 10^{-3}$  as above. Separately, Ref. [61] claimed that curvature addresses the BAO–CMB tension by increasing the total density at decoupling, mimicking matter. As Eq. (3.11) shows, curvature’s contribution to the energy density is at all times entirely negligible relative to its impact on the conversion from comoving to transverse distance, and also has the opposite sign; its density at decoupling would not be relevant anyway compared to late times (see Fig. 6), and even if it were, the relative contribution from curvature is reduced by a factor of  $1 + z_d$  at decoupling compared to today, not enhanced as they write.

The preferred curvature fraction above reduces the amplitude of CMB lensing by just over a percent (about double its impact on the MEDI), which increases the CMB lensing excess by a small amount relative to the  $\gtrsim 3\%$  precision with which current data constrain phenomenological rescalings of the lensing amplitude. Curvature thus alleviates neutrino mass limits solely by mediating the matter-era distance excess, with a penalty from the lensing excess that increases as greater curvature is invoked to accommodate neutrinos heavier than 60 meV.

### C. Implications for neutrino masses

To further illustrate the importance of the matter-era distance excess for current cosmological inference, we quantify the degree to which some of the high-redshift solutions discussed in Secs. III A and III B relax neutrino mass limits. Section II A 2 establishes the primary role of the MEDI in geometric measurements of neutrino masses; with a new-physics explanation of the excess, neutrino masses are then constrained almost entirely by the amplitude of late-time structure, including whatever impact the invoked new physics has on structure growth. In this section, we derive neutrino mass constraints in these various extensions of the cosmological model and summarize discussion throughout Secs. III A and III B on their interplay.

Figure 8 displays posterior distributions over the neutrino mass sum derived from DESI DR2 BAO data combined with CMB temperature and polarization data and marginalized over the parameters of various high-redshift solutions to the matter-era distance excess. As anticipated from Sec. III A 1 and shown previously in Refs. [7, 16], high-redshift recombination via a time-varying electron mass is the most effective means to remove geometric information on neutrino masses. Dark forces are nearly as effective since, as shown in Ref. [27] and reviewed in Sec. III B 2, they have minimal direct impact on CMB lensing. These two scenarios remove nearly all of the penalty on neutrino masses from adding DESI data to CMB data. Decaying dark matter, on the other hand, exacerbates the lensing excess by reducing the density in clustering matter and suppressing the growth rate via its relativistic decay products (see Sec. III B 1 and Ref. [22]); spatial curvature suppresses the lensing amplitude to a slightly lesser extent (Sec. III B 3 and Ref. [93]). Decaying dark matter and curvature thus only marginally relax neutrino mass limits.

In all scenarios, but especially for high-redshift recombination and a dark force, dropping large-scale CMB polarization data (which measure the optical depth) further relaxes limits by allowing the primordial power spectrum to have a larger amplitude, enabling greater suppression of

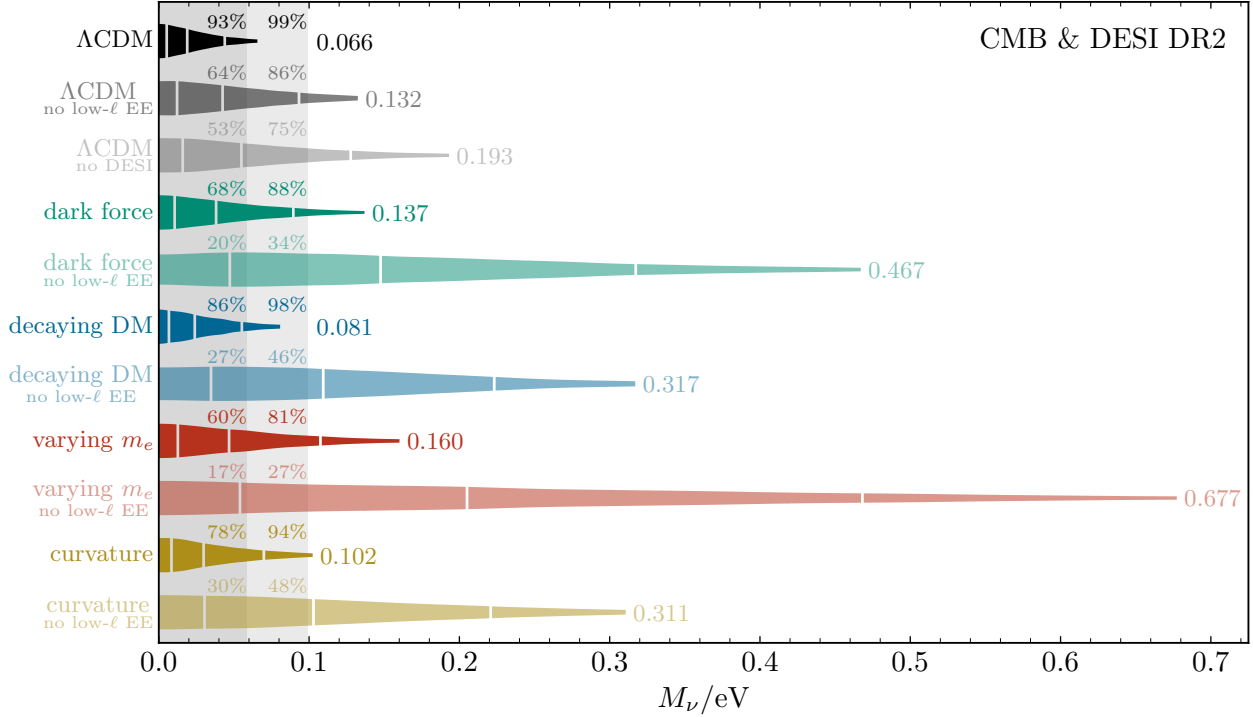


Figure 8. Impact of high-redshift solutions to the matter-era distance excess on neutrino mass limits from DESI DR2 and CMB temperature and polarization data, comparing dark forces (Sec. III B 2), decaying dark matter (Sec. III B 1), high-redshift recombination via a time-varying electron mass (Sec. III A 1), and spatial curvature (Sec. III B 3) to  $\Lambda$ CDM results. Each posterior is truncated at the 95th percentile (which is labeled), white lines mark the median and  $\pm 1\sigma$  quantiles, and the percent of the posterior that is incompatible with each mass hierarchy (vertical grey regions) is also labeled. Results either include (opaque) or omit (transparent) large-scale polarization data; the latter effectively removes the information on neutrino masses from the amplitude of structure. The  $\Lambda$ CDM result without large-scale polarization data illustrates the limited impact of optical depth measurements on the matter-era distance excess (Sec. III A 3) as, despite the simultaneous resolution of the CMB lensing excess, the 95th percentile relaxes only halfway to the result that excludes DESI data. Spatial curvature and (especially) decaying dark matter further suppress the lensing amplitude and therefore only have a marginal effect; a dark force and a time-varying electron mass, which have no direct impact on CMB lensing, are most successful in mediating the matter-era distance excess and alleviating neutrino mass limits. In these scenarios, upper limits are substantially increased by additionally omitting large-scale polarization data (which mitigates the impact of the CMB lensing excess).

structure by free-streaming neutrinos (and decaying dark matter or negative spatial curvature). The CMB lensing amplitude remains a point of tension in all models, underscoring the importance of robust measurements of the optical depth. Removing the optical depth constraint alone, despite its potential to not just allow for greater neutrino free-streaming but also partly mediate the matter-era distance excess (see Sec. III A 3), is less impactful than a varying electron mass and comparably so to a dark force.<sup>14</sup> This comparison suggests that solving the geometric (matter-era distance) tension alone more effectively addresses the neutrino mass tension than solving the lensing excess alone. Regardless, more complex reionization histories or large-scale primordial power spectra only achieve a small fraction of the requisite increase in the optical depth [39]; another possibility is birefringence induced by a hyperlight axion [94], though it has not yet been tested in a full parameter analysis.

<sup>14</sup> Our result excluding low- $\ell$  polarization data, which uses high- $\ell$  data from *Planck*, ACT, and SPT, is consistent with that using just *Planck* PR4 [38] or PR3 [39] and is slightly tighter than that from PR3 and DESI DR1 [7].

### D. High-redshift alternatives to dynamical dark energy

Current low-redshift distance measurements, which directly trace the late-time expansion history, do not provide compelling evidence for dynamical dark energy on their own [6, 95]. Conversely, the CMB is only weakly sensitive to the low-redshift expansion history and, insofar as dark energy is concerned, effectively provides nothing more than an integral constraint via the distance to last scattering. Yet the strongest evidence for dynamical dark energy emerges when combining distances with the CMB. However, Fig. 3 demonstrates that this improvement in joint fit cannot derive from dynamical dark energy’s impact on the *measured* matter-era distance interval—i.e., on  $D_M(a_m)/r_d$  inferred from DESI data alone.

In this section, we show that the joint evidence for dark energy dynamics in fact derives from its impact on distances at *high* redshift. That is, dynamical dark energy mediates the BAO–CMB tension specifically through the extrapolation of linear-in- $a$  approximations of the equation of state to high redshift, where a series expansion in small  $1 - a$  is least valid and the inferred “phantomlike” behavior most severe.<sup>15</sup> In turn, we show that any high-redshift solution to the matter-era distance excess, like those discussed in Sec. III, eliminates the CMB’s contribution to the preference for dynamical dark energy. We then identify the residual and more direct evidence for dark energy dynamics in DESI’s low-redshift distances—that is, the features a microphysical model would have to reproduce, on top of addressing the matter-era distance excess, in order to match the evidence attributed to the phenomenological model.

#### 1. Dynamical dark energy and the MEDI

We apply Eq. (3.7) to generalize the impact of a cosmological constant derived in Sec. II A 3 to dark energy with a varying equation of state. For tractability we assume radiation and dark energy are never simultaneously relevant. The correction is integrable for a constant equation of state  $w_{\text{DE}}$  at  $z > z_m$ , i.e.,  $\bar{\rho}_{\text{DE}}(a)/\bar{\rho}_m(a) = \bar{\rho}_{\text{DE}}(a_m)/\bar{\rho}_m(a_m) \cdot (a/a_m)^{-3w_{\text{DE}}}$ . In this limit,<sup>16</sup>

$$\frac{\chi(a_d, a_m)}{\chi_{mr}(a_d, a_m)} - 1 \simeq -\frac{\bar{\rho}_{\text{DE}}(a_m)/\bar{\rho}_m(a_m)}{14 - 12[1 + w_{\text{DE}}(a_m)]} \simeq -\frac{(a_m/a_{m-\text{DE}})^{-3w_{\text{DE}}}}{2 - 12w_{\text{DE}}}. \quad (3.12)$$

To make contact with the result for a cosmological constant [Eq. (2.10)], the second expression in Eq. (3.12) writes  $\bar{\rho}_{\text{DE}}(a)/\bar{\rho}_m(a) = (a/a_{m-\text{DE}})^{-3w_{\text{DE}}}$  where the matter and dark energy densities cross at  $a = a_{m-\text{DE}}$ .<sup>17</sup> Approximating the equation of state as constant with value  $w_{\text{DE}}(a_m)$  for  $z > z_m$  is more than sufficient to qualitatively understand the effect in the  $w_{\text{DE}}(a) = w_0 + (1 - a)w_a$  model, since the linearized equation of state has undergone 70% of its evolution toward its asymptotic value  $w_\infty = w_0 + w_a$  by  $z_m = 2.330$ . While Eq. (3.12) only captures the instantaneous rate of change in its density [ $w_{\text{DE}}(a_m)$ ] at the endpoint of the integral, its effect is generally largest at the latest times, particularly for fits to current data that extrapolate  $w_{\text{DE}}(a \ll 1) \ll -1$ .

For parameters preferred by current data, with  $w_\infty \ll -1$  but  $a_{m-\text{DE}}$  largely unchanged in fit compared to  $\Lambda$ CDM, Eq. (3.12) shows that the dominant impact of dynamical dark energy is to rapidly decrease its instantaneous contribution to the MEDI at  $a > a_m$  compared to a cosmological constant, as illustrated in Fig. 6. Namely, the extrapolation of the preferred phantomlike behavior both suppresses the numerator in Eq. (3.12) (i.e., the dark energy density decreases with redshift)

<sup>15</sup> Our analysis thus identifies the physical mechanism underlying the observation in Ref. [96] that the phantom transition is necessary to alleviate neutrino mass limits.

<sup>16</sup> In Eq. (3.12) we dropped the lower limit of the integral in Eq. (3.7), but the correction would be early-time dominated were  $w_{\text{DE}} > -1/6$  (and is logarithmically sensitive when the inequality is saturated). Excluding this possibility is a more restrictive condition than requiring that dark energy redshift more slowly than matter, but extrapolations of a linear-in- $a$  equation of state from current data strongly preclude such a regime.

<sup>17</sup> The equality scale factor  $a_{m-\text{DE}}$ , which is uniquely specified by the matter fraction  $\Omega_m$  in  $\Lambda$ CDM and measured by DESI to be  $0.751 \pm 0.010$ , is a more robust summary statistic than  $\Omega_m$  with dynamical dark energy, with  $a_{m-\text{DE}} = 0.748^{+0.016}_{-0.017}$ .

and enhances the denominator (i.e., its density decreases more rapidly with redshift). For instance, with  $w_{\text{DE}}(a_m) \approx -2$  inferred by DESI alone, the fiducial half-percent suppression of the MEDI by a cosmological constant is reduced by a factor of 30. Since the matter-era distance excess (for  $M_\nu = 60$  meV) is just over half a percent, dynamical dark energy thus resolves the BAO-CMB tension by eliminating its impact on distances during matter domination ( $z > z_m$ ).<sup>18</sup>

## 2. Reducible and irreducible evidence

To retain a Bayesian approach in quantifying preferences for new physics, we focus on posterior distances, i.e., what for sufficiently normal distributions would be the norm of parameter (vector) differences with the inverse covariance matrix serving as the metric. Since some posteriors are not well approximated as normal, we estimate the distance from a cosmological constant by computing the smallest mass level that encloses the point  $[w(z = 0.5), w_a] = [-1, 0]$  and converting it to the corresponding number of  $\sigma$ s for a two-dimensional normal distribution. DESI reports a number of frequentist statistics [6], which should be equivalent for sufficiently well-constrained posteriors [97], but are less straightforward to use for interpreting and disentangling preferences for dark energy dynamics and the high-redshift extensions we consider.

Second, we continue to fix a neutrino mass sum of 60 meV to be minimally compatible with neutrino oscillation constraints, and also to avoid the complication of CMB lensing’s independent disfavor of the suppression of structure from heavier neutrinos (i.e., marginalized over geometric effects [7]). There is nuance in generalizing fixed- $M_\nu$  results, in particular because the matter-era distance tension must ultimately be addressed in the context of an *a priori* unknown neutrino mass sum. For instance,  $M_\nu$  is conventionally restricted only to be nonnegative, so when most of the posterior mass is below 60 meV (as inferred by DESI and the CMB within  $\Lambda$ CDM), marginalizing over  $M_\nu$  reduces the apparent tension. Conversely, marginalizing over neutrino mass sums larger than 60 meV strengthens the matter-era distance tension.

Finally, to minimize computational cost and enable counterfactual tests (that artificially shift parameters preferred by the CMB), we employ CMB priors in place of likelihoods as in Sec. III B. We exclude lensing reconstruction, which would increase the joint preference to about  $3\sigma$ , for reasons discussed around Fig. 3. The considered extensions (including dynamical dark energy) again have a minimal impact on the integrated Sachs-Wolfe effect and CMB lensing, with the exception of decaying dark matter (see Ref. [23] for a dedicated analysis). Differences at the level of tenths of a standard deviation, whether from the choice of statistic, neutrino mass sum, or dataset, are unimportant for our purpose, which is to assess the differential impact of the matter-era distance excess and alternative explanations thereof on preferences for dark energy dynamics.

To test that the CMB’s added evidence for dark energy dynamics derives uniquely from its high-redshift resolution of the matter-era distance excess, Fig. 9 shows that combining DESI data with a CMB prior on either the CDM and baryon densities (which calibrates the CMB’s prediction for the MEDI) or  $1/\theta_\perp(a_d)$  (which provides the high-redshift anchor for the acoustic scale’s measurement of the MEDI) is insufficient to reproduce the preference. In fact, adding either the CMB’s geometric or nongeometric information only *reduces* the preference compared to DESI’s alone. Moreover, the added evidence also vanishes when shifting the central value of  $\theta_\perp(a_d)$  or the CDM density by the precise amount to remove the matter-era distance excess.

These tests establish the importance of dynamical dark energy’s high-redshift behavior and, moreover, that any other solution to the matter-era distance excess is a viable alternative explanation

<sup>18</sup> In fact, the suppression of the dark energy density is relevant at lower redshift, too: in the fits to current data, the equation of state crosses  $-1$  slightly before matter–dark-energy equality, increasing not only the “predicted” MEDI but also the “measured” distance to matter domination  $D_M(a_m)/r_d$  as evident in Fig. 1. Both effects alleviate the matter-era distance excess, though the latter is subdominant.

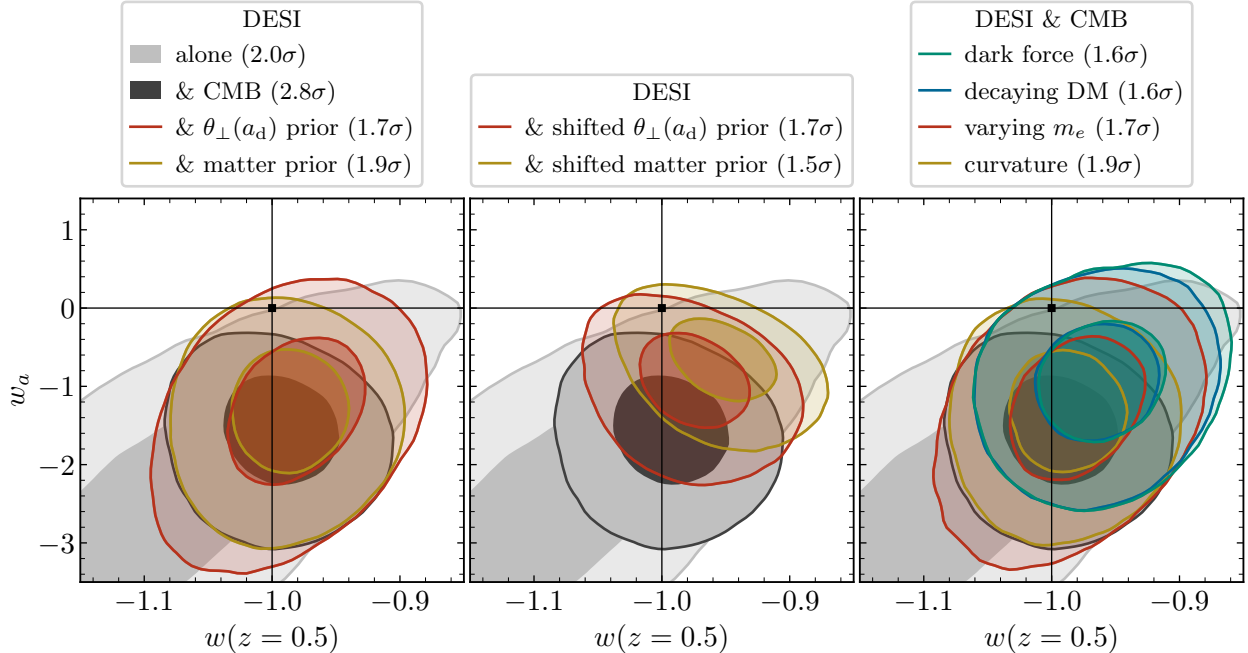


Figure 9. Impact of the matter-era distance excess (and alternative explanations thereof) on dynamical dark energy preferences from DESI DR2 and CMB data, presented as  $w_a$  and the equation of state at redshift 0.5 (close to the pivot redshift in all cases and much less correlated with  $w_a$  than  $w_0$  is) for visual clarity. Contours indicate 1 and  $2\sigma$  levels of the 2D distributions (i.e., the 39.3% and 86.5% mass levels thereof) to facilitate reading off posterior distances from  $w(a) = -1$  (which are also noted in the legends). Each panel shows standard results from DESI alone (light grey) and with a CMB prior (dark grey). Including a CMB prior with only geometric [ $\theta_{\perp}(a_d)$ , gold] or only nongeometric (baryon and CDM densities, red) information (left panel) is insufficient to realize the CMB’s added evidence; both are required to manifest the matter-era distance excess. Taking the full CMB prior but shifting the mean of either  $\theta_{\perp}(a_d)$  (gold) or the CDM density (red) to remove the matter-era distance excess (middle panel) eliminates the added preference from the CMB. Any of the high-redshift solutions presented in Sec. III (right panel) achieve a similar effect.

of the BAO–CMB tension. Figure 9 shows that a number of the models discussed in Secs. III A and III B indeed remove the CMB’s added evidence for dynamical dark energy by independently resolving the matter-era distance excess. Observe, for instance, that marginalizing over curvature has the same effect as removing the CMB’s geometric information, while modified recombination via a varying electron mass (which allows nearly arbitrary values of  $\omega_m r_d^2$ ) is tantamount to removing the CMB’s nongeometric information.<sup>19</sup> Decaying dark matter and dark forces achieve a similar effect, but only in the direction of decreasing  $\omega_m r_d^2$  and therefore increasing  $w_a$  closer to zero.

Though the evidence for dynamical dark energy deriving from the matter-era distance excess has quite a number of microphysically grounded alternatives (those discussed in Secs. III A and III B) that do not rely on the extrapolation of phenomenological models, the residual preference thereof is never much lower than that from DESI data alone. This irreducible evidence derives from DESI’s more direct constraints on the low-redshift expansion history as traced by its full set of observations at  $z < z_m$ . Figure 10 demonstrates that this evidence is most uniquely represented in the Alcock–Paczynski distortion  $D_M/D_H$ , a ratio which asymptotes to  $z$  for small redshift in all cosmologies. For further illustration, Fig. 11 displays the same analyses as Fig. 9 with the  $D_M/D_H$  information removed from the DESI likelihoods at redshifts 0.51 and 0.706. DESI’s independent

<sup>19</sup> Reference [65] previously proposed modified recombination as an alternative to dynamical dark energy, though they misattributed its effect to the change in  $r_d$  itself.

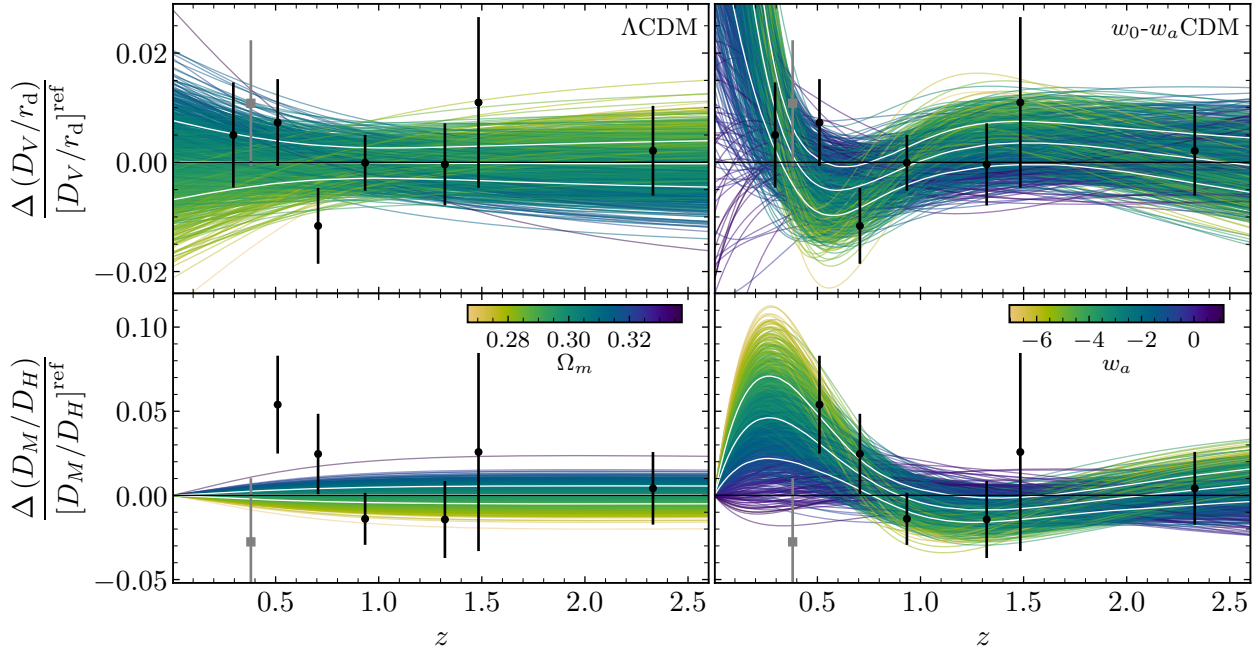


Figure 10. Features in DESI DR2 data that drive its preferences for dynamical dark energy over cosmological constant. Each panel depicts 1000 posterior samples from DESI alone for each model as residuals compared to DESI’s best-fit  $\Lambda$ CDM model, with DESI DR2 data superimposed in black; each curve is colored by its value of the present matter fraction  $\Omega_m$  for  $\Lambda$ CDM (left panels) or  $w_a$  for  $w_0$ - $w_a$ CDM (right panels). White lines depict the corresponding median and  $\pm 1\sigma$  quantiles. While  $\Lambda$ CDM provides a perfectly adequate fit to the isotropic BAO scale  $D_V/r_d \equiv 1/\theta_{\text{BAO}}$  [Eq. (2.11c), top panels], it has extremely little freedom to accommodate the variations in the Alcock–Paczynski distortion  $D_M/D_H$  (bottom panels), which varies with  $\Omega_m$  alone in  $\Lambda$ CDM and approaches  $z$  for small  $z$  in all cosmologies. In contrast, dynamical dark energy fits its low-redshift trend nearly perfectly with decreasing  $w_a$ . Since DESI DR2 does not supply a measurement of  $D_M/D_H$  from its lowest redshift sample, we display the lowest-redshift measurement from the Sloan Digital Sky Survey [63] in grey, as it opposes this trend.

preference for dynamics drops from  $2\sigma$  to  $1\sigma$ , while that of the DESI subset combined with CMB data (driven by the matter-era distance excess) persists at  $2.3\sigma$ . Just as in Fig. 9, the preference emerges only if sufficient CMB information is included to realize the matter-era distance excess; alternative explanations thereof reduce the joint evidence to as low as  $0.4\sigma$ .

Reproducing the sharp feature at low redshift in DESI’s data requires a rather extreme change to the expansion history at very late times—one that  $\Lambda$ CDM cannot accommodate. That this feature is fit so well by a phenomenological model like  $w_0$ - $w_a$  (with no theoretical prior to regulate its predictions) might suggest that it is relatively susceptible to low-redshift (high-leverage) statistical fluctuations. The tests shown in Fig. 11 do not call these data into question, but merely identify the observations most responsible for the dynamical dark energy preference. Indeed, were the physical behavior of the dynamical dark energy fit realized in a microphysical model at both low and high redshift, the feature in  $D_M/D_H$  and the matter-era distance excess could be taken as consilient evidence. While DESI DR2 does not derive a measurement of  $D_M/D_H$  from its lowest redshift sample, the lowest-redshift measurement from the Sloan Digital Sky Survey [63] opposes the trend in the  $w_0$ - $w_a$  fit to DESI; future anisotropic measurements at low redshift, from both DESI and other surveys with different sky coverage, may therefore be decisive in differentiating dynamical dark energy from solutions to the matter-era distance excess alone.

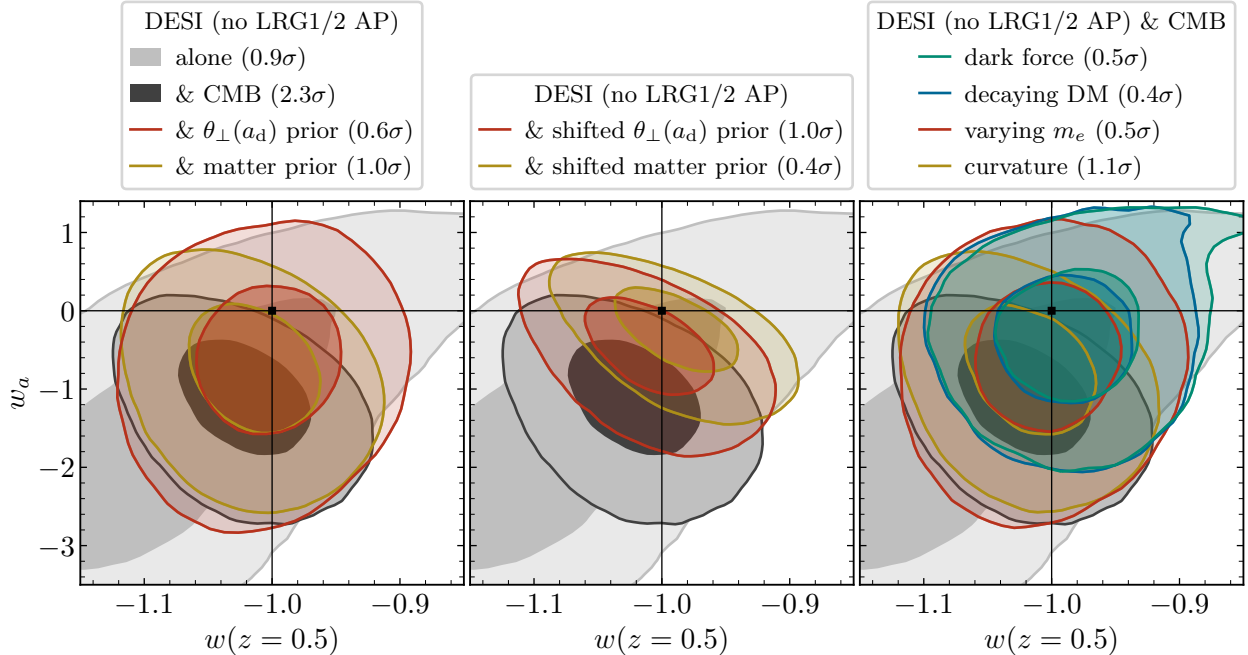


Figure 11. Same as Fig. 9, but taking DESI’s measurements of  $D_V$  alone for its  $z = 0.51$  and  $0.706$  bins (i.e., marginalizing the respective likelihoods over  $D_M/D_H$ ). With this subset of DESI data, solutions to the matter-era distance excess reduce the joint preference for dynamical dark energy to the  $0.5\sigma$  level.

#### IV. SUMMARY AND CONCLUSIONS

Recent observations position the acoustic scale as a precise and robust observable for constraining the expansion history, with future surveys promising multifold improvements, especially at high redshift. In this work, we developed an analytic description of high-redshift distances that cleanly compartmentalizes the acoustic scale’s sensitivity to the dark-energy- and matter-dominated eras. We conclude by summarizing the matter-era distance interval and its implications for the BAO–CMB tension, neutrino masses, dynamical dark energy, and tests of the cosmological model going forward.

##### A. The matter-era distance interval

The CMB’s acoustic scale information in the angular extent of the sound horizon is the second best-measured number in cosmology (after the present-day CMB temperature), providing the most precise and robust constraint on the integrated evolution of the dark energy density. Any cosmological model that expands the freedom of this quantity must therefore contend with parameter degeneracies with dark energy. With low-redshift acoustic scale measurements reaching subpercent precision, however, current data stand to simultaneously constrain both dark energy and a broad range of new physics at higher redshift.

In Sec. II A, we showed how combining acoustic scale measurements from low-redshift surveys and from the CMB cancels off a nearly optimal amount of their sensitivity to dark energy (even if just a cosmological constant). The difference in distances (measured relative to the sound horizon) to photon–baryon decoupling as constrained by the CMB and to the highest redshift accessible to large-scale structure surveys—the “matter-era distance interval”—represents the vast majority of the information on the interim expansion history. While DESI’s Lyman- $\alpha$  forest sample, with effective redshift 2.330, enables a direct and model-independent measurement of the distance to

matter domination (per se), Sec. **IIB** showed that all of DESI’s BAO data combine to measure the distance to  $z = 2.330$  with more than quadruple the precision; this result, moreover, is largely robust to dark energy dynamics. The MEDI derived in this manner therefore represents not just a critical component of the information in acoustic scale data but also a constraint on high-redshift dynamics that is agnostic to low-redshift dynamics.

As a first application, Sec. **IIC1** demonstrated that the MEDI represents the key contribution of the CMB’s geometric information to measurements of the late-time matter density from the acoustic scale. Without it, DESI presently constrains  $\omega_m r_d^2$  (i.e., the matter density in acoustic scale units) with 1.7% precision. Even marginalizing over DESI’s constraint on the matter density at  $z < 2.330$ , the MEDI alone measures the matter density (say, between  $z = 2.330$  and decoupling) with nearly four times the precision. The combined measurement (i.e., taking the same matter abundance at all epochs) is just 1.5 times more precise than the latter, deriving from the modest correlation of the jointly inferred distance to  $z = 2.330$  with the late-time matter density.

As a corollary, the MEDI generalizes arguments of Ref. [7] on how cosmological distances measure (or constrain) neutrino masses in  $\Lambda$ CDM; moreover, it represents the *direct* measurement of neutrino masses from the expansion history. That is, attributing to massive neutrinos any reduction in the measured MEDI is no less “direct” than is attributing any reduction in the measured amplitude of late-time structure. In both cases, the measurement is made relative to the CMB’s massless-neutrino prediction extrapolated from the conditions (the density and spatial distribution of matter) it infers at last scattering, when neutrinos are relativistic. And in both cases observations exhibit an excess where there should be a deficit.

The results in Sec. **II** are general to physics before decoupling and show that the parameter combination that encodes the MEDI’s early-time dependence is  $\omega_{cb} r_d^2$ , the density of baryons and CDM in acoustic scale units, not the density or drag horizon themselves. Section **IIIA** explains how the MEDI predicted by the CMB depends on density ratios at last scattering, with Eq. (3.4) applicable in any cosmology whose early-time expansion history is well described by radiation and matter. We then reviewed how high-redshift recombination modulates the extrapolation of density ratios from last scattering to late times (and thus modifies the MEDI), with little impact on primary CMB anisotropies; high-density recombination, on the other hand, largely affects the MEDI only via small shifts in inferred early-time density ratios and is therefore more limited by CMB constraints.

By sequestering the dominant effects of dark energy, the MEDI depends on high-redshift physics in a manner that is not only physically transparent but also analytically tractable. Indeed, we derived accurate analytic approximations for a variety of high-redshift effects beyond  $\Lambda$ CDM, including the effects of massive neutrinos (and their noninstantaneous nonrelativistic transition), modified dynamics of dark matter (nontrivial redshifting or subcomponents that decay or emerge after decoupling), spatial curvature, and the small impact of (possibly dynamical) dark energy at high redshift. Using these analytic results, in Sec. **IIIB** we showed that MEDI measurements robustly approximate constraints deriving from the full set of acoustic scale observations.

## B. Acoustic scale tensions

The MEDI provides a unified description of the growing tension between CMB and low-redshift BAO observations, as explained in Sec. **IIC**. In models whose postdecoupling expansion history is well described by  $\Lambda$ CDM, the tension reduces to a late-time matter density deficit, which has been identified as the origin of the geometric incompatibility of CMB and BAO data with massive neutrinos [7, 22]. Namely, the aforementioned measurement of the matter density from the acoustic scale is more than  $2\sigma$  below the CMB’s preferred matter density (including neutrinos with the minimum mass sum allowed by neutrino oscillations). However, there is no evidence of a matter

density deficit strictly at the redshifts DESI itself observes ( $z \leq 2.330$ )—its data alone are compatible with substantially larger matter densities. By showing that the MEDI contains the vast majority of the acoustic scale’s information on the matter density, Sec. II C 1 demonstrated that the matter-era distance excess underlies the matter density deficit (rather than vice versa). This analysis thus identifies the true tension as one at higher redshift: the acoustic scale (from DESI and the CMB) measures (i.e., with reasonable robustness to the cosmological model) a matter-era distance interval more than  $2\sigma$  larger than that predicted by the CMB—that is, based on its geometry-independent, early-time information on the density in CDM and baryons. When marginalizing over neutrino masses compatible with neutrino oscillation data [44, 45], the matter-era distance tension is  $2.6\sigma$ .

While  $\Lambda$ CDM fits both DESI and CMB data well individually, the matter-era distance excess represents the coarse-graining of the physics between decoupling and late times that prevents their reconciliation. The physical insight afforded by the MEDI facilitates a broad and analytically grounded assessment of potential solutions to the BAO–CMB tension (and identifies deficiencies in prior interpretations of the tension and its implications). Section III explained how the MEDI underpins the mechanism by which previous specific proposals address the tension, including early recombination [16], dark forces [26, 27], decaying dark matter [22], and spatial curvature [93]. In Sec. III A we also explored the (rather limited, except for high-redshift recombination) extent to which predecoupling physics mediates the matter-era distance tension.

Section III A 3 also identified the physical mechanism by which freeing the optical depth to reionization (i.e., from its measurements with large-scale polarization) alleviates the BAO–CMB tension [7, 38, 39], though only by about  $0.6\sigma$  when the neutrino mass sum is fixed to zero; the MEDI thus remains poorly fit. Excluding low- $\ell$  polarization data is far more effective at resolving the CMB lensing excess, thereby removing the lensing-amplitude constraint on neutrino masses. Though doing so reduces the matter-era distance excess to below  $2\sigma$  when fixing  $M_\nu = 60$  meV, it also makes the CMB compatible with substantially heavier neutrinos, for which the MEDI is underpredicted by an even greater absolute amount (but with a marginally decreased significance of  $2.3\sigma$ ). Figure 8 in Sec. III C shows that neutrino masses are more strongly penalized by the matter-era distance excess when the lensing excess is resolved (by freeing the optical depth) than vice versa. Moreover, without low- $\ell$  polarization data, solutions to the matter-era distance excess dramatically alleviate neutrino mass limits, reinforcing that the optical depth is of subdominant importance to the geometric tension. Nevertheless, a robust measurement of the optical depth, insofar as it informs the neutrino mass sum allowed by CMB lensing, is vital to quantifying the matter-era distance excess.

Beyond new physics at high redshift, an analytic understanding of the tension motivates counterfactual tests to identify the causal relationship between observations and parameter constraints. For instance, merely shifting the CMB’s acoustic scale measurement removes the tension (though we are unaware of any mechanism to realize the requisite  $\sim 10\sigma$  shift). Likewise, increasing just the longitudinal distance measurement from DESI’s Lyman- $\alpha$  sample by  $\sim 2\sigma$  could possibly achieve the requisite shift in  $D_M(a_m)/r_d$ ; however, in  $\Lambda$ CDM the measurement of  $D_M(a_m)/r_d$  is not shifted even by excluding Lyman- $\alpha$  entirely.<sup>20</sup> Were the longitudinal Lyman- $\alpha$  measurement not so consistent with the  $\Lambda$ CDM result calibrated by all other tracers, it would supply more evidence for dynamical dark energy (as evident in Fig. 1) and significantly alter the joint constraint on  $D_M(a_m)/r_d$ . This measurement likely has the most leverage among DESI’s data, since it informs the density between redshifts  $\sim 1.5$  and  $2.330$  that determines how much comoving distance accumulates beyond that measured by lower-redshift tracers. The BAO shift due to nonlinear corrections [98–100], which is not currently included in DESI’s analysis of the Lyman- $\alpha$  forest [51], could be a relevant systematic, though it is not expected to be large enough to appreciably affect the matter-era distance excess.

<sup>20</sup> We also checked that MEDI measurements are robust to leaving out any one of DESI’s other tracers, a finding congruent with the insensitivity of  $D_M(a_m)/r_d$  to dark energy dynamics.

### C. Implications for dark energy

The matter-era distance excess underlies the implications of the BAO–CMB tension for not just neutrino masses (and other high-redshift physics) but also dynamical dark energy, putting the two on common physical footing and clarifying their relationship. Contrary to what one might expect, dark energy dynamics do not address the excess by shifting DESI’s jointly inferred distance to matter domination  $D_M(a_m)/r_d$  (see Fig. 1) but rather by evacuating dark energy at high redshift. In the phenomenological  $w_0$ – $w_a$  model, current data prefer the dark energy density to increase as the Universe expands at high redshift: by reaching a significantly lower density at  $a < a_m$ , these dynamics eliminate the half-percent suppression of the MEDI from a cosmological constant (see Fig. 6), nearly enough to resolve the matter-era distance excess. Our analytic description in Sec. III D 1 pinpoints this solution’s reliance on the extrapolated and most physically implausible features of the canonical models of the dark-energy equation of state, i.e., a leading-order Taylor expansion in  $1 - a$ . This resolution to the excess is therefore not strictly guaranteed in any dark energy model that resembles the phenomenological fit at low redshift.

As a corollary, the alleviation of the neutrino mass tension in dynamical dark energy scenarios [6, 8] should also not be taken for granted. Our findings—namely, the negligible impact on the inferred distance to matter domination—refute the presumption that dark energy dynamics relax neutrino mass limits strictly through low-redshift effects. The key role of dark energy’s high-redshift behavior in modulating neutrino mass inference calls for more careful scrutiny of their interplay in microphysical models of dark energy; it also suggests that cosmological measurements of neutrino masses may be more robust to dark energy than phenomenological analyses imply.

The quantitative and counterfactual tests in Sec. III D 2 confirm that the CMB’s role in the preference for dynamical dark energy is to introduce the matter-era distance excess, contrary to the claims in Ref. [6] that its role is to measure the present-day matter density or matter fraction (neither of which the CMB directly measures with relevant precision). Rather, the CMB calibrates the *early*-time densities in CDM and baryons and therefore a baseline prediction of the distance photons traverse in matter domination (see Sec. II C). The CMB itself allows for the late-time matter abundance to vary much more broadly, should it be increased by massive neutrinos (Sec. II A 2) or hyperlight scalars (Appendix A 1 b) or decreased by a subcomponent decaying (Sec. III B 1) or by a scalar-mediated dark force (Sec. III B 2); the present-day matter fraction varies even more widely if dark energy evolves. The importance of the matter-era distance interval also underscores the danger in conflating the matter fraction  $\Omega_m$  and the matter density  $\omega_m \equiv \Omega_m h^2$ : since the densities of each matter component are conventionally independent parameters, the matter fraction in reality parametrizes *dark energy*. These distinctions are key to identifying alternative explanations of the data, and Fig. 9 shows that indeed any alternative explanation of the matter-era distance excess removes the CMB’s added evidence for dark energy dynamics: both in general and in specific models, removing the matter-era distance excess reduces the preference to below the  $1.7\sigma$  level.

The irreducible preference for dark energy dynamics from DESI is driven by features at low redshift that could plausibly be interpreted as sample variance that is overfit by the relatively arbitrary low-redshift dynamics allowed by the  $w_0$ – $w_a$  model (see Fig. 10). (We do not explore the role of supernova distances, partly to limit scope and partly due to the incoherent implications of current datasets and their sensitivity to revised calibration [95, 101], which largely removed their contribution to the evidence.) The physical effects that yield evidence for phenomenological models must also be contextualized in their underlying microphysical implementations. Given that this model only otherwise improves the joint BAO–CMB fit through its extrapolated and nominally unphysical dynamics at high redshift, this irreducible evidence must be weighed against microphysically grounded, alternative explanations of the matter-era distance excess. That said, a microphysical model that simultaneously explains both the low-redshift Alcock–Paczynski distortion

feature and the matter-era distance tension would be favored over the high-redshift scenarios discussed in Sec. III that explain only the latter. The most important theoretical input needed from fundamental models of dynamical dark energy is therefore not how their low-redshift behavior maps into the  $w_0$ – $w_a$  parameter space but rather whether they can simultaneously explain this low-redshift feature and the matter-era distance excess.

#### D. Outlook

The matter-era distance interval highlights the key role played by high-redshift distance measurements in constraining cosmology. Moreover, the current matter-era distance tension underscores the need to study extensions to the cosmological model in tandem with neutrino masses, in particular models for which low-redshift distances are informative. Fortunately, the MEDI is analytically tractable and supports a physically transparent interpretation of current data and their potential implications for the cosmological model. Robust explanatory power derives from an analytic (or at least semianalytic) understanding of the full physics of the problem to inform the interpretation of high-dimensional likelihoods over parameters, the combination thereof from multiple observations, and their posterior marginalization.

In the near term, the matter-era distance excess represents a focal point for future updates from DESI. Stratifying DESI’s high-redshift tracers into multiple bins, or incorporating new tracers at  $z \sim 2$  [102], could also be valuable in testing the jointly inferred distance to matter domination. Alternatively calibrated distances, like those from supernovae, could also be incorporated to at least further constrain the relative evolution of distances with redshift. Naturally, acoustic scale measurements from the rest of the sky would provide independent measurements of the distance to matter domination, though they would be perhaps more valuable in testing whether the low-redshift evidence for dynamical dark energy (Fig. 10) is simply sample variance. The MEDI also identifies unique physics opportunities in the high-redshift BAO observations that would be possible with extensions to DESI and stage-5 spectroscopic surveys [103–106]. BAO distances at yet-higher redshift could provide multiple measurements of the matter-era distance interval that better disentangle the dwindling influence of dark energy on distances, enabling robust measurements of neutrino masses or other early-Universe physics with nontrivial redshift dependence. It would also be valuable to pursue geometric neutrino mass measurements that are completely independent of dark energy.

Despite its critical importance in constraining cosmological parameters, the matter-era distance interval lacks discriminatory power: a single number is insufficient to differentiate multiple effects on the high-redshift expansion history. While future surveys may measure multiple intervals, the growth of structure remains (as always) an independent probe. Of course, many models in the class we considered in this work have largely scale-independent effects on observable scales. Decisive evidence for physics beyond  $\Lambda$ CDM—in tandem with a neutrino mass measurement—may ultimately only be possible for those most predictive models whose signatures in large-scale structure are strongly correlated with their effects on the expansion history.

#### ACKNOWLEDGMENTS

We thank Simone Ferraro, Lloyd Knox, Marilena Loverde, Gabe Lynch, Noah Sailer, Murali Saravanan, Kendrick Smith, Martin White, and Matias Zaldarriaga for discussions and feedback. Research at Perimeter Institute is supported in part by the Government of Canada through the Department of Innovation, Science and Economic Development and by the Province of Ontario through the Ministry of Colleges and Universities. This work made use of a number of open-source software packages [107–119].

## Appendix A: Calculational details

### 1. Analytic results

In this appendix we outline the approximations made in deriving the analytic results quoted in Secs. [II C](#) and [III B](#). In all cases, small perturbations to the matter-era distance interval are calculated from Eq. [\(3.7\)](#) as

$$\Delta\chi(a_d, a_m) \equiv \chi(a_d, a_m) - \chi_{mr}(a_d, a_m) \simeq -\frac{1}{2} \int_{\tau(a_d)}^{\tau(a_m)} d\tau \frac{\bar{\rho} - \bar{\rho}_{mr}}{\bar{\rho}_{mr}} \quad (\text{A1})$$

$$\simeq -\frac{1}{2H_{100}\sqrt{\omega_{cb}}} \int_{a_d}^{a_m} \frac{da}{\sqrt{a + a_{\text{eq}}}} \frac{\bar{\rho} - \bar{\rho}_{mr}}{\bar{\rho}_{mr}}. \quad (\text{A2})$$

For cases that introduce a new physical timescale, results that account for the residual effect of radiation after equality (which precedes decoupling) are not as tractable, in which case we replace  $a_{\text{eq}}$  with zero and  $\bar{\rho}_{mr}$  with  $\bar{\rho}_{cb}$ . The various models we study also impact the drag horizon, but we only consider regimes in which deviations in the expansion history become most important well after decoupling, in which case the effect on  $r_d$  is smaller than that on  $\chi(a_d, a_m)$  by at least an order of magnitude (as could be anticipated from Fig. [6](#)). That said, computing the change to  $r_d$  would only require a straightforward modification of the calculations presented before (by including the plasma sound speed in the integrand).

#### a. Massive neutrinos

Section [II A 2](#) presents a simplified, piecewise approximation to the MEDI that treats neutrinos' nonrelativistic transition as instantaneous, which we now improve upon by accounting for their rather gradual transition. We first write the perturbation to the density in a Universe with fully relativistic neutrinos in the form

$$\frac{\bar{\rho} - \bar{\rho}_{mr}}{\bar{\rho}_{mr}} = \frac{\bar{\rho}_{\nu,\text{rel}}}{\bar{\rho}_{mr}} \frac{\bar{\rho}_{\nu} - \bar{\rho}_{\nu,\text{rel}}}{\bar{\rho}_{\nu,\text{rel}}} = \frac{f_{\nu} a_{\nu}}{a + a_{\text{eq}}} \frac{\bar{\rho}_{\nu} - \bar{\rho}_{\nu,\text{rel}}}{\bar{\rho}_{\nu,\text{rel}}}, \quad (\text{A3})$$

where  $a_{\nu} \equiv \langle ap/m_{\nu} \rangle = \langle p/T_{\nu} \rangle T_{\nu,0}/m_{\nu}$  and  $f_{\nu} = m_{\nu} \bar{n}_{\nu}/\bar{\rho}_m$  as in Sec. [II A 2](#). Analytic expressions for Eq. [\(A3\)](#) are not possible for general  $T_{\nu}/m_{\nu}$  but are in the nonrelativistic and relativistic limits. Since the energy density in a single neutrino eigenstate is

$$\bar{\rho}_{\nu} = 2 \int \frac{d^3p}{(2\pi)^3} \frac{\sqrt{p^2 + m_{\nu}^2}}{e^{p/T_{\nu}} + 1} = 2 \int \frac{d^3p}{(2\pi)^3} \frac{1}{e^{p/T_{\nu}} + 1} \cdot \begin{cases} p + m_{\nu}^2/2p, & m_{\nu} \ll T_{\nu}, \\ m_{\nu}, & m_{\nu} \gg T_{\nu}, \end{cases} \quad (\text{A4})$$

keeping only the term leading-order in  $m_{\nu}/T_{\nu}$  in each limit, the perturbation to the energy density takes the form

$$\frac{\bar{\rho}_{\nu} - \bar{\rho}_{\nu,\text{rel}}}{\bar{\rho}_{\nu,\text{rel}}} \simeq \begin{cases} \frac{1}{2} \frac{\langle T_{\nu}/p \rangle}{\langle p/T_{\nu} \rangle} \left( \frac{m_{\nu}}{T_{\nu}} \right)^2, & m_{\nu} \ll T_{\nu}, \\ \frac{1}{\langle p/T_{\nu} \rangle} \frac{m_{\nu}}{T_{\nu}} - 1. & \end{cases} \quad (\text{A5})$$

Here angled brackets denote phase-space averages, which are written such that they each evaluate to a single number:  $\langle T_{\nu}/p \rangle \approx 0.456144$  and  $\langle p/T_{\nu} \rangle \approx 3.15137$ .

To proceed, we separate the integral Eq. (A2) into these two regimes at some scale factor  $a_\times$  near  $T_{\nu,0}/m_\nu$  (specified below), yielding

$$\frac{\Delta\chi(a_d, a_m)}{1/H_{100}\sqrt{\omega_{cb}}} \simeq -f_\nu \left( \frac{\langle T_\nu/p \rangle \langle p/T_\nu \rangle}{2} \left[ \frac{a^2 - 4aa_{\text{eq}} - 8a_{\text{eq}}^2}{3a_\nu\sqrt{a+a_{\text{eq}}}} \right]_{a_d}^{a_\times} + \left[ \frac{a + 2a_{\text{eq}} + a_\nu}{\sqrt{a+a_{\text{eq}}}} \right]_{a_\times}^{a_m} \right), \quad (\text{A6})$$

where  $a_\nu \equiv \langle ap/m_\nu \rangle = \langle p/T_\nu \rangle T_{\nu,0}/m_\nu$  as in Sec. II A 2. We do not distinguish between neutrino eigenstates above since in practice we take a degenerate hierarchy, but one could do so by summing over the contribution of each. We are free to choose  $a_\times$  different from  $a_\nu$  to minimize errors over some range of masses; we find  $a_\times \approx 1.32a_\nu$  to be roughly optimal for  $z_m = 2.330$ , yielding subpercent errors in the sensitivity coefficient for  $0.02 \lesssim M_\nu/\text{eV} \lesssim 0.3$ . The only other approximation errors in Eq. (A6) are  $\mathcal{O}(f_\nu)$  [i.e., in the small correction itself, which is the  $\mathcal{O}(f_\nu^2)$  error made in Eq. (A2) to begin with], which is only  $\gtrsim 10\%$  for  $M_\nu \gtrsim 1.3$  eV, and those when  $a_\nu$  is not much greater than  $a_m$ . The further simplifications made in Eq. (2.6) by taking  $a_{\text{eq}}$  and  $a_d$  negligible compared to  $a_m$  and  $a_\nu$  only marginally increase this error.

### b. Hyperlight scalar fields

The gravitational effects of sufficiently light scalar fields closely resemble those of massive neutrinos [12–16]—in particular, misaligned scalars that begin oscillating after decoupling and are therefore hyperlight, i.e., have mass  $H_0 \ll m_\phi < H(a_\star) \approx 3 \times 10^{-29}$  eV  $\ll H(a_{\text{eq}})$  and can only be a subcomponent of dark matter. At early times while frozen, they contribute to the stress-energy tensor as (a negligible amount of) dark energy and subsequently redshift like matter once oscillating; in the hyperlight mass range, they increase the matter abundance after decoupling like massive neutrinos. They also do not cluster on observable scales [12, 120]. Such light scalars cannot be both nonrelativistic and a thermal relic, for which reason their late-time abundance is determined by not just their mass (as for neutrinos) but also their (nonthermal) initial conditions. As such, hyperlight scalars make for a similar but distinct application of the approximation Eq. (2.3) of the MEDI, in which  $\omega_m \geq \omega_{cb}$  and  $a_\times$  are separate free parameters. Like for massive neutrinos, the simple piecewise treatment of Eq. (2.3) provides a good estimate; however, the result may in fact be computed analytically with the perturbative method described in Sec. III B, using analytic solutions for the scalar dynamics in a matter-dominated Universe.

Unlike neutrino masses (which identify a special temperature and therefore scale factor), the scalar’s mass introduces a physical timescale to the problem, so we take a pure-matter Universe. Hyperlight scalars whose mass satisfies  $H(a_m) \ll m_\phi \ll H(a_{\text{eq}})$  begin oscillating when  $m_\phi = 3H(a_{\text{osc}})/2$ . The homogeneous value of a hyperlight scalar field initially misaligned at  $\bar{\phi}_i$  evolves according to  $\bar{\phi}(t)/\bar{\phi}_i = \sin(m_\phi t)/m_\phi t = \sin(m_\phi t)/[a(t)/a_{\text{osc}}]^{3/2}$  [see, e.g., 16]. Here  $a_{\text{osc}} \simeq \sqrt[3]{9/4} (m_\phi/\sqrt{\omega_{cb}}H_{100})^{-2/3}$  is defined such that, at  $a \gg a_{\text{osc}}$ , the scalar’s energy density  $\bar{\rho}_\phi = (d\bar{\phi}/dt)^2/2 + m_\phi^2\bar{\phi}^2/2$  oscillates about  $m_\phi^2\bar{\phi}_i^2/2(a/a_{\text{osc}})^3$ , where  $m_\phi^2\bar{\phi}_i^2/2$  is the early-time energy density in the frozen condensate. As such, at late times the scalar comprises a fraction  $f_\phi = 3(\bar{\phi}_i/\sqrt{2}M_{\text{pl}})^2/4$  of the total matter density.

The correction to the MEDI from a hyperlight scalar,

$$\frac{\Delta\chi(a_d, a_m)}{1/H_{100}\sqrt{\omega_{cb}}} \simeq -\frac{1}{2} \int_{a_d}^{a_m} \frac{da}{\sqrt{a}} \frac{\bar{\rho}_\phi}{\rho_{cb}} \simeq -\frac{f_\phi}{2} \int_{a_d}^{a_m} \frac{da}{\sqrt{a}} \frac{(a/a_{\text{osc}})^3 \bar{\rho}_\phi}{m_\phi^2\bar{\phi}_i^2/2}, \quad (\text{A7})$$

has an unilluminating form in terms of special functions, but for  $H(a_m) \ll m_\phi \ll H(a_d)$  we need

only its asymptotic forms. The final result,

$$\frac{\Delta\chi(a_d, a_m)}{1/H_{100}\sqrt{\omega_{cb}}} \simeq -f_\phi \left[ \sqrt{a_m} \left( 1 + \frac{\cos(2m_\phi t_m)/15 - \sin^2(m_\phi t_m)/5}{(a_m/a_{\text{osc}})^3} \right) - \frac{\sqrt{3a_{\text{osc}}}\Gamma(1/3)}{5\sqrt[3]{2}} - \sqrt{a_d} \frac{(a_d/a_{\text{osc}})^3}{7} \right], \quad (\text{A8})$$

with  $m_\phi t_m = (a_m/a_{\text{osc}})^{3/2}$ , is accurate to  $\mathcal{O}(f_\phi)$  [i.e., the subleading corrections to Eq. (A2)], but incurs increasingly large errors as  $m_\phi$  approaches  $H(a_{\text{eq}}) \simeq 2.2 \times 10^{-28}$  eV from neglecting radiation's impact on Eq. (A7) both explicitly and on the solution  $\phi(t)$ . The dependence of Eq. (A8) on  $a_d$  is negligible (and subdominant to the errors from neglecting radiation). Equation (A8) also breaks down for  $m_\phi < 3H(a_m)$ , since  $a_m$  is no longer much greater than  $a_{\text{osc}}$ ; the sinusoidal terms in Eq. (A8) improve the accuracy for masses just above  $3H(a_m)$  by accounting for the initial oscillations of  $\bar{\rho}_\phi$  but do not qualitatively alter the result. Dropping the aforementioned terms yields

$$\frac{\Delta\chi(a_d, a_m)}{1/H_{100}\sqrt{\omega_{cb}}} \simeq -f_\phi \sqrt{a_m} \left[ 1 - \sqrt{a_{\text{osc}}/a_m} \Gamma(1/3) \sqrt{3}/5\sqrt[3]{2} \right]. \quad (\text{A9})$$

The numerical coefficient multiplying  $\sqrt{a_{\text{osc}}/a_m}$  is about  $-0.74$ , whose difference from unity (as would be derived in a piecewise approximation to the MEDI) accounts for the scalar's impact at early times before it rapidly oscillates.

Because their phenomenology is so similar to massive neutrinos, with their suppression of structure growth even sharing a close quantitative relationship to their impact on the MEDI, we do not present a dedicated analysis of hyperlight scalars. The analytic results Eqs. (2.6) and (A9) allow for a straightforward translation of constraints on the neutrino fraction to the scalar fraction as a function of the scalar mass.

### c. Decaying dark matter

Section III B 1 discusses decaying dark matter as a nearly instantaneous reduction in the matter density; we now account for both the relativistic decay products and the early phase of decay. The decay of nonrelativistic dark matter into dark radiation (whose energy densities are labeled  $\bar{\rho}_{\text{ddm}}$  and  $\bar{\rho}_{\text{ddr}}$ , respectively) with general rate  $\Gamma_{\text{dd}}(t)$  is described by the Boltzmann equations

$$\frac{d(a^3 \bar{\rho}_{\text{ddm}})}{dt} = -\Gamma_{\text{dd}} a^3 \bar{\rho}_{\text{ddm}} \quad (\text{A10a})$$

$$\frac{d(a^4 \bar{\rho}_{\text{ddr}})}{dt} = a \Gamma_{\text{dd}} a^3 \bar{\rho}_{\text{ddm}}, \quad (\text{A10b})$$

which have formal solutions

$$a(t)^3 \bar{\rho}_{\text{ddm}}(t) = a(t_i)^3 \bar{\rho}_{\text{ddm}}(t_i) \exp \left[ - \int_{t_i}^t dt' \Gamma_{\text{dd}}(t') \right] \quad (\text{A11a})$$

$$a(t)^4 \bar{\rho}_{\text{ddr}}(t) = a(t_i)^4 \bar{\rho}_{\text{ddr}}(t_i) + a(t_i)^3 \bar{\rho}_{\text{ddm}}(t_i) \int_{t_i}^t dt' a(t') \Gamma_{\text{dd}}(t') \exp \left[ - \int_{t_i}^{t'} dt'' \Gamma_{\text{dd}}(t'') \right]. \quad (\text{A11b})$$

With a time-independent decay rate, the integral in Eq. (A11a) is trivial, but the outer integral in Eq. (A11b) is not, as it depends explicitly on both time and scale factor. That is, we took  $\Gamma_{\text{dd}}$  to

be a physical time scale, so as in Appendix A1b we restrict results to matter domination in which  $a \propto t^{2/3}$ . The remaining integral has the asymptotic expansions of the form

$$\int dx x^n e^{-x} = -\Gamma(1+n) + x^n \left[ \frac{x}{1+n} - \frac{x^2}{2+n} + \mathcal{O}(x^3) \right] \quad (\text{A12a})$$

$$= e^{-x} \left[ -1 - \frac{n}{x} + \mathcal{O}(x^{-2}) \right], \quad (\text{A12b})$$

where  $n = 2/3$  and  $x = \Gamma_{\text{dd}} t$  in our case.

Like for massive neutrinos in Appendix A1a, we resort to splitting the integral at  $a_\times$  into the two regimes of Eq. (A12) and choose an optimal value for  $a_\times$  after the fact. Taking  $\bar{\rho}_{\text{ddr}}(t_i) = 0$ ,  $t_i \rightarrow 0$ , and  $a(t)/a_{\text{dd}} = (\Gamma_{\text{dd}} t)^{2/3}$  (which defines  $a_{\text{dd}}$ ), Eq. (A11) becomes

$$\bar{\rho}_{\text{ddm}}(a) = \frac{a(t_i)^3 \bar{\rho}_{\text{ddm}}(t_i)}{a^3} e^{-(a/a_{\text{dd}})^{3/2}} \quad (\text{A13a})$$

$$\bar{\rho}_{\text{ddr}}(a) = \frac{a_{\text{dd}} a(t_i)^3 \bar{\rho}_{\text{ddm}}(t_i)}{a^4} \begin{cases} 3(a/a_{\text{dd}})^{5/2}/5, & a \ll a_{\text{dd}}, \\ \Gamma(5/3) - e^{-(a/a_{\text{dd}})^{3/2}}, & a \gg a_{\text{dd}}. \end{cases} \quad (\text{A13b})$$

The perturbation to the matter density (where  $\bar{\rho}_m$  is that if the decaying species were stable) thus has early- and late-time behavior given by

$$\frac{\bar{\rho} - \bar{\rho}_m}{\bar{\rho}_m} = f_{\text{ddm}} \begin{cases} -2(a/a_{\text{dd}})^{3/2}/5, & a \ll a_{\text{dd}}, \\ -1 + \frac{\Gamma(5/3)}{a/a_{\text{dd}}}, & a \gg a_{\text{dd}}, \end{cases} \quad (\text{A14})$$

where  $f_{\text{ddm}} = \lim_{a \rightarrow 0} \bar{\rho}_{\text{ddm}}(a)/\bar{\rho}_m(a)$  is the fraction of matter (by energy density) that decays. Equation (A2) evaluates to

$$\frac{\Delta\chi(a_{\text{d}}, a_{\text{m}})}{1/H_{100}\sqrt{\omega_m}} \simeq f_{\text{ddm}} \left( \frac{\sqrt{a_{\text{dd}}}}{10} \left[ \left( \frac{a}{a_{\text{dd}}} \right)^2 \right]_{a_{\text{d}}}^{a_\times} + \left[ \sqrt{a} \left( 1 + \frac{\Gamma(5/3)}{a/a_{\text{dd}}} \right) \right]_{a_\times}^{a_{\text{m}}} \right), \quad (\text{A15})$$

which, when taking  $a_\times = 1.12a_{\text{dd}}$ , is accurate at the percent level for  $a_{\text{dd}} \lesssim a_{\text{m}}/2$  (up to corrections next-to-leading in  $f_{\text{ddm}}$ ), with a marginal increase in error as  $a_{\text{dd}}$  approaches  $a_{\text{eq}}$ . Here  $\omega_m = \lim_{a \rightarrow 0} a^3 \bar{\rho}_m(a)/3H_{100}^2 M_{\text{pl}}^2$ . Taking  $a_{\text{d}}/a_{\text{dd}}$  to zero yields Eq. (3.8).

Because the decay is exponentially fast, soon after  $\Gamma_{\text{dd}} t = 1$  the Universe is well described by decoupled matter and radiation (in different amounts than before decay). Therefore, a treatment of the postdecay regime that does not rely on a perturbative expansion in small  $f_{\text{ddm}}$  simply takes the standard matter–radiation result Eq. (2.2) with  $\omega_{cb}$  multiplied by  $1 - f_{\text{ddm}}$  and  $a_{\text{eq}}$  augmented to account for the relativistic decay products via  $a_{\text{eq}} = [a_{\text{eq}}|_{f_{\text{ddm}}=0} + \Gamma(5/3)f_{\text{ddm}}a_{\text{dd}}]/(1 - f_{\text{ddm}})$ .

#### d. Dark forces

Section III B 2 studies dark matter subject to a long-range force mediated by a linear coupling to a light scalar, in which the homogeneous dynamics of the scalar induce the dark matter particle mass to evolve with time. Employing analytic results from Ref. [27], we derive the analytic result for Eq. (A1) quoted in Sec. III B 2. The homogeneous mode of the mediator  $\bar{\varphi}$  evolves as  $\bar{\varphi}(a) = \bar{\varphi}_i - f_\chi d_{m_\chi}^{(1)}(1 - 1/y + 2 \ln y)$  where  $2y = 1 + \sqrt{1 + a/a_{\text{eq}}}$ , while the dark matter mass  $m_\chi$  evolves in proportion to  $e^{d_{m_\chi}^{(1)}(\bar{\varphi} - \bar{\varphi}_i)} \approx 1 + d_{m_\chi}^{(1)}(\bar{\varphi} - \bar{\varphi}_i)$ . Here  $f_\chi$  is the fraction of all matter

coupled to  $\varphi$  and  $d_{m_\chi}^{(1)}$  the linear coupling coefficient thereof; the force strength relative to gravity is  $\beta = (d_{m_\chi}^{(1)})^2$ . Note that  $y = 1 + \tau/4\sqrt{2}[a_{\text{eq}}H_{\text{eq}}]^{-1}$ , i.e., the dynamics are expressed uniquely in terms of conformal time; likewise, in a matter–radiation Universe,  $\tau/[a_{\text{eq}}H_{\text{eq}}]^{-1} = 2\sqrt{2}(\sqrt{1 + a/a_{\text{eq}}} - 1)$ . As such, Eq. (A1) may be integrated analytically with no approximation [other than working at  $\mathcal{O}(\beta f_\chi^2)$ ].

The perturbation to the energy density is

$$\frac{\bar{\rho}(a) - \bar{\rho}_{mr}(a)}{\bar{\rho}_{mr}(a)} = \frac{f_\chi [m_\chi(a)/m_\chi(a_i \rightarrow 0) - 1]}{1 + a_{\text{eq}}/a} + \frac{(d\bar{\varphi}/d \ln a)^2}{3}, \quad (\text{A16})$$

the two terms encoding the evolution of  $m_\chi$  and the contribution of the mediator’s kinetic energy. Taking a cue from the analytic solution for  $\bar{\varphi}$ , it proves expedient to change variables to  $y$  itself, such that

$$\frac{\Delta\chi(a_d, a_m)}{1/H_{100}\sqrt{\omega_{cb}}} \simeq \sqrt{a_{\text{eq}}}\beta f_\chi^2 \left[ \frac{2y(2 \ln y - 1)}{1 - 1/2y} - \frac{2y}{3} - 4 \ln y + 1 + \frac{4y - 1}{3y^2(1 - 1/2y)} \right]_{y(a_d)}^{y(a_m)}. \quad (\text{A17})$$

The sensitivity coefficient  $\partial \ln \chi(a_d, a_m)/\partial (1 + \beta f_\chi^2)$  evaluates to 2.2867 for  $a_m = 1/(1 + 2.330)$ , which matches the numerical result up to corrections at next-to-leading order in  $\beta f_\chi^2$ . Since our interest is  $a_m \gg a_d > a_{\text{eq}}$  [and thus  $y(a_m) \gg 1$ ], Eq. (3.9) presents the leading-order behavior of Eq. (A17), neglecting the lower boundary of the integral as well. This result could be further generalized to mediators with masses larger than  $H_0$  using analytic solutions from Ref. [27], accounting for the mediator’s late-time abundance with a calculation analogous to that for uncoupled scalars in Appendix A1b.

## 2. Numerical implementation

The combination of CMB data we use includes foreground-marginalized ACT DR6 temperature and polarization data (with likelihood implemented in `candl` [121]) and a subset of *Planck* PR3 observations [59] prescribed by Ref. [2] for combination with ACT, restricted to multipoles  $\ell \leq 1000$  in temperature and  $\leq 600$  in polarization and temperature-polarization cross correlation and including the  $\ell < 30$  temperature and polarization likelihoods from PR3. Specifically, we use the foreground-marginalized `Plik_lite` variants with `Commander` and `SimAll` for  $\ell < 30$  [1, 59, 122]. We truncate the ACT likelihood at  $\ell = 4000$  to mitigate needless computational cost (see Ref. [27]). Following Ref. [3], we also include SPT-3G D1 [3] data without further amendments. We include no lensing reconstruction data.

For models that significantly modify dynamics before decoupling (those considered in Sec. III A), we use the Boltzmann code `CLASS` [123, 124]; we use `CAMB` [125] for the varying neutrino mass results presented in Fig. 3. We employ precision settings as enumerated in Appendix D of Ref. [27]. We perform parameter sampling with `emcee` [107–109], running long enough to obtain at least  $10^4$  independent samples. We take standard priors for  $\Lambda$ CDM parameters:  $\omega_b \sim \mathcal{U}(0.005, 0.035)$ ,  $\omega_c \sim \mathcal{U}(0.01, 0.25)$ ,  $100\theta_s \sim \mathcal{U}(0.9, 1.1)$ ,  $\tau_{\text{reio}} \sim \mathcal{U}(0.02, 0.2)$ , scalar spectral amplitude  $A_s$  via  $\ln(10^{10}A_s) \sim \mathcal{U}(1.61, 3.91)$ , scalar spectral tilt  $n_s \sim \mathcal{U}(0.8, 1.2)$ , and  $M_\nu/\text{eV} \sim \mathcal{U}(0, 1.5)$ . Here  $\mathcal{U}(a, b)$  specifies a uniform distribution between  $a$  and  $b$  and  $\mathcal{N}(\mu, \sigma)$  a normal distribution with mean  $\mu$  and standard deviation  $\sigma$ . For the extensions in Sec. III A, we sample  $\Delta N_{\text{eff}} \sim \mathcal{U}(-2, 3)$  and the early-time values of the electron mass and fine structure constant relative to their present values,  $m_{e,i}/m_{e,0} \sim \mathcal{U}(0.7, 1.3)$  and  $\alpha_i/\alpha_0 \sim \mathcal{U}(0.7, 1.3)$ . When varying either of the latter, we replace  $\omega_b$  with  $\tilde{\omega}_b = \omega_b / (m_{e,i}\alpha_i^2/m_{e,0}\alpha_0^2)$  and likewise for  $\omega_c$ , each sampled from the same prior

as above. The posterior over these parameters is more efficiently sampled because the rescaling removes the degeneracy with  $a_*$  [per Eqs. (3.1) and (3.2)].

For all other results that do not rely on a Boltzmann code, we employ a prior on the angular extent of the sound horizon and the baryon and CDM densities (via  $R_*$  and  $x_{\text{eq}}$ , as defined in Sec. III A) derived from  $\Lambda$ CDM fit to the aforementioned primary CMB data. The background evolution in such cases is implemented with JAX [118] with ordinary differential equation solvers supplied by DiffraX [119]. In these cases, we sample  $\omega_b \sim \mathcal{U}(0.02, 0.025)$ ,  $\omega_c \sim \mathcal{U}(0.01, 0.5)$ , and  $\omega_{\text{DE}} \sim \mathcal{U}(0.0, 1.0)$ . The narrower prior on the baryon density, which is nearly centered on the values preferred by the CMB (and BBN) with width of 30–40  $\sigma$ , minimizes changes to the recombination history (which we do not model) while still allowing for substantial variation in  $r_{\text{d}}$ .

The extensions in Sec. III A sample the curvature density  $\omega_k \sim \mathcal{U}(-0.5, 0.5)$ , the would-be present density in decaying dark matter  $\tilde{\omega}_{\text{ddm}} \equiv \lim_{a \rightarrow 0} a^3 \bar{\rho}_{\text{ddm}} / 3H_{100}^2 M_{\text{pl}}^2 \sim \mathcal{U}(0.0, 0.1)$ , or the analogously defined density in coupled dark matter  $\tilde{\omega}_\chi \sim \mathcal{U}(0.01, 0.5)$  and the coupling strength relative to gravity  $\beta \sim \mathcal{U}(10^{-6}, 0.1)$ . For dynamical dark energy (Secs. II B 2 and III D 2), we sample the present equation of state  $w_0 \sim \mathcal{U}(-3, 1)$  and, for the linear-in- $a$  model,  $w_\infty = \lim_{a \rightarrow 0} w(a) = w_0 + w_a \sim \mathcal{U}(-20, 0)$ . Unlike those in Ref. [6], these priors do not truncate a nonnegligible fraction of the posterior in the  $w_a$  direction.

- 
- [1] N. Aghanim *et al.* (Planck), Planck 2018 results. VI. Cosmological parameters, *Astron. Astrophys.* **641**, A6 (2020), [Erratum: *Astron. Astrophys.* 652, C4 (2021)], [arXiv:1807.06209 \[astro-ph.CO\]](#).
  - [2] T. Louis *et al.* (ACT), The Atacama Cosmology Telescope: DR6 Power Spectra, Likelihoods and  $\Lambda$ CDM Parameters, [arXiv:2503.14452 \[astro-ph.CO\]](#) (2025).
  - [3] E. Camphuis *et al.* (SPT-3G), SPT-3G D1: CMB temperature and polarization power spectra and cosmology from 2019 and 2020 observations of the SPT-3G Main field, [arXiv:2506.20707 \[astro-ph.CO\]](#) (2025).
  - [4] D. J. Fixsen, E. S. Cheng, J. M. Gales, J. C. Mather, R. A. Shafer, and E. L. Wright, The Cosmic Microwave Background spectrum from the full COBE FIRAS data set, *Astrophys. J.* **473**, 576 (1996), [arXiv:astro-ph/9605054](#).
  - [5] J. C. Mather *et al.*, Measurement of the Cosmic Microwave Background spectrum by the COBE FIRAS instrument, *Astrophys. J.* **420**, 439 (1994).
  - [6] M. Abdul Karim *et al.* (DESI), DESI DR2 results. II. Measurements of baryon acoustic oscillations and cosmological constraints, *Phys. Rev. D* **112**, 083515 (2025), [arXiv:2503.14738 \[astro-ph.CO\]](#).
  - [7] M. Loverde and Z. J. Weiner, Massive neutrinos and cosmic composition, *JCAP* **12**, 048, [arXiv:2410.00090 \[astro-ph.CO\]](#).
  - [8] A. G. Adame *et al.* (DESI), DESI 2024 VI: cosmological constraints from the measurements of baryon acoustic oscillations, *JCAP* **02**, 021, [arXiv:2404.03002 \[astro-ph.CO\]](#).
  - [9] D. J. Eisenstein and M. J. White, Theoretical uncertainty in baryon oscillations, *Phys. Rev. D* **70**, 103523 (2004), [arXiv:astro-ph/0407539](#).
  - [10] L. Knox, On precision measurement of the mean curvature, *Phys. Rev. D* **73**, 023503 (2006), [arXiv:astro-ph/0503405](#).
  - [11] J. Lesgourgues and S. Pastor, Neutrino mass from Cosmology, *Adv. High Energy Phys.* **2012**, 608515 (2012), [arXiv:1212.6154 \[hep-ph\]](#).
  - [12] L. Amendola and R. Barbieri, Dark matter from an ultra-light pseudo-Goldstone-boson, *Phys. Lett. B* **642**, 192 (2006), [arXiv:hep-ph/0509257](#).
  - [13] D. J. E. Marsh, E. Macaulay, M. Trebitsch, and P. G. Ferreira, Ultra-light Axions: Degeneracies with Massive Neutrinos and Forecasts for Future Cosmological Observations, *Phys. Rev. D* **85**, 103514 (2012), [arXiv:1110.0502 \[astro-ph.CO\]](#).
  - [14] R. Hlozek, D. Grin, D. J. E. Marsh, and P. G. Ferreira, A search for ultralight axions using precision cosmological data, *Phys. Rev. D* **91**, 103512 (2015), [arXiv:1410.2896 \[astro-ph.CO\]](#).
  - [15] R. Hlozek, D. J. E. Marsh, D. Grin, R. Allison, J. Dunkley, and E. Calabrese, Future CMB tests of dark

- matter: Ultralight axions and massive neutrinos, *Phys. Rev. D* **95**, 123511 (2017), [arXiv:1607.08208 \[astro-ph.CO\]](#).
- [16] M. Baryakhtar, O. Simon, and Z. J. Weiner, Cosmology with varying fundamental constants from hyperlight, coupled scalars, *Phys. Rev. D* **110**, 083505 (2024), [arXiv:2405.10358 \[astro-ph.CO\]](#).
- [17] M. S. Turner, Cosmology with Decaying Particles, *Phys. Rev. D* **31**, 1212 (1985).
- [18] É. Aubourg *et al.* (BOSS), Cosmological implications of baryon acoustic oscillation measurements, *Phys. Rev. D* **92**, 123516 (2015), [arXiv:1411.1074 \[astro-ph.CO\]](#).
- [19] V. Poulin, P. D. Serpico, and J. Lesgourgues, A fresh look at linear cosmological constraints on a decaying dark matter component, *JCAP* **08**, 036, [arXiv:1606.02073 \[astro-ph.CO\]](#).
- [20] T. Bringmann, F. Kahlhoefer, K. Schmidt-Hoberg, and P. Walia, Converting nonrelativistic dark matter to radiation, *Phys. Rev. D* **98**, 023543 (2018), [arXiv:1803.03644 \[astro-ph.CO\]](#).
- [21] F. McCarthy and J. C. Hill, Converting dark matter to dark radiation does not solve cosmological tensions, *Phys. Rev. D* **108**, 063501 (2023), [arXiv:2210.14339 \[astro-ph.CO\]](#).
- [22] G. P. Lynch and L. Knox, What's the matter with  $\Sigma m\nu$ ?, *Phys. Rev. D* **112**, 083543 (2025), [arXiv:2503.14470 \[astro-ph.CO\]](#).
- [23] T. Montandon, V. Poulin, T. Rink, and T. Schwetz, Neutrino mass limits and decaying dark matter: background evolution versus perturbations, [arXiv:2603.03284 \[astro-ph.CO\]](#) (2026).
- [24] M. Archidiacono, E. Castorina, D. Redigolo, and E. Salvioni, Unveiling dark fifth forces with linear cosmology, *JCAP* **10**, 074, [arXiv:2204.08484 \[astro-ph.CO\]](#).
- [25] S. Bottaro, E. Castorina, M. Costa, D. Redigolo, and E. Salvioni, Unveiling Dark Forces with Measurements of the Large Scale Structure of the Universe, *Phys. Rev. Lett.* **132**, 201002 (2024), [arXiv:2309.11496 \[astro-ph.CO\]](#).
- [26] S. Bottaro, E. Castorina, M. Costa, D. Redigolo, and E. Salvioni, From 100 kpc to 10 Gpc: Dark matter self-interactions before and after DESI observations, *Phys. Rev. D* **112**, 023525 (2025), [arXiv:2407.18252 \[astro-ph.CO\]](#).
- [27] M. Costa, C. Creque-Sarbinowski, O. Simon, and Z. J. Weiner, Dark forces suppress structure growth, [arXiv:2510.00098 \[astro-ph.CO\]](#) (2025).
- [28] T. Sekiguchi and T. Takahashi, Early recombination as a solution to the  $H_0$  tension, *Phys. Rev. D* **103**, 083507 (2021), [arXiv:2007.03381 \[astro-ph.CO\]](#).
- [29] M. M. Ivanov, Y. Ali-Haïmoud, and J. Lesgourgues,  $H_0$  tension or  $T_0$  tension?, *Phys. Rev. D* **102**, 063515 (2020), [arXiv:2005.10656 \[astro-ph.CO\]](#).
- [30] M. Wyman, D. H. Rudd, R. A. Vanderveld, and W. Hu, Neutrinos Help Reconcile Planck Measurements with the Local Universe, *Phys. Rev. Lett.* **112**, 051302 (2014), [arXiv:1307.7715 \[astro-ph.CO\]](#).
- [31] C. Dvorkin, M. Wyman, D. H. Rudd, and W. Hu, Neutrinos help reconcile Planck measurements with both the early and local Universe, *Phys. Rev. D* **90**, 083503 (2014), [arXiv:1403.8049 \[astro-ph.CO\]](#).
- [32] J. L. Bernal, L. Verde, and A. G. Riess, The trouble with  $H_0$ , *JCAP* **10**, 019, [arXiv:1607.05617 \[astro-ph.CO\]](#).
- [33] V. Poulin, T. L. Smith, T. Karwal, and M. Kamionkowski, Early Dark Energy Can Resolve The Hubble Tension, *Phys. Rev. Lett.* **122**, 221301 (2019), [arXiv:1811.04083 \[astro-ph.CO\]](#).
- [34] V. Poulin, T. L. Smith, D. Grin, T. Karwal, and M. Kamionkowski, Cosmological implications of ultralight axionlike fields, *Phys. Rev. D* **98**, 083525 (2018), [arXiv:1806.10608 \[astro-ph.CO\]](#).
- [35] T. L. Smith, V. Poulin, and M. A. Amin, Oscillating scalar fields and the Hubble tension: a resolution with novel signatures, *Phys. Rev. D* **101**, 063523 (2020), [arXiv:1908.06995 \[astro-ph.CO\]](#).
- [36] J. C. Hill, E. McDonough, M. W. Toomey, and S. Alexander, Early dark energy does not restore cosmological concordance, *Phys. Rev. D* **102**, 043507 (2020), [arXiv:2003.07355 \[astro-ph.CO\]](#).
- [37] V. Poulin, T. L. Smith, and T. Karwal, The Ups and Downs of Early Dark Energy solutions to the Hubble tension: A review of models, hints and constraints circa 2023, *Phys. Dark Univ.* **42**, 101348 (2023), [arXiv:2302.09032 \[astro-ph.CO\]](#).
- [38] N. Sailer, G. S. Farren, S. Ferraro, and M. White, Addressing Tensions in  $\Lambda$ CDM Cosmology by an Increase in the Optical Depth to Reionization, *Phys. Rev. Lett.* **136**, 081002 (2026), [arXiv:2504.16932 \[astro-ph.CO\]](#).
- [39] T. Jhaveri, T. Karwal, and W. Hu, Turning a negative neutrino mass into a positive optical depth, *Phys. Rev. D* **112**, 043541 (2025), [arXiv:2504.21813 \[astro-ph.CO\]](#).
- [40] W. Hu, Dark energy probes in light of the CMB, *ASP Conf. Ser.* **339**, 215 (2005), [arXiv:astro-ph/0407158](#).

- [41] S. Weinberg, *Cosmology* (2008).
- [42] S. Ilić, M. Kopp, C. Skordis, and D. B. Thomas, Dark matter properties through cosmic history, *Phys. Rev. D* **104**, 043520 (2021), [arXiv:2004.09572 \[astro-ph.CO\]](#).
- [43] Z. Hou *et al.*, Constraints on Cosmology from the Cosmic Microwave Background Power Spectrum of the 2500 deg<sup>2</sup> SPT-SZ Survey, *Astrophys. J.* **782**, 74 (2014), [arXiv:1212.6267 \[astro-ph.CO\]](#).
- [44] P. F. de Salas, D. V. Forero, S. Gariazzo, P. Martínez-Miravé, O. Mena, C. A. Ternes, M. Tórtola, and J. W. F. Valle, 2020 global reassessment of the neutrino oscillation picture, *JHEP* **02**, 071, [arXiv:2006.11237 \[hep-ph\]](#).
- [45] I. Esteban, M. C. Gonzalez-Garcia, M. Maltoni, T. Schwetz, and A. Zhou, The fate of hints: updated global analysis of three-flavor neutrino oscillations, *JHEP* **09**, 178, [arXiv:2007.14792 \[hep-ph\]](#).
- [46] M. Baes, P. Camps, and D. Van De Putte, Analytical expressions and numerical evaluation of the luminosity distance in a flat cosmology, *Mon. Not. Roy. Astron. Soc.* **468**, 927 (2017), [arXiv:1702.08860 \[astro-ph.CO\]](#).
- [47] W. Lin, X. Chen, and K. J. Mack, Early Universe Physics Insensitive and Uncalibrated Cosmic Standards: Constraints on  $\Omega_m$  and Implications for the Hubble Tension, *Astrophys. J.* **920**, 159 (2021), [arXiv:2102.05701 \[astro-ph.CO\]](#).
- [48] M. Garny, F. Niedermann, and M. S. Sloth, Dark Acoustic Oscillations as an Early-Universe Explanation of the DESI Anomaly, [arXiv:2512.15870 \[astro-ph.CO\]](#) (2025).
- [49] S. Bashinsky and U. Seljak, Neutrino perturbations in CMB anisotropy and matter clustering, *Phys. Rev. D* **69**, 083002 (2004), [arXiv:astro-ph/0310198](#).
- [50] D. Baumann, D. Green, J. Meyers, and B. Wallisch, Phases of New Physics in the CMB, *JCAP* **01**, 007, [arXiv:1508.06342 \[astro-ph.CO\]](#).
- [51] M. Abdul Karim *et al.* (DESI), DESI DR2 results. I. Baryon acoustic oscillations from the Lyman alpha forest, *Phys. Rev. D* **112**, 083514 (2025), [arXiv:2503.14739 \[astro-ph.CO\]](#).
- [52] A. Cuceu *et al.*, DESI DR1 Ly $\alpha$  forest: 3D full-shape analysis and cosmological constraints, [arXiv:2509.15308 \[astro-ph.CO\]](#) (2025).
- [53] M. Chevallier and D. Polarski, Accelerating universes with scaling dark matter, *Int. J. Mod. Phys. D* **10**, 213 (2001), [arXiv:gr-qc/0009008](#).
- [54] E. V. Linder, Exploring the expansion history of the universe, *Phys. Rev. Lett.* **90**, 091301 (2003), [arXiv:astro-ph/0208512](#).
- [55] J. L. Bernal, T. L. Smith, K. K. Boddy, and M. Kamionkowski, Robustness of baryon acoustic oscillation constraints for early-Universe modifications of  $\Lambda$ CDM cosmology, *Phys. Rev. D* **102**, 123515 (2020), [arXiv:2004.07263 \[astro-ph.CO\]](#).
- [56] A. G. Riess *et al.*, A Comprehensive Measurement of the Local Value of the Hubble Constant with 1 km s<sup>-1</sup> Mpc<sup>-1</sup> Uncertainty from the Hubble Space Telescope and the SH0ES Team, *Astrophys. J. Lett.* **934**, L7 (2022), [arXiv:2112.04510 \[astro-ph.CO\]](#).
- [57] W. L. Freedman, B. F. Madore, T. J. Hoyt, I. S. Jang, A. J. Lee, and K. A. Owens, Status Report on the Chicago-Carnegie Hubble Program (CCHP): Measurement of the Hubble Constant Using the Hubble and James Webb Space Telescopes, *Astrophys. J.* **985**, 203 (2025), [Erratum: *Astrophys. J.* 993, 252 (2025)], [arXiv:2408.06153 \[astro-ph.CO\]](#).
- [58] S. Casertano *et al.* (H0DN), The Local Distance Network: a community consensus report on the measurement of the Hubble constant at 1% precision, [arXiv:2510.23823 \[astro-ph.CO\]](#) (2025).
- [59] N. Aghanim *et al.* (Planck), Planck 2018 results. V. CMB power spectra and likelihoods, *Astron. Astrophys.* **641**, A5 (2020), [arXiv:1907.12875 \[astro-ph.CO\]](#).
- [60] L. Herold and M. Kamionkowski, Revisiting the impact of neutrino mass hierarchies on neutrino mass constraints in light of recent DESI data, *Phys. Rev. D* **111**, 083518 (2025), [arXiv:2412.03546 \[astro-ph.CO\]](#).
- [61] P. W. Graham, D. Green, and J. Meyers, New interpretations of the cosmological preference for a negative neutrino mass, *Phys. Rev. D* **113**, 043514 (2026), [arXiv:2508.20999 \[astro-ph.CO\]](#).
- [62] A. J. Ross, L. Samushia, C. Howlett, W. J. Percival, A. Burden, and M. Manera, The clustering of the SDSS DR7 main Galaxy sample – I. A 4 per cent distance measure at  $z = 0.15$ , *Mon. Not. Roy. Astron. Soc.* **449**, 835 (2015), [arXiv:1409.3242 \[astro-ph.CO\]](#).
- [63] S. Alam *et al.* (eBOSS), Completed SDSS-IV extended Baryon Oscillation Spectroscopic Survey: Cosmological implications from two decades of spectroscopic surveys at the Apache Point Observatory, *Phys. Rev. D* **103**, 083533 (2021), [arXiv:2007.08991 \[astro-ph.CO\]](#).

- [64] L. Pogosian, G.-B. Zhao, and K. Jedamzik, A Consistency Test of the Cosmological Model at the Epoch of Recombination Using DESI Baryonic Acoustic Oscillation and Planck Measurements, *Astrophys. J. Lett.* **973**, L13 (2024), [arXiv:2405.20306 \[astro-ph.CO\]](#).
- [65] S. H. Mirpoorian, K. Jedamzik, and L. Pogosian, Is dynamical dark energy necessary? DESI BAO and modified recombination, *JCAP* **12**, 050, [arXiv:2504.15274 \[astro-ph.CO\]](#).
- [66] W. Hu and M. J. White, Acoustic signatures in the cosmic microwave background, *Astrophys. J.* **471**, 30 (1996), [arXiv:astro-ph/9602019](#).
- [67] W. Hu and M. J. White, The Damping tail of CMB anisotropies, *Astrophys. J.* **479**, 568 (1997), [arXiv:astro-ph/9609079](#).
- [68] W. Hu and N. Sugiyama, Small scale cosmological perturbations: An Analytic approach, *Astrophys. J.* **471**, 542 (1996), [arXiv:astro-ph/9510117](#).
- [69] D. J. Eisenstein and W. Hu, Baryonic features in the matter transfer function, *Astrophys. J.* **496**, 605 (1998), [arXiv:astro-ph/9709112](#).
- [70] L. Hart and J. Chluba, Updated fundamental constant constraints from Planck 2018 data and possible relations to the Hubble tension, *Mon. Not. Roy. Astron. Soc.* **493**, 3255 (2020), [arXiv:1912.03986 \[astro-ph.CO\]](#).
- [71] K. Jedamzik and L. Pogosian, Relieving the Hubble tension with primordial magnetic fields, *Phys. Rev. Lett.* **125**, 181302 (2020), [arXiv:2004.09487 \[astro-ph.CO\]](#).
- [72] G. P. Lynch, L. Knox, and J. Chluba, Reconstructing the recombination history by combining early and late cosmological probes, *Phys. Rev. D* **110**, 063518 (2024), [arXiv:2404.05715 \[astro-ph.CO\]](#).
- [73] G. P. Lynch, L. Knox, and J. Chluba, DESI observations and the Hubble tension in light of modified recombination, *Phys. Rev. D* **110**, 083538 (2024), [arXiv:2406.10202 \[astro-ph.CO\]](#).
- [74] S. H. Mirpoorian, K. Jedamzik, and L. Pogosian, Modified recombination and the Hubble tension, *Phys. Rev. D* **111**, 083519 (2025), [arXiv:2411.16678 \[astro-ph.CO\]](#).
- [75] M. Baryakhtar, O. Simon, and Z. J. Weiner, Searching for coupled, hyperlight scalars across cosmic history, *Phys. Rev. D* **111**, 115026 (2025), [arXiv:2502.04432 \[hep-ph\]](#).
- [76] Z. Hou, R. Keisler, L. Knox, M. Millea, and C. Reichardt, How Massless Neutrinos Affect the Cosmic Microwave Background Damping Tail, *Phys. Rev. D* **87**, 083008 (2013), [arXiv:1104.2333 \[astro-ph.CO\]](#).
- [77] M. M. Saravanan, T. Brinckmann, M. Loverde, and Z. J. Weiner, Abundance and properties of dark radiation from the cosmic microwave background, *JCAP* **08**, 040, [arXiv:2503.04671 \[astro-ph.CO\]](#).
- [78] F. Ge, F.-Y. Cyr-Racine, and L. Knox, Scaling transformations and the origins of light relics constraints from cosmic microwave background observations, *Phys. Rev. D* **107**, 023517 (2023), [arXiv:2210.16335 \[astro-ph.CO\]](#).
- [79] E. Calabrese *et al.* (Atacama Cosmology Telescope), The Atacama Cosmology Telescope: DR6 constraints on extended cosmological models, *JCAP* **11**, 063, [arXiv:2503.14454 \[astro-ph.CO\]](#).
- [80] S. Hannestad, Possible constraints on the time variation of the fine structure constant from cosmic microwave background data, *Phys. Rev. D* **60**, 023515 (1999), [arXiv:astro-ph/9810102](#).
- [81] M. Kaplinghat, R. J. Scherrer, and M. S. Turner, Constraining variations in the fine structure constant with the cosmic microwave background, *Phys. Rev. D* **60**, 023516 (1999), [arXiv:astro-ph/9810133](#).
- [82] L. Hart and J. Chluba, New constraints on time-dependent variations of fundamental constants using Planck data, *Mon. Not. Roy. Astron. Soc.* **474**, 1850 (2018), [arXiv:1705.03925 \[astro-ph.CO\]](#).
- [83] S. Vagnozzi, Consistency tests of  $\Lambda$ CDM from the early integrated Sachs-Wolfe effect: Implications for early-time new physics and the Hubble tension, *Phys. Rev. D* **104**, 063524 (2021), [arXiv:2105.10425 \[astro-ph.CO\]](#).
- [84] E. Chaussidon *et al.*, Early time solution as an alternative to the late time evolving dark energy with DESI DR2 BAO, *Phys. Rev. D* **112**, 063548 (2025), [arXiv:2503.24343 \[astro-ph.CO\]](#).
- [85] A. R. Khalife *et al.* (SPT-3G), SPT-3G D1: Axion Early Dark Energy with CMB experiments and DESI, [arXiv:2507.23355 \[astro-ph.CO\]](#) (2025).
- [86] H. García Escudero, S. H. Mirpoorian, and L. Pogosian, Sound-horizon-agnostic Inference of the Hubble Constant and Neutrino Masses from Baryon Acoustic Oscillations, Cosmic Microwave Background Lensing, and Galaxy Weak Lensing and Clustering, *Astrophys. J. Lett.* **998**, L41 (2026), [arXiv:2509.16202 \[astro-ph.CO\]](#).
- [87] R. K. Sharma and J. Lesgourgues, Constraints on neutrino mass and dark energy agnostic to the sound horizon, *JCAP* **02**, 034, [arXiv:2510.15835 \[astro-ph.CO\]](#).
- [88] F. Ge *et al.* (SPT-3G), Cosmology from CMB lensing and delensed EE power spectra using 2019–2020

- SPT-3G polarization data, *Phys. Rev. D* **111**, 083534 (2025), [arXiv:2411.06000 \[astro-ph.CO\]](#).
- [89] N. Aghanim *et al.* (Planck), Planck intermediate results. LI. Features in the cosmic microwave background temperature power spectrum and shifts in cosmological parameters, *Astron. Astrophys.* **607**, A95 (2017), [arXiv:1608.02487 \[astro-ph.CO\]](#).
- [90] E. Calabrese, A. Slosar, A. Melchiorri, G. F. Smoot, and O. Zahn, Cosmic Microwave Weak lensing data as a test for the dark universe, *Phys. Rev. D* **77**, 123531 (2008), [arXiv:0803.2309 \[astro-ph\]](#).
- [91] L. Knox and M. Millea, Hubble constant hunter’s guide, *Phys. Rev. D* **101**, 043533 (2020), [arXiv:1908.03663 \[astro-ph.CO\]](#).
- [92] D. W. Hogg, Distance measures in cosmology, [arXiv:astro-ph/9905116](#) (1999).
- [93] S.-F. Chen and M. Zaldarriaga, It’s all Ok: curvature in light of BAO from DESI DR2, *JCAP* **08**, 014, [arXiv:2505.00659 \[astro-ph.CO\]](#).
- [94] T. Namikawa, Resolving the Negative Effective Neutrino Mass Parameter with Cosmic Birefringence, *Phys. Rev. Lett.* **135**, 161004 (2025), [arXiv:2506.22999 \[astro-ph.CO\]](#).
- [95] B. Popovic *et al.* (DES), The Dark Energy Survey Supernova Program: A Reanalysis Of Cosmology Results And Evidence For Evolving Dark Energy With An Updated Type Ia Supernova Calibration, [arXiv:2511.07517 \[astro-ph.CO\]](#) (2025).
- [96] W. Yang, E. Di Valentino, E. V. Linder, S. Zhang, and S. Pan, When One-Parameter Dark Energy Makes Neutrinos Physical Again, [arXiv:2603.15422 \[astro-ph.CO\]](#) (2026).
- [97] L. Herold and T. Karwal, Bayesian and frequentist perspectives agree on dynamical dark energy, [arXiv:2506.12004 \[astro-ph.CO\]](#) (2025).
- [98] R. de Belsunce, S.-F. Chen, M. M. Ivanov, C. Ravoux, S. Chabanier, J. Sexton, and Z. Lukic, Precision measurements of EFT parameters and BAO peak shifts for the Lyman- $\alpha$  forest, *Phys. Rev. D* **111**, 063524 (2025), [arXiv:2412.06892 \[astro-ph.CO\]](#).
- [99] F. Sinigaglia, F.-S. Kitaura, K. Nagamine, and Y. Oku, The Negative Baryon Acoustic Oscillation Shift in the Ly $\alpha$  Forest from Cosmological Simulations, *Astrophys. J. Lett.* **971**, L22 (2024), [arXiv:2407.03918 \[astro-ph.CO\]](#).
- [100] B. Hadzhiyska, R. de Belsunce, A. Cuceu, J. Guy, M. M. Ivanov, H. Coquinot, and A. Font-Ribera, Measuring and unbiasing the BAO shift in the Ly  $\alpha$  forest with AbacusSummit, *Mon. Not. Roy. Astron. Soc.* **540**, 1960 (2025), [arXiv:2503.13442 \[astro-ph.CO\]](#).
- [101] T. J. Hoyt, D. Rubin, G. Aldering, S. Perlmutter, A. Cuceu, and R. Gupta, Union3.1: Self-consistent Measurements of Host Galaxy Properties for 2000 Type Ia Supernovae, [arXiv:2601.19424 \[astro-ph.CO\]](#) (2026).
- [102] A. Bault *et al.*, Baryon Acoustic Oscillations from the C IV Forest with DESI DR2, [arXiv:2601.08103 \[astro-ph.CO\]](#) (2026).
- [103] N. Sailer, E. Castorina, S. Ferraro, and M. White, Cosmology at high redshift — a probe of fundamental physics, *JCAP* **12** (12), 049, [arXiv:2106.09713 \[astro-ph.CO\]](#).
- [104] D. J. Schlegel *et al.* (DESI), A Spectroscopic Road Map for Cosmic Frontier: DESI, DESI-II, Stage-5, [arXiv:2209.03585 \[astro-ph.CO\]](#) (2022).
- [105] D. J. Schlegel *et al.*, The MegaMapper: A Stage-5 Spectroscopic Instrument Concept for the Study of Inflation and Dark Energy, [arXiv:2209.04322 \[astro-ph.IM\]](#) (2022).
- [106] R. Besuner *et al.* (Spec-S5), The Spectroscopic Stage-5 Experiment, [arXiv:2503.07923 \[astro-ph.CO\]](#) (2025).
- [107] D. Foreman-Mackey, D. W. Hogg, D. Lang, and J. Goodman, emcee: The MCMC Hammer, *Publ. Astron. Soc. Pac.* **125**, 306 (2013), [arXiv:1202.3665 \[astro-ph.IM\]](#).
- [108] D. W. Hogg and D. Foreman-Mackey, Data analysis recipes: Using Markov Chain Monte Carlo, *Astrophys. J. Suppl.* **236**, 11 (2018), [arXiv:1710.06068 \[astro-ph.IM\]](#).
- [109] D. Foreman-Mackey, W. Farr, M. Sinha, A. Archibald, D. Hogg, J. Sanders, J. Zuntz, P. Williams, A. Nelson, M. de Val-Borro, T. Erhardt, I. Pashchenko, and O. Pla, Emcee v3: A Python ensemble sampling toolkit for affine-invariant MCMC, *Journal of Open Source Software* **4**, 1864 (2019).
- [110] D. Foreman-Mackey, corner.py: Scatterplot matrices in python, *Journal of Open Source Software* **1**, 24 (2016).
- [111] C. R. Harris *et al.*, Array programming with NumPy, *Nature* **585**, 357 (2020), [arXiv:2006.10256 \[cs.MS\]](#).
- [112] P. Virtanen *et al.*, SciPy 1.0—Fundamental Algorithms for Scientific Computing in Python, *Nature Meth.* **17**, 261 (2020), [arXiv:1907.10121 \[cs.MS\]](#).

- [113] J. D. Hunter, Matplotlib: A 2D Graphics Environment, *Comput. Sci. Eng.* **9**, 90 (2007).
- [114] S. Hoyer and J. Hamman, xarray: N-D labeled arrays and datasets in Python, *Journal of Open Research Software* **5**, 10.5334/jors.148 (2017).
- [115] R. Kumar, C. Carroll, A. Hartikainen, and O. Martin, Arviz a unified library for exploratory analysis of bayesian models in python, *Journal of Open Source Software* **4**, 1143 (2019).
- [116] A. Meurer *et al.*, SymPy: symbolic computing in Python, *PeerJ Comput. Sci.* **3**, e103 (2017).
- [117] E. van der Velden, CMasher: Scientific colormaps for making accessible, informative and 'cmashing' plots, *The Journal of Open Source Software* **5**, 2004 (2020), [arXiv:2003.01069 \[eess.IV\]](#).
- [118] J. Bradbury, R. Frostig, P. Hawkins, M. J. Johnson, C. Leary, D. Maclaurin, G. Necula, A. Paszke, J. VanderPlas, S. Wanderman-Milne, and Q. Zhang, *JAX: composable transformations of Python+NumPy programs* (2018).
- [119] P. Kidger, *On Neural Differential Equations*, *Ph.D. thesis*, University of Oxford (2021), [arXiv:2202.02435 \[cs.LG\]](#).
- [120] W. Hu, R. Barkana, and A. Gruzinov, Cold and fuzzy dark matter, *Phys. Rev. Lett.* **85**, 1158 (2000), [arXiv:astro-ph/0003365](#).
- [121] L. Balkenhol, C. Trendafilova, K. Benabed, and S. Galli, candl: cosmic microwave background analysis with a differentiable likelihood, *Astron. Astrophys.* **686**, A10 (2024), [arXiv:2401.13433 \[astro-ph.CO\]](#).
- [122] Planck Collaboration, *clipy* (2018), commit hash ad1aff3.
- [123] D. Blas, J. Lesgourgues, and T. Tram, The Cosmic Linear Anisotropy Solving System (CLASS) II: Approximation schemes, *JCAP* **07**, 034, [arXiv:1104.2933 \[astro-ph.CO\]](#).
- [124] J. Lesgourgues, The Cosmic Linear Anisotropy Solving System (CLASS) I: Overview, [arXiv:1104.2932 \[astro-ph.IM\]](#) (2011).
- [125] A. Lewis, A. Challinor, and A. Lasenby, Efficient computation of CMB anisotropies in closed FRW models, *Astrophys. J.* **538**, 473 (2000), [arXiv:astro-ph/9911177](#).